Imperial College London
Department of Mechanical Engineering
Division of Thermofluids

Population Balance Modelling of Soot Formation in Laminar and Turbulent Flames

By

Binxuan Sun

Supervisor: Dr. Stelios Rigopoulos

Submitted for the degree of
Doctor of Philosophy
January 2021

Abstract

The reduction of soot emissions in combustion processes is a primary concern of combustion engineers due to the severe health impact of soot, and the prediction of the soot particle size distribution (PSD) has become important. The evolution of the PSD can be predicted by solving the population balance equation (PBE), and several approaches have been proposed for introducing soot morphology in the PBE. Furthermore, the PBE must be coupled with fluid dynamics, species transport and chemical kinetics in order to predict soot properties in laminar and turbulent flames. Finally, accurate and computationally efficient methods must be employed for solving the CFD-PBE approach.

In the first part of this thesis, the recently developed conservative finite volume sectional method for the solution of the population balance equation (PBE) is extended to a two-PBE approach for modelling soot formation that distinguishes between coalescence and aggregation and accounts for finite-rate fusing of primary particles within aggregates, while providing a numerically accurate description of primary particle surface growth and oxidation within aggregates. The validation of the method is conducted by reproducing the self-preserving distributions of aggregates with varying fractal dimension. Subsequently, the one-PBE and two-PBE approaches are coupled with CFD and applied to the application of the Santoro laminar non-premixed co-flow sooting flame. By using a comprehensive soot kinetic model, the deficiencies of the one-PBE approach are analysed, and the two-PBE approach is shown to provide a significant improvement in the description of soot morphology using a properly adjusted particle fusing rate. At present, the model parameters for the fusing of soot primary particles are based on sintering models from silica and titania nanoparticles due to the lack of experimental data for soot. Therefore, a comprehensive sensitivity analysis of the model parameters is conducted. The results show the predictive potential of both the one-PBE and two-PBE approaches. With the presently available experimental measurements, the results suggest that one-PBE method is a reasonable choice for the applications associated with turbulent flame.

Subsequently in the second part, the one-PBE method is incorporated into the LES-PBE-PDF approach developed within the group for modelling soot formation in turbulent flames. For the first time, the LES-PBE-PDF approach provides a comprehensive physicochemical model accounting for nucleation, surface growth, oxidation, condensation, coalescence and aggregation. The interaction between chemistry, turbulence and soot particles are accounted for by resolving an evolution equation for the LES-filtered one-point, one-time, joint scalar-number density probability density function (PDF). The Eulerian stochastic field method is used for the solution of the joint-scalar-number density PDF. By using the same kinetics and model parameters as tested in the laminar flame case, the LES-PBE-PDF approach is applied to model soot formation in the Sandia turbulent non-premixed sooting flame. The predicted thermochemical conditions and soot volume fraction are in reasonably good agreement with experimental measurements. The analysis and findings demonstrate good predictive capability and computational feasibility of the complete LES-PBE-PDF approach.

In summary, this thesis presents a systematic study for soot formation in the laminar and turbulent flames. In particular, the key adjustable model parameters, surface reactivity α and cut-off point d_c, are calibrated in the laminar flame and employed in the turbulent flame. Yet, some limitations should be pointed out. For soot study, the current methodology does not capture the composition of soot during its formation and growth, thus the surface reactivity model applied is rather primitive and needs some adjustments, and the work assumes a constant fractal dimension, whose impact should be further investigated. For turbulent sooting flame, future investigation regarding the micromixing model is warranted.

Copyright declaration

Declaration of originality

I certify that the work presented here is original, except as acknowledged, and has not been submitted, either in whole or part, for a degree at any other university than Imperial College London. This thesis is produced under the supervision of Dr. Rigopoulos. Contents taken from other sources are cited as such.

Acknowledgements

Throughout my PhD time at Imperial College London, I have been financially supported by the Imperial-CSC Scholarship. I am very lucky and very grateful for having had this opportunity to pursue a PhD at Imperial College London. For the computationally expensive numerical cases, I gratefully acknowledge the HPC services from Imperial College Research Computing Service (DOI: 10.14469/hpc/2232), ARCHER UK National Supercomputing Service (http://www.archer.ac.uk), and the UK Materials and Molecular Modelling Hub, which is partially funded by EPSRC (EP/P020194/1 and EP/T022213/1).

I would like to express my gratitude to Dr. Stelios Rigopoulos for his support, encouragement, and trust and above all, for giving me this opportunity to be part of the scientific community. During the past few years, we have had numerous discussions that are invaluable to me. With his professional advice, his patience and his positive spirit, I have overcome and achieved so many and finally reached this far. This memory will never fade. I would also wish to thank Dr. Salvador Navarro-Martinez and Prof. William Jones, for their accessibility and invaluable comments when I encounter problems learning and using the in-house code LES-BOFFIN. In particular, I would like to sincerely express my gratitude to Dr. Fabian Sewerin, who has kindly shared many thoughts and offered much help for the hitches and setbacks I experienced.

My colleagues at Imperial have always been very kind and supportive. I am very grateful for their friendship and accompany, making my past few years in Imperial so memorable. I would like to thank (in the order we met) Panos, Larry, Fabian, Lucas, Yuri, Hin-Yan, Tianjie, Tom, Malamas and Danny, and I wish them all the best for whatever goals they may pursue in their future. I will miss the good old times, the hot pot parties, the afternoon tea breaks and all the silly jokes and laughs we had. I am also thankful for all the supports from Kate and helps from all the other kind people at Imperial.

Lastly, this thesis is dedicated to my parents and my uncle Norman for their love and inspiration throughout my life, for which no words can truly express my gratitude. Thank you for everything that makes me who I am today.

Contents

List of Tables

List of Figures

Nomenclature

Abbreviations

CFD	Computational fluid dynamics
CMC	Conditional moment closure
DNS	Direct numerical simulation
FPV	The The flamelet/progress variable model
GDE	General dynamic equation
HAB	Height above burner
HACA	Hydrogen-abstraction-carbon-addition
LES	Large eddy simulation
MC	Monte Carlo
PAH	Polycyclic aromatic hydrocarbon
PBE	Population balance equation
PDF	Probability density function
PSD	Particle size distribution
R.H.S.	Right hand side
RANS	Reynolds-averaged Navier–Stokes equations

RMS	Root mean square
SDE	Stochastic differential equations
SGS	Sub-grid scale
TVD	Total variation diminishing

Greek letters

α	The fraction of active soot surface sites
β^c	The collision frequency in continuum regime
β^f	The collision frequency in free molecule regime
β^t	The collision frequency in transition regime
$\beta_{i,j}$	The collision frequency between particles of size i and particles of size j
χ	The scalar dissipation rate
χ_s	The number density of surface sites
χ_s-	The number density of active surface sites
Δ	The filter width in LES
$\delta(\cdot)$	Dirac's delta distribution
δ_{ij}	The Kronecker delta
$\dot{\omega}_k$	The production/destruction source term of scalar k
η	The Kolmogorov length scale
Γ	The scaled turbulent kinematic viscosity
γ_i	The sticking coefficient factor for a PAH_i

κ	The micromixing frequency
λ	The thermal conductivity of the mixture
λ_g	The mean free path of the carrier gas
$\mathbf{\Phi}(\mathbf{x}, t)$	The reactive scalar fields
$\mathbf{\Psi}$	Sample space vectors associated with scalar fields $\mathbf{\Phi}(\mathbf{x}, t)$
μ	The viscosity of the fluid
μ_{sgs}	The SGS turbulent viscosity
ν	The kinematic viscosity of the fluid
ω_{PAH}	The self-collision rate of a PAH
ω_{cond}	The condensation rate
ω_{nuc}	The production rate of the soot nuclei
$\phi(\mathbf{x}, t)$	A scalar function
ψ	Sample space variable associated with $\phi(\mathbf{x}, t)$
ρ	The density of the fluid
ρ_P	The density of particles
ρ_s	The density of soot aggregates
σ	The molecular diameter
$\tau(l)$	The characteristic timescale of eddies of size l
τ_c	Chemical timescale
τ_s	The characteristic sintering timescale
τ_t	Turbulent flow timescale

τ_η	The Kolmogorov timescale
τ_{ij}	The viscous stress tensor for a Newtonian fluid
$\upsilon'_{k,i}(\upsilon''_{k,i})$	The forward(backward) stoichiometric coefficient for species k in reaction i
ε	The turbulent dissipation rate

Latin letters

$\bar{W}$	The average molecular weight of the mixture
$\dot{C}$	The condensation source term for aggregates
$\dot{C}_p$	The condensation source term for primary particles
$\dot{m}_i(\boldsymbol{\theta}, \mathbf{x})$	Micromixing model
$\dot{Q}$	The radiation heat loss
$\dot{W}_j(t)$	The time derivative of the Wiener process $\mathbf{W}(t)$
$\mathbf{W}(t)$	Wiener process
$\mathbf{Z}$	Joint scalars associated with $\mathbf{Y}(\mathbf{x}, t)$ and $\mathbf{N}(v, \mathbf{x}, t)$
$\mathbf{z}$	Joint sample space variables associated with $\mathbf{Y}(\mathbf{x}, t)$ and $\mathbf{N}(v, \mathbf{x}, t)$
$\bar{\cdot}$	The LES filtering operator
$\mathbf{N}(v, \mathbf{x}, t)$	Number density scalars
$\mathbf{N}_\rho(v, \mathbf{x}, t)$	Mass-based number density scalars
$\mathbf{Y}(\mathbf{x}, t)$	Reactive scalars
Da	Damköhler number
Re	Reynolds number

Sc	Schmidt number
a_i	The surface area of aggregates of size i
a_s	The surface area of the volume-equivalent sphere
B	The nucleation source term
C_κ	The micromixing frequency constant
C_S	The Smagorinsky constant
C_{ov}	The overlap parameter
D^T	The thermal diffusivity
D_A	The size of a single aromatic ring
d_c	The cut-off point or the critical diameter
D_f	The aggregate fractal dimension
d_g	The diameter of gyration
D_m	The diffusion coefficient for mixture
D_P	The kinematic diffusivity for the particle
d_p	The diameter of primary particle
d_PAH	The diameter of a PAH
d_P	The particle diameter
D_k^m	The diffusion coefficient for species k due to the Fick's law
D_k^T	The thermal diffusion coefficient for species k
E_a	The activation energy in sintering timescale
E_i	The activation energy in chemical reactions

e_{ij}	The strain rate tensor
$f(\mathbf{\Psi};\mathbf{x},t)$	A probability density function associated with scalar fields $\mathbf{\Phi}(\mathbf{x},t)$
$f(\mathbf{y},\mathbf{n};\mathbf{x},t)$	Joint scalar-number density PDF
f_v	Soot volume fraction
G	The net rate of change of particle properties due to surface reaction
g	The gravitational acceleration
$g(\mathbf{\Psi};\mathbf{x},t)$	A fine-grained density function associated with $f(\mathbf{\Psi};\mathbf{x},t)$
$G(\mathbf{x}-\mathbf{x}^{'})$	The spatial filter function in LES
$g(\mathbf{y},\mathbf{n};\mathbf{x},t)$	Fine-grained density associated with $f(\mathbf{y},\mathbf{n};\mathbf{x},t)$
h	The total enthalpy of the mixture
$h(\mathbf{y},\mathbf{n},t;\mathbf{x})$	Transition PDF associated with $\theta_k^n(t;v,\mathbf{x})$
k	The turbulent kinetic energy
k_f	The fractal prefactor
k_B	The Boltzmann constant
$K_{c,i}$	The equilibrium constant for reaction i
k_g	The reaction rate coefficient for species g
L	The characteristic length scale of the flow
l_D	The length scale that separate the dissipation range and inertial range
l_E	The length scale that separate the anisotropic eddies and isotropic eddies
m_i	The mass of a PAH$_i$

$n(v, \mathbf{x}, t)$	The number density of particles per unit mixture volume
n_f	The number of independent stochastic fields $\theta(t; v, \mathbf{x})$
N_i	Number density (or concentration in discrete PBE) of soot aggregates of size i
N_m	The number of molecules per unit volume
n_p	The number density of primary particles
$N_\rho(v, \mathbf{x}, t)$	The mass-based number density scalars
$n_\rho(v, \mathbf{x}, t)$	The number density of particles per unit mixture mass
N_{A}	The Avogadro number
n_{av}	The number of primary particle per aggregate
$N_{p,i}$	The number density of primary particles of size i
q_j	The energy flux along $j-$th direction
R	The universal gas constant
$R_g(\mathrm{HACA})$	The mass growth rate due to HACA
S_i	Surface area of a soot aggregate of size i
S_{ij}	The strain rate tensor
T	Temperature
$u(l)$	The characteristic velocity of eddies of size l
u_j	The velocity along $j-$th direction
u_j^t	The thermophoretic velocity due to the temperature gradient
u_η	The Kolmogorov velocity scale

v_i	The volume of a soot particle of size i
v_{dimer}	The average volume of dimers
$v_{k,j}$	The diffusion velocity of species k along $j-$th direction
W_k	The molecular weight of species k
X_k	The mole fraction of species k
Y_k	The mass fraction of species k
Z	The mixture fraction
C(s)	Soot
C(s)$-$	Soot with active sites
Cu	The Cunningham correction factor for slip flow
Kn	The Knudsen number
$\theta(t; v, \mathbf{x})$	A stochastic field

Other symbols

$\langle\cdot\rangle$	The time-average operator in RANS
$\widetilde{\cdot}$	The Favre filtering operator in LES
$[\cdot]$	The concentration of species

Terminology associated with particle formation processes

Agglomeration	The process of particle collision to form soot agglomerates, which are groups of particles loosely held together
Aggregation	The process of particle collision to form soot aggregate, which are particles composed of two or more smaller primary particles firmly bound together

Coagulation	The processes that joint particles together, including coalescence, aggregation and agglomeration
Coalescence	The merging of two liquid-like soot particles into a spherical particle, which is a possible outcome of coagulation
Condensation	The process representing a heterogeneous gas-to-particle conversion. In this thesis, it represents the mass addition process of soot particle as a result of collisions between particles and gas-phase precursors
Fusing	The process of merging soot primary particles within a soot aggregate
Nucleation	The process of particle formation from gas-phase precursors to form the first particles, interchangeably with the term inception
Oxidation	The process of reducing soot mass by converting the solid-phase particle to gas-phase products
Sintering	The process of bonding and coalescence of particles into a larger one, used often in material science. In this thesis, this term is retained when referring to inorganic nanoparticles
Surface growth	The process of adding gas-phase species to the soot particle surface to increase the mass of the soot particles

Chapter 1

Introduction

1.1 Background

Soot is combustion-generated particulate matter formed from the incomplete gas-phase hydrocarbon combustion processes, consisting mainly of carbon and a small amount of H and other compounds existing in the fuels. These carbonaceous particulates are polydisperse, including incipient molecular particles of a liquid-like nature, and mature aggregates ranging from tens of nm up to a few μm [1].

Research efforts have been made to investigate the characteristics of soot and predict its formation in combustion processes. These studies are of great importance for several reasons. First and foremost, soot emissions are detrimental to the human health and environment. In the human body, exposure to soot derived from automobile engines may cause respiratory and cardiovascular diseases. Fine particles can get deep into lungs, and some may penetrate bloodstreams. Extensive studies in epidemiology have indicated that occupational exposure to diesel soot can be carcinogenic [2]. From an environmental aspect, soot has been identified as a significant cause in global warming [3, 4]. It acts as a strong absorber of sunlight and light reflected by the surface of Earth. Subsequently, the deposition of soot on polar ice could accelerate its melting and pose a threat to the vulnerable Arctic climate [5]. Moreover, soot tends to deposit in chimneys in domestic houses, leading to chimney fires if being ignited.

From an engineering perspective, soot's thermal radiation may have an adverse impact in a combustor, and soot may also damage combustion engines if deposited on its walls. On the other hand, soot can also be desirable. Soot finds its use with versatility in industrial applications, including carbon black use as pigments in inks and as a reinforcing phase in automobile tires. In furnace combustion, the heat transfer can be enhanced by soot radiation. As such, a great interest lies in controlling the production of soot particles, e.g., to reduce the soot emission from engines, to enhance the production of carbonaceous particles or control its properties in targeted combustors. The aforementioned reasons call for the need to predict soot formation.

Most combustion-generated soot undergoes a series of complex processes of nucleation, surface growth, oxidation, coalescence and aggregation, leading to a broad range of size distribution, and soot aggregates may present different properties, e.g., the radiative property [6], depending on its polydispersity (the degree of non-uniformity of a distribution). Soot properties also change dramatically with the conditions under which it is formed, such as the local chemical composition and thermodynamic conditions associated with the nature of the flow. Thus, a proper description for the soot kinetics is of paramount importance.

Since soot particles are polydisperse, one needs concepts from aerosol dynamics to describe the dynamical evolution of the particle properties. The Population Balance Equation (PBE) provides a mathematical tool that describes the evolution of the distribution of the characteristic property of the population. In the PBE, the particle entities can be characterised by one or more properties. The property in question is usually a measure of the particle size such as particle volume, particle mass or equivalent particle diameter, but other properties may also be relevant, such as the particle surface area. Formally, the PBE is an equation, or a system of equations that record the evolution of the particle size distribution (PSD) due to processes, such as nucleation, surface growth, coalescence and aggregation, and its mathematical form can be complex. The current solution methods of the PBE can be classified into several categories, among which the most prevalent two are moment-based methods and discretisation methods. The former is computationally effective, but solving only the low-order moments of the PSD; the latter provides a complete representation of the particle size distribution and thus, with increasing CPU power, have appeared more frequently in recent applications.

Currently, to obtain an accurate prediction of soot, a numerical model needs to: a) capture the formation of soot nuclei and its growth pathways, b) account for the polydispersity and morphology of soot particles, and c) address properly the complex coupling between chemical kinetics, fluid dynamics and particle events. The main targets of this thesis are related to mathematical modelling and numerical solution of soot aerosol dynamics, and the coupling of PBE and Computational Fluid Dynamics (CFD) in laminar and turbulent flames, attempting to address the following research challenges:

1. **How to address soot morphology properly from the viewpoint of model formulation and numerical methods for the solution of PBE.**

2. **The current CFD-PBE methods addressing the turbulence-chemistry-soot interaction either bring extra assumptions which make it extremely challenging to evaluate the source of uncertainties, or are primitive.**

3. **A systematic evaluation of population balance modelling for soot formation in laminar and turbulent flame is currently missing.**

Regarding the first challenge, a proper description for soot morphology is necessary because it has an impact on coagulation process and surface reactions. The fractal shape of soot must be accounted for when modelling the collision events among particles. For instance, the collision diameter of a chain-like aggregate is much larger than a spherical one with the same volume. Also, the surface area of an aggregate containing a number of primary particles also deviates dramatically from that of a volume-equivalent spherical particle. Such deviation can be problematic as a proper description of the aggregate surface area is important in modelling soot surface growth phenomena. Currently, most of the approaches belonging to the family of discretisation methods predict only the number density of soot aggregates (one-PBE method) (e.g., see Refs. [7, 8]). For larger aggregates with multiple primary particles, a common strategy is to assume that the size of primary particles is uniform and equals to a fixed size, neglecting the interaction between primary particles (e.g., the fusing of soot primary particles). The morphology of aggregates can then be accounted for based on further models. However, such a simplification would inevitably lead to inconsistency from a physical point of view, as it incurs the assumption that primary particles stop growing after reaching the pre-defined size. Although alternative methods can be developed (e.g. multi-dimension PBE method), these methods would introduce further issues, such as high CPU cost. An investigation regarding this inconsistency is necessary, particularly in the cases where the PBE is coupled with the flow.

In practical applications, another problem arises when the PBE must be coupled with fluid dynamics and chemistry. In laminar flames, this problem is rather straightforward as the flow field is fully resolved, presenting an accurate velocity field, but severe challenges exist in soot modelling in turbulent reacting flows. Although turbulence has been the subject of numerous investigations, our knowledge of turbulence is rather phenomenological. The random and chaotic nature of the instantaneous flow field leads to various length and time scales in the fluid motion. The turbulent fluctuations in velocity field can affect reactive scalar fields via turbulent convection, and subsequently, the particle concentration field, as the evolution of PSD depends on kinetic models in which the rate of each process is a function of local reactive scalars. For a conventional Reynolds-averaged (RANS) description, such correlations will lead to severe closure challenges as there are many unclosed terms due to fluctuations in reactive scalars and particle number density. The same type of problems exists also in the Large Eddy Simulation (LES). These issues bring about the second research challenge mentioned above. In the work of Rigopoulos [9], a PBE-PDF method was proposed to address the closure problem in the context of RANS. In the recent works of Sewerin and Rigopoulos [10, 11], the PBE-PDF model has been extended to LES (named as LES-PBE-PDF) to predict soot formation in turbulent reacting flow. The most advantageous feature of the LES-PBE-PDF is that it addresses the interaction of turbulent flow, chemistry and particle formation without additional closure models, and kinetic model of arbitrary complexity can be incorporated easily without introducing further assumptions. However, in earlier applications of the RANS PBE-PDF method to study precipitation and in the application of recent LES-PBE-PDF method to aerosol and soot, only nucleation and surface reactions were considered. A complete PBE encompassing coalescence and aggregation was not employed, and the kinetic model employed in Ref. [11] was rather simple, which meant that the full potential of the LES-PBE-PDF approach remained unexplored.

Lastly, a quantitatively good prediction of soot formation in turbulent flames is still an extremely challenging task (if not impossible) for now. It is very difficult to evaluate the source of errors as uncertainties come from several aspects including chemistry, soot kinetics, fluid dynamics, and aerosol dynamics. On the other hand, a numerical model must draw information from the available experimental measurements to carry out meaningful model validation. The state of the art in the simulation of turbulent sooting flames can barely provide a qualitatively good result, not to mention the fittings required for the model parameters. Whether it is possible to get good predictions in turbulent flames by employing a model that has been validated and investigated in the laminar flame without amendments remains unanswered. In my opinion, a systematic evaluation of population balance modelling for soot formation in laminar and turbulent flames would facilitate the understanding of the research needs and potentially reveal useful paths for future investigations.

1.2 Objectives of the thesis

Subsequently, the objectives of this thesis are threefold:

Firstly, to develop a physically realistic PBE model, a two-PBE method named

CFV-2PBE that addresses the inconsistency existed in a previously developed one-PBE method (CFV-1PBE) by taking into account the fusing of soot primary particles, and then to conduct a detailed sensitivity analysis of key model parameters for both CFV-1PBE and CFV-2PBE methods in the context of the Santoro laminar flame with a comprehensive soot kinetics, in order to systematically study the potential and limitations of the one-PBE and two-PBE approaches.

Secondly, to introduce coalescence and aggregation into the LES-PBE-PDF approach such that the model, for the first time, accounts for a comprehensive aerosol dynamics description, including particle nucleation, surface growth, oxidation, condensation, coalescence and aggregation, in the context of turbulent flows without bringing further closure assumptions. By doing so, this thesis aims to provide a numerical method that is compatible with various chemistry and soot kinetics and is computationally feasible.

Lastly, to apply the LES-PBE-PDF approach to investigate soot formation in the Sandia turbulent non-premixed flame with the validated numerics and the same kinetics calibrated in the Santoro laminar flame. By doing so, this work attempts to shed some light on the nature of discrepancies that arise in the simulation of turbulent sooting flames.

1.3 Outline of the thesis

Chapter 2 provides the theoretical background of the thesis. In particular, I briefly review the current knowledge regarding soot kinetics, including a few well-studied soot kinetic models that have been adopted prevalently in practical applications. Next, a general introduction of the population balance equation is presented, and the first research challenge mentioned above is further elucidated (See Section 2.2.2). Then the governing equations and the fundamental knowledge regarding the modelling of soot in turbulent flames is also reviewed. In particular, the research challenge regarding the CFD-PBE coupling in turbulent flames are discussed in detail in Section 2.6.

In Chapter 3, I address the development of CFV-2PBE method and the associated coupling in CFD; while in Chapter 4, I report a comprehensive soot kinetic model and conduct a systematic study for both the CFV-1PBE and CFV-2PBE methods in the Santoro laminar diffusion flame. Subsequently, I present the LES-PBE-PDF approach, its derivation, solution scheme, and associated numerics in Chapter 5, followed by its application in a turbulent non-premixed Sandia sooting flame in Chapter 6. Finally, the thesis's findings are concluded with an outlook for future work in Chapter 7.

Chapter 2

Theoretical Background

In this chapter, I review the main concepts for the modelling of soot kinetics first, discussing several types of classical models that have been employed in practical applications. For aerosol dynamics, the PBE is of central importance as it describes the dynamics of a polydispersed particle system. Thus, a concise summary regarding the PBE and the research challenges associated with the solution scheme of PBE is presented next. Since the numerical study of this work involves the coupling of PBE and fluid dynamics, the fundamental laws of conservation are demonstrated next. Finally, I introduce briefly soot modelling in turbulent reactive flow, especially the challenges regarding the modelling of turbulent-chemistry interaction and turbulence-chemistry-soot interaction.

2.1 Modelling of soot kinetics

In order to model the detailed sooting process, one needs to examine the insights of a complex system. Note that the terminology associated with the overall soot formation process discussed in this thesis can be found in the nomenclature of this thesis. Starting from the very first step, the fuel experiences, either pure or oxidative pyrolysis depending on the flame type. During this process, the aromatic rings are formed and further undergo growth by adding carbon radicals to form polycyclic aromatic hydrocarbons

(PAH). Under certain flame conditions, these PAHs would interact with each other and combine into larger matters with polynuclear aromatic structure, which eventually grows to incipient soot particles (or soot nuclei), the first recognisable soot particles. These incipient soot particles are very small at this stage, which makes experimental measurements extremely challenging, and the volume of these incipient soot particles contributes negligibly to the total soot volume. All the processes involved till this stage can be grouped and referred to as inception, or nucleation, although in recent studies there are more specific subcategories to distinguish the different stages involved in the inception process in terms of the evolutionary history of PAHs [12]. The PAHs are referred as soot precursors, which are molecular gas-phase species that act as the building blocks of soot particles, playing a role in inception and mass addition. Subsequently, the soot nuclei would experience a series of chemical and physical events to form young soot. The young soot particles have evolved beyond the inception stage, often containing large amounts of hydrogen and having liquid-like properties [12, 13]. In the high-temperature region, the young soot would dehydrogenate (this process is also referred as carbonisation) and react both physically (condensation) and chemically (surface growth) with gaseous hydrocarbon species, resulting in a significant increase in soot mass. In the meantime, the young soot particles also experience coalescence, agglomeration and aggregation (these processes are often grouped and referred as coagulation), which lead to agglomerates (groups of particles loosely held together) or mature soot aggregate (soot particles composed of smaller primary particles firmly bound together [14]) with a fractal shape [15]. Simultaneously, with all processes mentioned above, there can be a continual oxidative attack (oxidation) on the PAHs and soot particles to form gaseous products and reduce their size [16, 17]. Fig. 2.1 demonstrates the overall processes discussed above. In this section, the review targets on the modelling of the inception, surface growth and oxidation process, while leaving the coagulation to be discussed with PBE in the next section. One may refer Ref. [15] for a detailed explanation of the terminology associated with soot.

There has been a large body of research on soot kinetics since the last century.

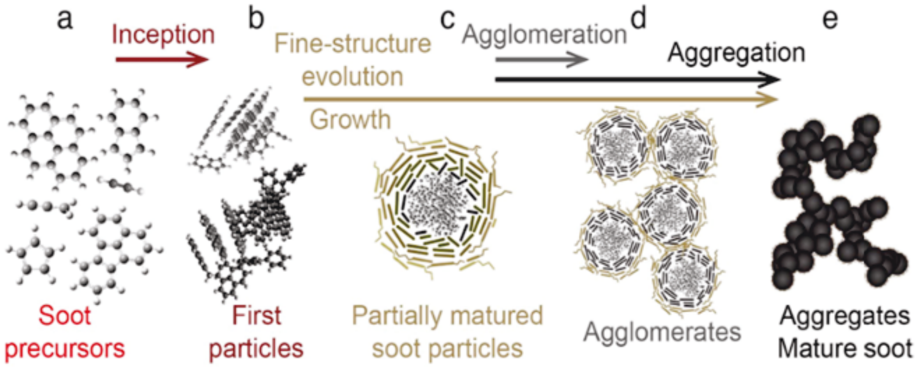

Figure 2.1: Schematic diagram of the overall soot formation processes and the representative products as the process proceeds. The illustration is adapted from [15].

Reviews by Haynes and Wagner [18], Glassman [19] and Kennedy [20] provide a clear picture of the early groundwork. Over the last two decades, further progress has been made with significant improvements in the detailed soot model description. One may find useful information in more updated reviews by Mansurov [21], D'Anna [22] and Wang [12]. In a very recent review paper by Rigopoulos [23], a concise summary of soot kinetic models is presented. As this is a vast subject, a comprehensive review is beyond the scope of the thesis; only the main concepts of well-established models are presented here to explain how soot kinetics work.

In the review in 1997, Kennedy classified soot models in three categories, namely empirical correlations, semi-empirical models and detailed models. Models being classified into the first category are rather simple, as soot is related to overall parameters (usually in engines) such as the unburned equivalence ratio, and are not suitable for direct coupling with fluid dynamics. They are rarely employed in research nowadays, so I will omit the literature review in this category. The semi-empirical models are the next level of soot modelling, incorporating some aspects of soot physics and chemistry. The models belong to this family can be further divided into non-precursor models and precursor models [23], depending on what type of parameters the soot is related to. The semi-empirical non-precursor models relate soot to temperature or mixture fraction and are mostly outdated now for research purposes due to an over-simplification of the system. An example is a model proposed by Tesner and co-workers [24], where soot formation is linked with temperature and a two-equation model for the number density of soot nuclei (originally named radical nuclei) and soot particles. Regardless of its simplicity, it was used widely over that period time in a range of combustion applications including turbulent sooting flames [25, 26]. The semi-empirical precursor models relate soot particles to precursors such as C_2H_2 or other PAHs via finite empirical kinetics, and generally require coupling with relatively detailed chemistry. As will be discussed in the following subsections, these models rely on empirical inputs for the soot nucleation, growth and oxidation rates, and are limited inherently to specific conditions. For generality, the detailed models are developed to offer a comprehensive description of PAH kinetics, soot inception, and subsequent growth. By design, models of this family are much more expensive. Many of the studies applying detailed models have been on ideal reactors or simplified laminar flows, however, there is also an increasing number of relatively recent studies employing these models to turbulent flows [27–29].

In the last two decades, most of the models employed in research belong to the families of semi-empirical precursor models and detailed models, and therefore I will focus on these two categories. Since some models are hybrid, adopting only some components of detailed models, my review will revisit several broadly-validated models as examples based on two distinct stages of the sooting process: the formation of soot nuclei and its following surface reactions respectively.

2.1.1 Formation of soot nuclei

There are many uncertainties involved in modelling the nucleation of soot particle. The transition between PAHs and soot are still poorly understood, and the size of the soot nuclei can not be identified with accuracy in the experiment due to its physical and chemical characteristics. As such, nucleation is generally rendered as the most difficult step to model. Early models are relatively simple, representing nucleation with a global expression, and the rate of nucleation is often related to species that play an important role in the sooting process, while more recent models tend to present the nucleation process with several PAHs and require a comprehensive description of PAH formation.

2.1.1.1 Semi-empirical precursor models

In the family of semi-empirical precursor models, a widely used one is acetylene-based, describing nucleation with a global reaction associated with C_2H_2, formulated by Leung et al. [30] as:

$$C_2H_2 \longrightarrow 2C(s) + H_2 \tag{2.1}$$

$$R_n = k_n(T)[C_2H_2] \tag{2.2}$$

where C(s) denotes the soot, k_n is the Arrhenius-type expression of the nucleation rate depending on temperature. One should note that the notation C(s) is not a rigorous description, as nascent soot particles have a relatively large carbon/hydrogen (C/H) ratio [31]. Due to the absence of a generally accepted alternative, it has been adopted for the demonstration purpose. In the model of Leung et al. [30], the size of nuclei was assumed to be 1.24 nm, equivalent the size of 100 carbon atoms. An extension proposed by Lindstedt [32] also includes a benzene nucleation step. Later on, Hall et al. [33] proposed a simplified PAH model, in which the nucleation is related to small PAHs, $C_{10}^{\cdot}H_7$ and $C_{14}H_{10}$ respectively. Since the authors aimed to minimise complications to chemistry, a series of steady-state assumptions were used to estimate the formation rate of $C_{10}^{\cdot}H_7$ and $C_{14}H_{10}$ using 'simple' species such as H_2, C_2H_2 and C_6H_6 etc. To accommodate practical applications, the reaction rate of this model is enlarged by eight times in Ref. [33]. For these models, the dependence of nucleation on acetylene suggests that this species must be predicted with accuracy, which can be achieved with chemical mechanisms of various complexity for simple fuels. Applications can be seen in both laminar [34] and turbulent flames [11,35].

2.1.1.2 Detailed models

The nucleation in detailed models requires the formation of aromatic species firstly. The kinetic study of PAH formation is extensive, see e.g. Ref. [36] or [37] for more information. The relatively recent work of Wang [12] also provides a detailed review. The main role of PAHs in soot formation is to link the gas-phase chemistry and soot nucleation, although they can also contribute to soot mass growth via condensation. Currently, the most celebrated mechanism for PAH formation is the hydrogen-abstraction-carbon-addition (HACA) mechanism, pioneered by Frenklach and coworkers [38–40]. It captures the essence of the thermodynamic and kinetic requirements for the sooting process. A prototype model for the growth of PAHs can be summarised as:

$$\mathrm{A}_i + \mathrm{H} \rightleftharpoons \mathrm{A}_i \cdot + \mathrm{H}_2 \tag{2.3}$$

$$\mathrm{A}_i + \mathrm{C}_2\mathrm{H}_2 \rightleftharpoons \mathrm{A}_i\mathrm{C}_2\mathrm{H}_2 \cdot \tag{2.4}$$

$$\mathrm{A}_i\mathrm{C}_2\mathrm{H}_2 \cdot + \mathrm{C}_2\mathrm{H}_2 \longrightarrow \mathrm{A}_{i+1} + \mathrm{H} \tag{2.5}$$

where A_i is a PAH with i aromatic rings. Important factors include: a) acetylene, the molecular building block species, b) the H atom, the driving force behind chain branching and flame propagation, and c) the high temperature that speeds up the kinetics. The oxidation is also considered in HACA but omitted here. Beyond the HACA mechanism, other reaction pathways may exist. For example, it is widely recognised that resonantly stabilised radical species are important in aromatics formation and growth of molecular weight [12]. These species include propargyl, benzyl and cyclopentadienyl. Despite all recent advances, further research is needed for fundamental chemical kinetics of aromatics. Given the large variability in fuel composition, PAH formation from real fuel combustion remains very challenging [12]. Presently, one of the most well-studied implementations is the ABF mechanism [41] by Appel et al. Other detailed PAH mechanisms can be found in Marinov et al. [42], D'Anna and Kent [43], Richter et al. [44], Slavinskaya and Frank [45] and Blanquart et al. [46].

Another major step for the nucleation in detailed models is the transition from PAHs to soot. As no experiment technique is available to analyse the soot nuclei, the detailed process remains uncertain. Currently, three conceptual pathways may be postulated for the inception of soot nuclei [12], as shown in Fig. 2.2. Path A represents the growth of "two-dimensional" PAHs into curved, fullerene-like structure; paths B denotes the physical coalescence of moderate-sized PAHs into stacked clusters; and path C involves the chemical bonding of PAHs into interlinked three-dimensional structures. As discussed in Ref. [12], path A is too slow to model the nucleation rate within the framework of HACA; and many works are in favour of path B and C, in which PAH dimerisation (the collision between PAHs to form a dimer) is taken as the initial nucleation step. For instance, the nucleation in the ABF mechanism is modelled as the self-collision of two pyrenes (four aromatic rings, $C_{16}H_{10}$).

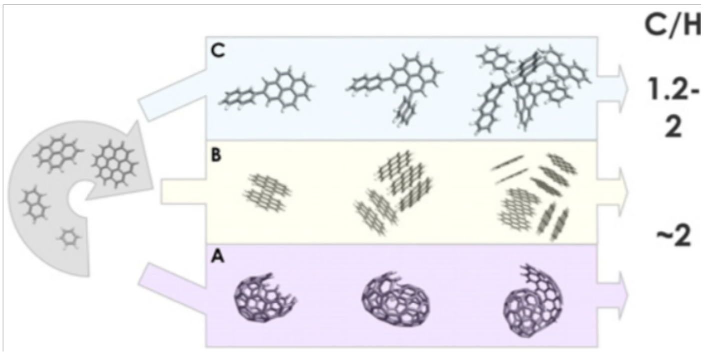

Figure 2.2: Conceptual mechanisms of soot particle inception. The illustration is adapted from [12].

Research over the past decade has tended to link soot nucleation with moderate-sized PAHs, as explained in Ref. [12] (see section 3.2.1). In a more recent work by Wang et al. [47], eight PAHs ranging from pyrene ($C_{16}H_{10}$)) to coronene ($C_{24}H_{12}$)) are involved in the nucleation process. Their model considers both homogeneous nucleation (self-addition of PAHs) and heterogeneous nucleation (collision of two different PAHs), thus constituting 36 nucleation reactions in total. The model was employed in an ethylene-air counterflow diffusion flames [47]. A different form can be found in the model of Blanquart et al. [46], where the self-collision of six different PAHs generates dimers, an intermediate particle used to form soot nuclei via self-collision and to contribute to soot mass by condensing upon the surface of larger soot particles.

Obviously, a very detailed model for soot nucleation is computationally expensive, which can be a significant problem when coupling with CFD, especially in turbulent flows. In practice, determining which model to employ is always a compromise between accuracy and CPU cost.

2.1.2 Surface growth and oxidation of soot

After soot nuclei are formed, their further growth depends heavily on the chemical reactions between gaseous species and the surface of soot particles. The simplified expressions for the surface growth in the early empirical models are outdated. Based on a number of fundamental studies on soot surface growth, a consensus has been reached that acetylene is the dominant species for the soot mass addition.

In the family of semi-empirical models, the associated reaction step can be described schematically as:

$$\mathrm{C_2H_2} + n\mathrm{C(s)} = (n+2)\mathrm{C(s)} + \mathrm{H_2} \tag{2.6}$$

Following the comprehensive studies by Harris and Weiner [13,48], a branch of models with empirical rate constants were proposed to calculate the surface growth rate. The most simplified form can be expressed as:

$$R_g = k_g S[\mathrm{C_2H_2}] \tag{2.7}$$

where the surface area S, rate constants k_g and acetylene concentration $[\mathrm{C_2H_2}]$ are the three major components, and R_g indicates the rate of surface growth. The surface growth in the above expression depends linearly on the surface area. Such a relation can be treated only as a simplification and does not hold in most cases. For example, Leung et al. [30] found that the linear dependence of surface growth on the surface area would significantly exaggerate the influence of surface area on the soot formation.

Thus they proposed a square root dependence of growth on the surface area to reduce the growth. Later on, in a subsequent study by Lindstedt [32], several growth models are compared, and the one independent of the surface area gave the best results in the context of that model. Another example can be found in the work by Brookes and Moss [49], in which growth was assumed to be proportional to S^n, and n was calibrated based on experiments.

Currently, OH and O_2 are considered as two main oxidising species of soot, although O is also included in some models. Similarly, a simplified global description can be described as:

$$\mathrm{C(s)} + \frac{1}{2}\,\mathrm{O_2} \longrightarrow \mathrm{CO} \tag{2.8}$$

$$\mathrm{C(s)} + \mathrm{OH} \longrightarrow \mathrm{CO} + \mathrm{H} \tag{2.9}$$

Two very first studies for O_2 oxidation were due to Nagle and Strick-Constable [16] and Lee et al. [50], and the most commonly used model for OH oxidation is due to Neoh et al. [17]. These studies are the backbone for the oxidation part in the currently prevalent soot kinetics, although authors generally introduce corrections to the rates in these models according to their need. For example, the first model proposed by Leung et al. [30] considered only the oxidation by O_2 but with an eight times enlargement for the oxidation rate proposed by Lee et al. [50], possibly to account for the impact of neglecting OH oxidation. The study of Liu et al. [51] considered oxidation by both species with further modifications.

In detailed models, the surface chemistry covers both the surface growth and oxidation step. The fundamental mechanism in current modelling community for soot growth is the HACA mechanism of Frenklach and coworkers [39, 40, 52]. It describes the soot surface constituting aromatic basal planes and edges sites. The H-abstraction happening on the surface would lead to an aryl radical site, which then is attacked by acetylene in a way similar to HACA mechanism in gaseous PAH formation. Including the oxidation, the following expressions are the basic form of HACA for soot surface reaction [41]:

$$\mathrm{C(s)-H+H \rightleftharpoons C(s)-+H_2} \tag{2.10}$$

$$\mathrm{C(s)-H+OH \rightleftharpoons C(s)-+H_2O} \tag{2.11}$$

$$\mathrm{C(s)-+H \longrightarrow C(s)-H} \tag{2.12}$$

$$\mathrm{C(s)-+C_2H_2 \longrightarrow C(s)-H+H} \tag{2.13}$$

$$\mathrm{C(s)-+O_2 \longrightarrow 2CO+products} \tag{2.14}$$

$$\mathrm{C(s)-+OH \longrightarrow CO+products} \tag{2.15}$$

where further modifications have been made mainly in the reaction rates, while in [53] the Eq. 2.12 is considered as a reversible reaction. In a recent study by Wang et al. [47], the radicals CH_3, C_3H_3 and C_2H are introduced as extra H-abstraction reactions. Still, the form above is the most prevalent HACA mechanism in today's soot modelling community, and the rate-limiting reactions in HACA are the hydrogen abstraction reactions.

In HACA mechanism, the rate equations associated with $\mathrm{C(s)-H}$ for a soot aggregate of size class i is [39]:

$$R_{g,i} = k_{g,s} C_g \alpha \chi_s S_i N_i \tag{2.16}$$

where $k_{g,s}$ is the per-site rate coefficient, C_g is the concentration of associated gas-phase species g, such as C_2H_2 in Eq. 2.13 or H in Eq. 2.12, χ_s is the number density of surface sites (i.e. number of sites per unit soot surface area) that are estimated to be 2.3×10^{19} sites/m^2, S_i is the surface area, N_i is the number density, and α is the fraction of surface sites that are available for reactions, a free parameter that is also interpreted as soot surface reactivity [54,55]. Effectively, the physical interpretation of the multiplication of α, χ_s, S_i and N_i is the concentration of available sites $\mathrm{C(s)-H}$. For reactions associated with $\mathrm{C(s)-}$, χ_s in Eq. 2.16 is replaced by the number density of radical χ_{s-} sites, which are determined by assuming steady state for C(s)− as:

$$\chi_{s-} = \frac{k_{2.10}[\mathrm{H}] + k_{2.11}[\mathrm{OH}]}{k_{-2.10}[\mathrm{H_2}] + k_{-2.11}[\mathrm{H_2O}] + k_{2.12}[\mathrm{H}] + k_{2.13}[\mathrm{C_2H_2}] + k_{2.14}[\mathrm{O_2}] + k_{2.15}[\mathrm{OH}]}\chi_s \tag{2.17}$$

where the k's subscripts refer to the per-site rate coefficient $k_{g,s}$ of the corresponding reactions, and the positive sign (omitted) and the negative sign represent forward and backward reaction respectively.

The surface reactivity α is of central importance in HACA mechanism. By design, one feature of the surface reactivity α is to correct the assumptions made in the surface growth scheme. The number density of surface sites χ_s was estimated based on the assumption that the surface is covered with benzene rings [39]. It was assumed that there are two sites per benzene ring length (2.46 Å). The distance between the benzene stacks is 3.51 Å. Thus χ_s was computed to be $2/(2.46 \times 3.51) = 0.23$ sites/Å, equivalent to 2.3×10^{19} sites/m^2. This value is essentially a theoretical maximum for soot surface sites, given that all of these sites are treated as armchair sites. For soot particles composed of stacks of four to eight-ring PAHs, a smaller value for χ_s is expected [55]. Another feature of α is to account for soot aging, as the C/H ratio of soot particles will increase and lead to less chemical reactivity [18]. Consequently, α reconciles the uncertainties of treating soot surface sites as corresponding sites on the benzene molecule. It is very difficult to estimate α from first principles, hence α was initially treated as a free parameter that can be adjusted to produce the best agreement between the predictions and experimental results. From a physical perspective, the value of α is bounded between zero and unity. Several forms of α can be found in the literature. For example, α was initially treated as a constant with different values for different flames [40], later it was modelled to depend on temperature [54] and particle size [41]. Several α models are summarised in Table. 2.1 for demonstration purpose. A comprehensive study investigating α is due to Veshkini et al. [55], in which the α model accounts for particle age. To reach a consensus for the modelling of α, further investigations are still needed.

Table 2.1: Several α models in HACA mechanism.

Proposed by	Formula	Value at 1700 K
Frenklach and Wang [39]	0.1	0.1
Appel et al. [41]	$\tan h(\mathrm{a}/\log\mu_1+\mathrm{b})$ [a]	0.93
Guo et al. [54]	$0.0045 \exp(9000/T)$	0.9
Dworkin et al. [8]	0.0078	0.078

[a] where μ_1 is the first size moment of the soot PSD, and a, b are fitted parameters that are function of temperature.

Apart from the acetylene route, the condensation of PAHs on the soot surface also contributes to the mass growth. As it is a heterogeneous gas-to-particle conversion process often modelled as the coagulation between soot particles and gaseous PAHs, the modelling of condensation depends on soot kinetic model. So far, there is no widely adopted condensation model in soot studies. A relatively recent condensation model employed in my study is presented in Section 4.1.2.

2.2 Population balance equation and its solution

The Population Balance Equation (PBE), also named as General Dynamic Equation (GDE), has found diverse applications in applications associated with particulate systems, and it is also of paramount importance in the study of aerosol dynamics, for its ability to describe the dynamics of a polydisperse particle system in terms of a distributed property (e.g. a measure of particle size, volume or mass). Moreover, particle morphology can also be accounted for if more properties such as the particle surface area and the number of primary particles are involved. The physical and chemical processes described by the PBE can be categorised in two classes. The first one covers the processes associated with particle transport in physical space, including convection, diffusion and thermophoresis; while the second one includes the physical and chemical processes that result in changes in particle property space at each spatial point, such as particle inception, continuous size change (e.g., surface growth, oxidation and condensation), particle combination (coalescence and aggregation), and sintering (the fusing of primary particles) and breakage. Due to the complex mathematical expression of the PBE, analytical solutions of PBE are rare. One requires an accurate numerical solution scheme for a successful application of PBE. General reviews of the associated topic can be found in Refs. [56–58], while in Refs. [23, 59] the coupling of PBE with reacting flows is reviewed. In this section, I aim to introduce the main concepts of the PBE and how it accounts for particle morphology. Specifically, I focus on the processes classified in the second class and discuss the PBE for a spatially homogeneous system. The challenges associated with the solution of PBE are emphasised in the end. The coupling with flow will be discussed in Section 2.3.4.

2.2.1 Formulation of the PBE

The first PBE appeared as a discrete form in the work of Smoluchowski [60] on coagulation of monodisperse colloids. That form is also called as the Smoluchowski equation in literature and is suitable for populations where polydispersity appears by continuous additions of monodisperse particles. Considering a volume v_0 as the smallest volume of the particle, a discrete representation of particle volume space v takes the form $v_i = iv_0$. Its associated concentration of particles of volume v_i can be defined as N_i. Subsequently, the Smoluchowski equation can be expressed as:

$$\frac{dN_i}{dt} = \frac{1}{2}\sum_{j=1}^{i-1} \beta_{j,i-j} N_j N_{i-j} - \sum_{j=1}^{\infty} \beta_{i,j} N_i N_j \tag{2.18}$$

where the first term of the right-hand side (R.H.S.) accounts for coagulation of all pairs of particles (smaller than v_i) whose sum of volumes yields v_i, and the second term is a sink term due to coagulation of particles of volume v_i with all the other particles. The coagulation kernel $\beta_{i,j}$ describes the probability of the collision between a particle of volume v_i and one of volume v_j (also referred as collision frequency), which will be addressed later in this section. The Smoluchowski equation described only coagulation. Later in the work by Friedlander [61], the method was extended to include surface processes such as condensation and evaporation of aerosols. These processes are described by adding or removing a single unit.

There are certain disadvantages in the discrete PBE formulation. The first one is that the discrete PBE does not apply to an aerosol system that covers a large range in the particle size space. For example, for a PBE that describes coagulation of particles ranging from 1 nm to 1 μm in diameter, 10^9 discrete units are needed. A large number of variables make it computationally prohibited to apply discrete PBE in many applications. The second one is that surface processes can involve a much smaller unit, thus increasing the number of discrete units significantly. For example, in the soot case, the smallest unit could be an acetylene C_2H_2. Consequently, the continuous PBE is developed to address the drawbacks mentioned above, in which the variable of the PBE is continuous.

For the continuous PBE, the number density $n(v,t)$ is defined as the number of particles having volume between v and $v + \delta v$ per unit of particle volume at time t. One can interpret $n(v,t)$ as a quantity per unit volume in particle volume space. Anticipating the coupling with fluid dynamics, a link between the number density concentration $n(v_i,t)$ and the particle number concentration N_i can be established as:

$$N_i = n(v_i)dv \tag{2.19}$$

Now, the final equation of a continuous PBE accounting for nucleation, surface growth and coagulation is given as:

$$\begin{aligned}\frac{\partial n}{\partial t} + \frac{\partial (Gn)}{\partial v} = B\delta(v - v_0) &+ \frac{1}{2}\int_0^v \beta(w, v-w)n(w)n(v-w)dw \\ &- n(v)\int_0^\infty \beta(v,w)n(w)dw\end{aligned} \tag{2.20}$$

where I omit the dependence where necessary for brevity. G represents the net rate of change of particle volume due to continuous processes such as surface growth and oxidation, and its role here is a convective velocity along the particle volume coordinate. B denotes the nucleation rate, and delta function $\delta(v - v_0)$ indicates that nucleation produces only particles of volume v_0. The last two terms on the R.H.S. of the equation address coagulation process, corresponding to the sums in the discrete PBE (Eq. 2.18), and possible forms of coagulation kernel $\beta(v, w)$ will be given later. In the case of soot, the PBE is associated with the chemical species, thus a proper coupling between PBE, species mass balance equations and chemical kinetics must be provided. In such cases, the nucleation, surface growth and oxidation rates are the functions of the species mass fractions that can be computed according to the kinetic models described in Section 2.1.

In the aerosol community, several extensions to Eq. 2.20 are available, for example, the terms describing breakage processes. In this section, however, I focus on the basic form as shown in Eq. 2.20 because the current work neglects the internal oxidation (thus oxidation-induced breakage). The PBE can also be extended to several dimensions, in which a joint distribution in terms of extra variables (e.g. surface area or chemical composition) is considered. By doing so, one obtains a more detailed description of particle properties compared to one dimension PBE. A specialised introduction regarding this topic will be given in Chapter 3. While it is not hard to formulate a multidimensional PBE, the detailed kinetics required for describing the processes in the additional dimensions is the main obstacle. And solving a multidimensional PBE is also a computationally expensive task.

In what follows, I present how coagulation is described. The form of coagulation kernel based on spherical particles in soot study will be introduced first, followed by its extension that accounts for the fractal-shaped aggregates.

2.2.1.1 Coagulation kernels

The collision behaviour of particles can be classified into different classes, based on the relative size of the particles compared to the mean free path λ_g of the carrier gas. For particles whose diameter d_p is much smaller than the mean free path of the gas ($d_\mathrm{p} \ll \lambda_g$), collisions take place in the free molecule regime, and the expression for collision frequency can be derived based on the kinetic theory of gases for collisions among molecules that act like rigid elastic spheres [57]:

$$\beta^f(v,w) = \left(\frac{3}{4\pi}\right)^{\frac{1}{6}} \left(\frac{6k_{\mathrm{B}}T}{\rho_p}\right)^{\frac{1}{2}} \left(\frac{1}{v}+\frac{1}{w}\right)^{\frac{1}{2}} \left(v^{\frac{1}{3}}+w^{\frac{1}{3}}\right)^2 \tag{2.21}$$

where ρ_p is the particle density and k_{B} is the Boltzmann constant.

For particles larger than the mean free path of the gas ($d_{\mathrm{p}} \gg \lambda_g$), the collisions are due to Brownian motion in the continuum regime, and the associated kernel has the following expression:

$$\beta^c(v,w) = \frac{2k_{\mathrm{B}}T}{3\mu} \left(\frac{1}{v^{\frac{1}{3}}}+\frac{1}{w^{\frac{1}{3}}}\right) \left(v^{\frac{1}{3}}+w^{\frac{1}{3}}\right) \tag{2.22}$$

where μ is the gas viscosity. A modification of Eq. 2.22 is available for particles in the continuum-slip regime [62]:

$$\beta^c(v,w) = \frac{2k_{\mathrm{B}}T}{3\mu} \left(\frac{\mathrm{Cu}(v)}{v^{\frac{1}{3}}}+\frac{\mathrm{Cu}(w)}{w^{\frac{1}{3}}}\right) \left(v^{\frac{1}{3}}+w^{\frac{1}{3}}\right) \tag{2.23}$$

where:

$$\mathrm{Cu} = 1 + 1.257\frac{2\lambda_g}{d_{\mathrm{p}}} \tag{2.24}$$

is the Cunningham correction factor for slip flow, and the numerical factor has been obtained by Davies [63]. In the above formulas, the gas mean free path can be approximated from the kinetic gas theory, based on the assumption that the gas composes of only a single component whose molecule behave like rigid elastic spheres [57, 64]:

$$\lambda_g = \frac{1}{\sqrt{2}\pi\sigma^2 N_m} \tag{2.25}$$

where σ and N_m represents the molecular diameter and the number of molecules per unit volume respectively. According to ideal gas law, N_m can be obtained as:

$$N_m = \frac{p}{kT} \tag{2.26}$$

A dimensionless number, Knudsen number Kn, is used to determine the regime of coagulation. Kn is defined as:

$$\mathrm{Kn} = \frac{2\lambda_g}{d_\mathrm{p}} \tag{2.27}$$

For Kn > 10, the particles are smaller than the mean free path of the gas and thus the coagulation kernel takes the form given in Eq. 2.21, while for Kn < 0.1 coagulation occurs due to Brownian motion, hence Eq. 2.22 must be employed. For coagulation in transition regime (0.1 < Kn < 10), a kernel β^t is formulated due to Fuchs [65], which, however, is replaced by a harmonic average approximation [62] in soot modelling:

$$\beta^t(v,w) = \frac{\beta^f(v,w)\beta^c(v,w)}{\beta^f(v,w) + \beta^c(v,w)} \tag{2.28}$$

For larger particles where inertial effects are considerable, other kernels such as laminar shear, turbulent shear and sedimentation are available. Since these kernels are not suitable for the usual size range of soot particles, their functional forms will not be given here.

2.2.1.2 Aggregate morphology

The collision of spherical soot particles above a certain size tends to form agglomerates and fractal aggregates. Since the mechanism of agglomeration is still unknown [15], majority of the studies consider only the fractal aggregates as a simplification. During this aggregation process, the shape of the primary particles is retained, although some continuous deformation is expected due to processes such as the fusing of primary particles and condensation. A proper description for the fractal aggregates is needed. In PBE, fractal aggregates are generally assumed to constitute primary particle of same diameter d_p and characterised by a fractal dimension D_f [57]:

$$n_{av} = A\left(\frac{d_g}{d_p}\right)^{D_f} \tag{2.29}$$

where n_{av} is the number of primary particles per aggregate, A is a proportionality constant, and d_g is a characteristic length such as the diameter of gyration or collision diameter. The fractal dimension value can be obtained from experiments or numerical studies (e.g. Monte Carlo simulations). $D_f = 3$ represents spherical particles and $D_f = 1$ represents chain-like aggregate particles. Typical values around 1.8 are prevalent in soot modelling [66, 67]. Finally, modified coagulation kernels which account for the fractal aggregate can be given as [62, 68]:

$$\begin{aligned} \beta^f(v,w) =& \sqrt{\frac{\pi k_\mathrm{B} T}{2\rho_s}} \left(\frac{1}{v} + \frac{1}{w}\right)^{\frac{1}{2}} (d(v) + d(w))^2 \\ \beta^c(v,w) =& \frac{2k_\mathrm{B}T}{3\mu}\left(\frac{\mathrm{Cu}(v)}{d(v)} + \frac{\mathrm{Cu}(w)}{d(w)}\right)(d(v) + d(w)) \end{aligned} \tag{2.30}$$

where $d(v)$ represents either the spherical particle diameter or the collision diameter of an aggregate that can be computed according to Eq. 2.29. It should be noted that, the fractal shape of aggregates must be accounted for when evaluating the surface area by which surface growth and oxidation rates are determined. A correction may be applied to account for a degree of overlapping [69] (e.g. see Eq. 3.20 in Section 3.3.1).

2.2.2 Challenges associated with the solution of the PBE

The PBE is a partial integro-differential equation that requires specialised methods for its solution. Analytical solutions are available only for special cases, while Monte-Carlo methods have been employed mostly in ideal reactors or one-dimensional laminar flames [70, 71]. For more complex two- and three-dimensional flows, the families of methods that have been employed are moment and discretisation (also called sectional) methods. In moment methods (Refs. [72–74] among others), one solves for the moments of the distribution, rather than for the PSD, and therefore the number of variables is kept to a minimum. However, moment methods do not predict the PSD, and furthermore the moment equations are unclosed, thus requiring closure assumptions. Sectional methods, on the other hand, solve directly for the PSD and do not require closure assumptions, but the discretisation of the PBE poses several unique challenges due to the presence of integral terms, thus requiring the development of specialised methods. The progenitor of sectional methods is the approach proposed by Bleck [75] in aerosol science, where a graphical procedure was used to illustrate the particle sectioning. The approach of Gelbard et al. [76], also initially developed for atmospheric aerosols, was later applied to soot formation in laminar premixed [77] and diffusion flames [78–80]. This implementation is, however, restricted in terms of the grid employed. The approach of Kumar and Ramkrishna [81] originates in the chemical engineering literature and has also been employed for soot formation in several studies, such as Refs. [82, 83]. This approach is not limited by the choice of grid and represents the distribution as a sum of delta functions, such that only certain particle sizes are allowed. Since a non-uniform grid cannot account for all aggregates formed, as they may not lie at grid nodes, correction factors are introduced to conserve any two moments by distributing the moments of aggregates to the two adjacent points. However, this approach places a priority on moment conservation at the expense of accuracy in the prediction of the distribution. Adaptive grid approaches have also been developed and applied to aerosols and soot [10, 11, 84, 85]. Liu and Rigopoulos [7] recently proposed a finite volume method that combines accurate prediction of the distribution with moment conservation in an arbitrary grid. A more extensive recent review of solution methods for the PBE with focus on soot modelling has been provided by Rigopoulos [23].

An important challenge in the population balance modelling of soot formation is the prediction of soot morphology. Once two particles have collided, the aggregate gradually transforms towards a spherical shape via the process known as sintering in materials science. As the fusing of soot particles involves different physical mechanisms, different terms such as coalescence and aggregation have been suggested for use in the soot literature [15]. Incipient liquid-like particles are subjected to instantaneous coalescence to form spherical particles. Larger primary particles form aggregates with fractal shapes, within which they are gradually being fused. Three concepts have appeared in the literature for extending the PBE to account for fractal aggregates, and these will be described in the following discussion.

The first approach is to employ the standard PBE with different aggregation kernels for spherical particles and aggregates, and to impose a cut-off size that separates the two types. This formulation can be solved with standard sectional methods and has been used in many studies, including Refs. [1, 7, 29, 86, 87]. There are, however, two important limitations associated with this approach. The first one is related to the model parameter, the cut-off size, which is an artificial conception that does not represent the physics of aggregation, assuming as it does instantaneous coalescence up to a considerable size and no further fusing afterwards. As mentioned, only very small particles coalesce instantaneously, while larger particles are fused with a finite timescale. The second limitation is related to the calculation of surface growth and oxidation, which is carried out in an inconsistent manner in the context of this approach. The size of the primary particles is assumed to be frozen once they reach the cut-off size, in spite of the fact that growth and oxidation continue to take place. Therefore the surface area, on which these processes depend, is inconsistent with the rate of change of the particle volume.

The second approach is the two-dimensional PBE proposed by Koch and Friedlander [88]. In this approach, the particle surface area is introduced as an additional independent variable in the PBE, and an additional term is introduced to account for sintering. A two-dimensional sectional method for the numerical solution of this formulation was developed and applied to the study of silica and titania nanoparticles by Xiong and Pratsinis [89] and Xiong et al. [90]. This approach is the most comprehensive one, but it is computationally expensive due to the two dimensions involved. While its employment in the context of an ideal reactor or a one-dimensional flame is affordable, its coupling with a three-dimensional CFD simulation would require excessive resources.

The third approach is to employ an additional dependent, rather than independent, variable, resulting in a system of coupled PBEs. This approach was pioneered by Rogak [91] and Tsantilis and Pratsinis [92], initially to describe the aerosol synthesis of nanoparticles such as silica and titania. The first of these studies employed an additional discrete PBE for the number of primary particles in the aggregates, while sintering was assumed to be instantaneous for particles smaller than a critical diameter. The second study employed an additional PBE for the aggregate surface area. The equation for the evolution of the surface area due to sintering is the same as the equation employed in the two-dimensional formulation. In the two-PBE approach, however, an average surface area is considered for each particle size section, in contrast to the two-dimensional PBE. In the work of Xiong and Pratsinis [89], where a sectional method was used to discretise the two-dimensional PBE, the effect of the number of surface area sections within a size section on the grain size predicted was found to be less than 5%. The two-PBE approach is computationally economical and suitable for coupling with CFD. Further studies with this approach on nanoparticle synthesis (silica and/or titania) employed either the surface area equation [93] or the number of primary particles [94, 95]. The method was also applied to soot [8, 55, 96–98] with the number of primary particles being the second equation.

There are several outstanding questions, however, regarding the two-PBE approach. The theoretical advantages over the one-PBE approach, which is customarily employed in turbulent flow simulations, and the sensitivity of the key parameters must be systematically investigated in laminar flames where reliable datasets are available and where the interaction between turbulence, chemistry and soot does not complicate matters further. The gradual fusing of primary particles that shapes the surface area of aggregates has rarely been studied in soot modelling, although it has been investigated in the modelling of silica and titania nanoparticle formation. Recently, Chen et al. [99] employed the sintering expression for SiO_2 in the context of a Monte-Carlo simulation of soot formation in laminar ethylene premixed flames, where the sintering parameters were adjusted to match soot experiments. On the other hand, Veshkini et al. [98] employed an expression originating in TiO_2 particles in the context of a sectional method for a sooting laminar diffusion flame. Since there is no experimental information on the rate of fusing of soot primary particles, however, the extrapolation of kinetics extracted from other inorganic nanoparticles warrants a systematic investigation. Finally, the structure and performance of numerical methods for the solution of two-PBE models must be analysed. In a problem as complex as soot formation in flows, establishing the accuracy of numerical methods is essential for preventing compensation of modelling and numerical errors. These facts bring about the first objective of this thesis.

2.3 Conservation equations for reacting flow

In this section, I briefly review the continuum mechanical description of a fluid flow with an immersed particulate phase. While the numerical solution of governing equations for flow motion, species, enthalpy and particles for laminar flames is relatively straightforward, their application to turbulent flames requires non-trivial modelling efforts, which will be discussed in Section 2.6 and in Chapter 5. Here, I will start by introducing the conservation equations and the chemical source terms. Subsequently, I summarise the general form of the conservation equations that is frequently employed in practical applications.

For notational brevity, the Einstein summation convention is adopted for the description of the following math formulae. The instantaneous velocity $u_j(\mathbf{x}, t)$, the pressure $p(\mathbf{x}, t)$ and the fluid density $\rho(\mathbf{x}, t)$ at a spatial location $\mathbf{x}$ in the physical domain and a point in time t are introduced as the dependent variables in view of an Eulerian formulation. The dependence on $\mathbf{x}$ and t will be omitted except when necessary. The conservation equations for mass, momentum, reactive scalars (gaseous species and enthalpy) and particles are presented in Cartesian coordinates.

2.3.1 The conservation law of fluid motion

Because the mean free path of the molecules is smaller than the smallest scales of the flow field, the concept of continuum applies, and the fluid particle can be treated as an ensemble of molecules, i.e., a volume average of molecules. Subsequently, the flow field can be described by the conservation equations for mass and momentum:

$$\frac{\partial \rho}{\partial t} + \frac{\partial \rho u_j}{\partial x_j} = 0 \tag{2.31}$$

$$\frac{\partial \rho u_i}{\partial t} + \frac{\partial \rho u_i u_j}{\partial x_j} = -\frac{\partial p}{\partial x_i} + \frac{\partial \tau_{ij}}{\partial x_j} + \rho g_i \tag{2.32}$$

where $i = 1, 2, 3$ indicating three directions in Cartesian coordinates, g_i denotes the body forces per unit volume (e.g. gravity), and τ_{ij} represents the viscous stress tensor for a Newtonian fluid where stress and rate of strain for a fluid particle are linear:

$$\tau_{ij} = \mu \left(\frac{\partial u_i}{\partial x_j} + \frac{\partial u_j}{\partial x_i} \right) - \frac{2}{3} \mu \frac{\partial u_k}{\partial x_k} \delta_{ij} \tag{2.33}$$

where δ_{ij} is the Kronecker delta, and μ is the viscosity of the fluid.

2.3.2 Governing equation for species mass fraction

In reactive flow, the conservation of each species k is of interest, and the governing equation for the species k is generally described in terms of its mass fraction Y_k:

$$\frac{\partial \rho Y_k}{\partial t} + \frac{\partial \rho (u_j + v_{k,j}) Y_k}{\partial x_j} = \rho \dot{\omega}_k \tag{2.34}$$

where $v_{k,j}$ is the diffusion velocity of species k along j-th direction, $\dot{\omega}_k$ represents the scalar production/destruction source term. Note that in here and what follows the summation does not imply in species index k. By definition, in the context of the mixture-average formulations, the diffusion velocity can be written as [100]:

$$v_{k,j} = -\frac{D_k^m}{X_k}\frac{\partial X_k}{\partial x_j} - \frac{D_k^m}{X_k}(X_k - Y_k)\frac{1}{p}\frac{\partial p}{\partial x_j} - \frac{D_k^T}{\rho Y_k}\frac{1}{T}\frac{\partial T}{\partial x_j} \tag{2.35}$$

where X_k is the mole fraction for species k, D_k^T is the thermal diffusion coefficient for species k due to the temperature gradient, and D_k^m represents the diffusion coefficient for the species k into the multi-component mixture due to Fick's law (i.e. the diffusion is due to the gradients of species concentration). The first and second terms in the R.H.S. of Eq. 2.35 represent the diffusion due to species concentration gradient and the diffusion due to pressure gradient respectively, while the latter is often neglected in the case of laminar diffusion flames in the open air. The third term in the R.H.S. of Eq. 2.35 accounts for the Soret effect (mass diffusion due to temperature gradients). It must be noted that the modelling of species diffusion is complex and is extensively discussed; one may refer Ref. [101] for more details. Formally, substituting Eq. 2.35 into Eq. 2.34 and rearranging the equation, a comprehensive description for the governing equation for species mass fraction can be written as:

$$\begin{aligned}\frac{\partial \rho Y_k}{\partial t} + \frac{\partial \rho u_j Y_k}{\partial x_j} =& \underbrace{\frac{\partial}{\partial x_j}\left(\rho D_k^m \frac{\partial Y_k}{\partial x_j}\right)}_{\text{Differential diffusion}} + \underbrace{\frac{\partial}{\partial x_j}\left(\rho D_k^m \frac{1}{\bar{W}}\frac{\partial \bar{W}}{\partial x_j}\right)}_{\text{Molecular weight}} \\ &+ \underbrace{\frac{\partial}{\partial x_j}\left(D_k^T \frac{1}{T}\frac{\partial T}{\partial x_j}\right)}_{\text{Thermophoresis}} + \rho\dot{\omega}_k\end{aligned} \tag{2.36}$$

where the diffusion due to pressure gradient is neglected, and $\bar{W}$ denotes the average molecular weight of the mixture.

2.3.3 Governing equation for energy

There are several different forms of governing equation for energy. A commonly adopted form in reactive flow is based on the total enthalpy h, from which the temperature can be determined [101]:

$$\frac{\partial \rho h}{\partial t} + \frac{\partial \rho u_j h}{\partial x_j} = \frac{\partial p}{\partial t} + \tau_{ij}\frac{\partial u_i}{\partial x_j} + \dot{Q} - \frac{\partial q_j}{\partial x_j} \tag{2.37}$$

where the first term on the R.H.S. can be neglected for low Mach number flows. The second term on the R.H.S. represents viscous heating, which is also negligible under the low Mach number assumption. The source term $\dot{Q}$ is the heat source that may include radiation and external heat source. The energy flux q_j encompasses the contributions due to the inter-diffusion of species, thermal conduction, and the Dufour effect, which is due to a mass concentration gradient occurring as a coupled effect of irreversible processes (it can be seen as the reciprocal phenomenon to the Soret effect):

$$q_j = \sum_{k=1}^{K} \rho Y_k h_k u_{k,j} - \lambda \frac{\partial T}{\partial x_j} - \sum_{k=1}^{K} \frac{RT}{W_k X_k} D_k^T \left[\frac{\partial X_k}{\partial x_j} + (X_k - Y_k)\frac{1}{p}\frac{\partial p}{\partial x_j} \right] \tag{2.38}$$

where h_k represents the specific enthalpy of species k, W_k represents the molecular weight of species k, λ represents the thermal conductivity of the mixture, and R represents the universal gas constant. Similarly, neglecting the terms associated with pressure gradient and substituting Eq. 2.38 into Eq. 2.37 with non-trivial manipulations, a comprehensive description for the energy governing equation is written as:

$$\begin{aligned} \frac{\partial \rho h}{\partial t} + \frac{\partial \rho u_j h}{\partial x_j} = & \underbrace{\frac{\partial}{\partial x_j}\left(\rho D^T \frac{\partial h}{\partial x_j}\right) - \sum_{k=1}^{K} \frac{\partial}{\partial x_j}\left[\rho (D^T - D_k^m) h_k \frac{\partial Y_k}{\partial x_j}\right]}_{\text{Differential diffusion}} \\ & + \underbrace{\sum_{k=1}^{K} \frac{\partial}{\partial x_j}\left(\rho D_k^m h_k Y_k \frac{1}{\bar{W}}\frac{\partial \bar{W}}{\partial x_j}\right)}_{\text{Molecular weight}} + \underbrace{\sum_{k=1}^{K} \frac{\partial}{\partial x_j}\left(\frac{D_k^T h_k}{T}\frac{\partial T}{\partial x_j}\right)}_{\text{Thermophoresis}} \\ & + \underbrace{\sum_{k=1}^{K} \frac{\partial}{\partial x_j}\left(\frac{RT}{W_k X_k} D_k^T \frac{\partial X_k}{\partial x_j}\right)}_{\text{Dufour effect}} + \dot{Q} \end{aligned} \tag{2.39}$$

where D^T, which is different from the thermal diffusion coefficient D_k^T for species k, represents thermal diffusivity of the mixture. The radiation loss is included in the source term $\dot{Q}$.

2.3.4 Spatially dependent PBE

In practical applications, the governing equations for particle, or inhomogeneous population balance equation, must be solved with other governing equations. Since the homogeneous PBE (Eq. 2.20) is a statement of conservation for particle number concentration in particle property space (e.g. volume space v), additional terms accounting for its spatial transport are needed. Formally, I consider a spatially varying number density, $n(v, \mathbf{x}, t)$, and augment the PBE with terms associated with spatial transport:

$$\begin{aligned}\frac{\partial n}{\partial t} + \frac{\partial (Gn)}{\partial v} + \frac{\partial [(u_j + u_j^t)n]}{\partial x_j} &= \frac{\partial}{\partial x_j}\left(D_p \frac{\partial n}{\partial x_j}\right) + B\delta(v - v_0) \\ &+ \dot{C} + \frac{1}{2}\int_0^v \beta(w, v-w)n(w)n(v-w)dw - \int_0^\infty \beta(v,w)n(v)n(w)dw \qquad (2.40)\end{aligned}$$

where $\dot{C}$ encompasses source terms due to other processes such as condensation, u_j^t represents the thermophoretic velocity due to the temperature gradient, and D_p denotes the kinematic diffusivity for the particle. Here, Eq. 2.40 is a volume-based description for the number density. In practice, it is advantageous to switch to a mass-based definition of the number density $n_\rho(v, \mathbf{x}, t)$ per unit of mixture mass, given as:

$$n_\rho(v, \mathbf{x}, t) = \frac{n(v, \mathbf{x}, t)}{\rho(\mathbf{x}, t)} \qquad (2.41)$$

By doing so, the parts related to physical transport in the spatially dependent PBE are in accordance with that of the governing equations for species and enthalpy, and such expression is also beneficial to the mathematical formulation in turbulent flame, as discussed in [11]. The functional forms for the rate of the surface reaction G, condensation process C and nucleation B will be demonstrated in detail in Section 4.1, together with a comprehensive demonstration of the soot kinetic model.

2.3.5 Chemical source term

Generally, gas-phase chemical reaction source terms $\dot{\omega}_k$ appeared in Section 2.3.2 are highly non-linear. Their standard expression begins with a set of I elementary reversible (or irreversible) reactions.

$$\sum_{k=1}^{K} \upsilon'_{k,i} A_k \rightleftharpoons \sum_{k=1}^{K} \upsilon''_{k,i} A_k \qquad (i = 1, \ldots, I) \tag{2.42}$$

where the stoichiometric coefficient $\upsilon_{k,i}$ are inter numbers, and A_k is the chemical symbol for the kth species. The superscript $'$ denotes forward stoichiometric coefficients, while $''$ denotes reverse stoichiometric coefficients. An elementary reaction involves typically only three to four species, thus the $\upsilon_{k,i}$ can be relatively sparse for a large set of reactions. Now the production rate $\dot{\omega}_k$ of the kth species as a summation of the rate of progress variables for all reactions containing the kth species can be written as:

$$\dot{\omega}_k = \sum_{i=1}^{I} (\upsilon''_{k,i} - \upsilon'_{k,i}) q_i \qquad (k = 1, \ldots, K) \tag{2.43}$$

where the rate of progress variable q_i for the ith reaction is determined by the difference of the forward and reverse rates as:

$$q_i = k_{f,i} \prod_{k=1}^{K} [A_k]^{\upsilon'_{k,i}} - k_{r,i} \prod_{k=1}^{K} [A_k]^{\upsilon''_{k,i}} \qquad (k = 1, \ldots, K) \tag{2.44}$$

where $[A_k]$ represents the molar concentration of the kth species, and $k_{f,i}$ and $k_{r,i}$ are the forward and reverse rate constants of the ith reaction. The forward rate constants $k_{f,i}$ have the following Arrhenius temperature dependence:

$$k_{f,i} = a_i T^n \exp\left(-\frac{E_i}{RT}\right) \tag{2.45}$$

where the pre-exponential factor a_i, the temperature exponent n, and the activation energy E_i are specified. In thermal systems, the reverse rate constants $k_{r,i}$ are related to the forward rate constants through the equilibrium constants $K_{c,i}$ by:

$$k_{r,i} = \frac{k_{f,i}}{K_{c,i}} \tag{2.46}$$

where the equilibrium constants $K_{c,i}$ are determined from the thermodynamic properties. This study adopts the standard Chemkin subroutines to carry out the calculation for the reaction rates.

2.3.6 The simplified transport equations for reactive scalars

The comprehensive form of the governing equations for species and enthalpy can be simplified according to the practical applications. When the local average molecular weight does not vary a lot throughout the reacting flow field, which is the case for the flame with light species being fuel (e.g. CH_4 or C_2H_2), the second term in the r.h.s. of Eq. 2.36 is often neglected, and the thermal diffusion coefficient D_k^T can also be neglected as it is a function that depends on the difference of species molecular weight. Thus, the governing equation for species follows:

$$\frac{\partial \rho Y_k}{\partial t} + \frac{\partial \rho u_j Y_k}{\partial x_j} = \frac{\partial}{\partial x_j}\left(\rho D_k^m \frac{\partial Y_k}{\partial x_j}\right) + \rho \dot{\omega}_k \tag{2.47}$$

and the governing equation for enthalpy, neglecting terms due to molecular weight, thermophoresis and Dufour effect, can be simplified to:

$$\frac{\partial \rho h}{\partial t} + \frac{\partial \rho u_j h}{\partial x_j} = \frac{\partial}{\partial x_j}\left(\rho D^T \frac{\partial h}{\partial x_j}\right) - \sum_{k=1}^{K} \frac{\partial}{\partial x_j}\left(\rho (D^T - D_k^m) h_k \frac{\partial Y_k}{\partial x_j}\right) + \dot{Q} \tag{2.48}$$

Formally, Eqs. 2.31, 2.32, 2.47, 2.48 and 2.40 form a complete equation system that can be discretised directly in the laminar flames.

In turbulent flames, further simplification is possible. It is common to assume that all the species have the same mixture diffusion coefficient, to simplify the differential diffusion whose contribution is relatively small compared to that due to turbulent viscosity. By doing so, the governing equation for species in turbulent flames can be formulated as:

$$\frac{\partial \rho Y_k}{\partial t} + \frac{\partial \rho u_j Y_k}{\partial x_j} = \frac{\partial}{\partial x_j}\left(\rho D_m \frac{\partial Y_k}{\partial x_j}\right) + \rho \dot{\omega}_k \tag{2.49}$$

where D_m denotes the diffusion coefficient of the mixture. Following the same assumption and assuming a unity Lewis number, the governing equation for enthalpy in turbulent flames can be written as:

$$\frac{\partial \rho h}{\partial t} + \frac{\partial \rho u_j h}{\partial x_j} = \frac{\partial}{\partial x_j}\left(\rho D_m \frac{\partial h}{\partial x_j}\right) + \dot{Q} \tag{2.50}$$

Consequently, the species and energy conservation equations, Eq. 2.49 and Eq. 2.50, can be reformulated in terms of a general reactive scalar $\mathbf{\Phi} = (\phi_1, \ldots, \phi_{n_s})$, where n_s is the number of scalars (total number of species plus one due to enthalpy) required to describe the system:

$$\frac{\partial \rho \phi_s}{\partial t} + \frac{\partial \rho u_j \phi_s}{\partial x_j} = \frac{\partial}{\partial x_j}\left(\rho D_m \frac{\partial \phi_s}{\partial x_j}\right) + \rho \dot{\omega}_s \tag{2.51}$$

where $\dot{\omega}_s$ represents the source term for the reactive scalars. Formally, Eqs. 2.31, 2.32, 2.51, and 2.40 provide a system of conservation equations for turbulent flames, to be processed under the framework of LES. Further modelling details associated with LES will be presented in Chapter 5.

2.4 Fundamentals of turbulent flow

Turbulent reactive flows with soot formation are encountered in many industrial applications of engineering and environment importance. While increasingly stringent regulations call for control of the number density of soot particles, there are other industrial processes in which soot particles of a certain size are desirable. In either case, soot models must be coupled with turbulent reacting flows, which makes it one of the most challenging tasks in the combustion community for several reasons. Without introducing soot particles into the problem, there is already a wide range of coupled problems involved in turbulent flames. For example, the fluid dynamics of the reacting flow must be well resolved to capture the mixing between reactive species and all transport phenomena such as heat transfer, convection, molecular diffusion and turbulent transport. Detailed chemical reaction mechanisms are also required to describe the formation of the combustion products, and radiative heat transfer due to certain species is significant. The coupling of the soot model with turbulent flow adds another level of complexity, as one needs to address the non-linear interactions between turbulence, chemistry and soot.

The following section aims to present a general background of the topic, identify the questions and modelling issues for readers that are not familiar with the topic. I will introduce first the general feature of turbulent motions, followed by a summary of the numerical approaches for turbulence modelling. Next, I demonstrate the LES formalism for variable-density flows, which is the basis for my turbulent flame application. In the Section 2.5.3, I will discuss the main obstacles that one needs to address when combustion is coupled with turbulent flows and the currently most prevalent methods that are adopted to address the turbulence-chemistry interaction, i.e., the closures for the chemical source term. Finally, in Section 2.6, the challenges associated with the interactions between turbulence, chemistry and soot will be discussed in detail.

2.4.1 Overview of turbulent motion

Unlike a laminar flow, where the fluid flows in an organised manner without disruption, a turbulent flow is characterised by chaotic fluctuations in flow velocity, pressure and all other variables. Observations, dating back to the nineteenth century by Reynolds, showed that turbulence is triggered when the inertial forces outweigh the fluid viscous damping. The dimensionless Reynolds number is used to characterise the flow pattern, written as:

$$\mathrm{Re} = \frac{uL}{\nu} \tag{2.52}$$

where u and L, respectively, denote a characteristic velocity and a characteristic length scale of the flow, and $\nu = \mu/\rho$ is the kinematic viscosity of the fluid. The Reynolds number is of great importance in turbulent flows as it is used to judge whether the flow is laminar or turbulent.

One of the cornerstones in turbulence theories, due to Richardson [102], is the motion that the turbulence can be considered to be composed of eddies of different sizes. Eddies of size l have a characteristic velocity $u(l)$ and timescale $\tau(l) = l/u(l)$. Large eddies, frequently with high Reynolds number and negligible viscosity effects, are unstable and break up, continually transferring energy to smaller eddies. These smaller eddies undergo similar processes and pass the energy to even smaller eddies. This energy cascade continues until the Reynolds number is small enough such that the eddy motion is stable and molecular viscosity becomes effective again in dissipating the kinetic energy. This picture introduces a key parameter that appeared in most combustion models: the rate of dissipation ε, which is a measure of viscous dissipation of turbulent kinetic energy. The ε is determined by the transfer of energy from the largest eddies of length scale l_0, characteristic velocity u_0. These eddies contain kinetic energy of order u_0^2 and timescale $\tau_0 = l_0/u_0$, thus the rate of energy transfer can be considered to scale as $u_0^2/\tau_0 = u_0^3/l_0$. This definition indicates that ε scales as u_0^3/l_0, independent of ν, which is consistent with the experimental observations in free shear flows [103]. Moreover, it is well accepted, due to Kolmogorov hypotheses [104], that as the length scale l decreases, both the velocity and time scales of the eddies decrease.

According to the Kolmogorov hypotheses [104], turbulent eddies can be categorised into two size ranges depending on their distinctive nature of motions. The large eddies are anisotropic and are generally affected by the boundary conditions of the flow. They will gradually lose their directional information and geometry determined by the mean flow field and the boundary as the energy passes down the cascade, until reaching a point where the statistics of the small scale motions are isotropic. Here, I introduce a length scale l_E to separate the anisotropic large eddies ($l_E < l$) and isotropic small eddies $l < l_E$. As stated in Kolmogorov's first similarity hypothesis [104], the locally isotropic turbulence can be uniquely determined by ε and ν. The size range $l < l_E$ is referred to as the universal equilibrium range, while its counterpart is referred to as the energy-containing range [103]. In the universal equilibrium range, the timescales τ are small compared with τ_0, indicating that the small eddies adapt fast to sustain a dynamic equilibrium with the energy transferred by the large eddies and dissipated by viscosity.

To characterise the size of the smallest eddies that are dissipating energy, Kolmogorov introduced the Kolmogorov length scale η, velocity scale u_η and timescale τ_η [104]:

$$\eta = \left(\frac{\nu^3}{\varepsilon}\right)^{1/4} \tag{2.53}$$

$$u_\eta = (\varepsilon\nu)^{1/4} \tag{2.54}$$

$$\tau_\eta = \left(\frac{\nu}{\varepsilon}\right)^{1/2} \tag{2.55}$$

These definitions indicate that the Kolmogorov scales characterise the smallest dissipative eddies in two identities. First, the Reynolds number based on these scales is written as:

$$\mathrm{Re}_\eta = \frac{\eta u_\eta}{\nu} \tag{2.56}$$

where, according to Eq. 2.53 and Eq. 2.54, the value of Re_η equals unity, which is consistent with the notion that the energy cascade proceeds to the smallest scales until the dissipation due to viscosity is effective. Second, the dissipation rate ε can be expressed as:

$$\varepsilon = \nu(\frac{u_\eta}{\eta})^2 = \frac{\nu}{\tau_\eta^2} \tag{2.57}$$

where the expression of $(u_\eta/\eta) = 1/\tau_\eta$ indicating a consistent characterisation of the velocity gradients of the dissipative eddies. On the small scales, the turbulent velocity fields are statistically identical when they are scaled by the Kolmogorov scales.

Moreover, the ratios of the smallest to the largest scales scale with Reynolds number:

$$\frac{\eta}{l_0} \sim \mathrm{Re}^{-3/4} \tag{2.58}$$

$$\frac{u_\eta}{u_0} \sim \mathrm{Re}^{-1/4} \tag{2.59}$$

$$\frac{\tau_\eta}{\tau_0} \sim \mathrm{Re}^{-1/2} \tag{2.60}$$

Obviously, at high Reynolds number, the scales of the smallest eddies is very small. As will be discussed in the next section, this picture makes DNS in high Reynolds number applications intractable.

At sufficiently high Reynolds number, there is a range of scales l that are very large compared with η, but very small compared with l_0, i.e., $\eta \ll l \ll l_0$. The Reynolds number $lu(l)/\nu$ of these eddies is large, which means that the viscosity imposes trivial impact on their motion. Subsequently, as stated in Kolmogorov's second similarity hypothesis [104], the statistics of the motion of eddies of size $\eta \ll l \ll l_0$ have a universal form that is uniquely determined by ε, but independent of ν. At this point, I can introduce a length scale l_D, which splits the universal equilibrium range $l < l_E$ into two subranges: the dissipation range ($l < l_D$) and inertial range ($l_D < l < l_E$). According to the second similarity hypothesis, motions in the inertial range are determined only by inertial effects, while only motions in the dissipation range are responsible for all of the dissipation. A schematic illustration is shown in Fig. 2.3.

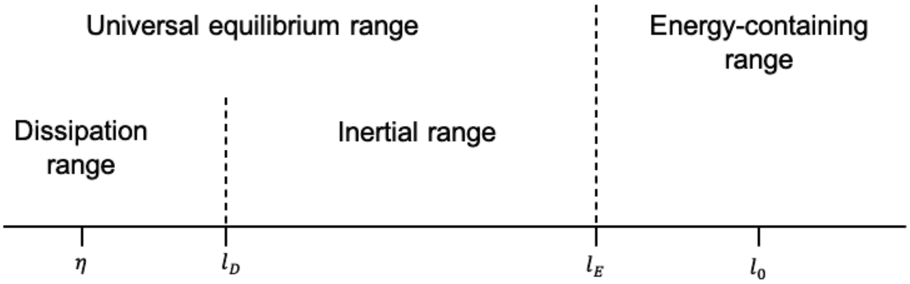

Figure 2.3: A schematic illustration of eddy size ranges with various length scales (on a logarithmic scale).

When describing turbulent motions of various scales, the notions of energy cascade and Kolmogorov hypotheses provide an invaluable framework to theoretical study and numerical modelling. Readers may refer to Ref. [103] for a comprehensive description regarding various scales of turbulent motion.

2.4.2 Numerical approaches associated with turbulent flow

The ultimate objective in a numerical study is to obtain a model or approach that is quantitatively accurate and computationally affordable to predict quantities of interest. Due to the chaotic flow pattern associated with turbulence, a simple analytic method is not possible in applications of practical relevance. In most cases, the governing partial differential equations are solved numerically, with the specification of the appropriate initial boundary conditions. At present, the numerical approaches solving the equations of motion can be classified into three main categories:

- Direct Numerical Simulation (DNS)
- Large Eddy Simulation (LES)
- Reynolds Averaged Navier Stokes Equations (RANS)

In DNS, all the scales of motion must be resolved without further modelling. By directly discretising and solving the Navier-Stokes equations, it is conceptually the simplest and most accurate method. However, the computational cost is also extremely high, as the computational domain has to be fine enough to capture the Kolmogorov scales that scale with Re as indicated in Eqs. 2.58, 2.59 and 2.60. The challenge is even severe when the reactive scalars of different characteristic chemical timescales are involved. At present, DNS is limited to applications of low to moderate Reynolds number and relatively simple geometry. Nevertheless, it is still a powerful research tool that can provide invaluable, detailed data not available from experiment studies for model validations in RANS and LES.

RANS is the oldest method for modelling turbulence. It can be seen as a statistical method, in which the partial differential governing equations are averaged to formulate transport equations for the mean variables of interest. Conceptually, each quantity ϕ associated with the flow can be decomposed into a time-averaged mean value $\langle\phi\rangle$ and a statistical fluctuation $\phi^{'}$ (this process is also known as Reynolds decomposition):

$$\phi = \langle\phi\rangle + \phi^{'} \qquad \text{with} \quad \langle\phi^{'}\rangle = 0 \tag{2.61}$$

Note that $\langle\rangle$ is used to denote time-average. Introducing the Reynolds decomposition into the governing equations and averaging, a set of transport equations for the mean quantities with unclosed terms appears. Various models have been proposed to close the equation system, e.g., the most prevalent $k-\epsilon$ model by Jones and Launder [105]. Since the local fluctuations and turbulent structures are integrated into time-averaged mean quantities, these structures are no longer exist. Thus RANS prediction provides considerably less information compared with DNS. However, they are much more affordable and now are applied as a standard tool in the industry.

The knowledge of steady statistical means is indeed not always sufficient, especially when one needs an accurate prediction, for example, of pollutant associated with complicated flow patterns such as swirling flows, recirculation regions and other flows in which large-scale unsteadiness is significant. This brings about the LES, which can be seen as a compromise between DNS and RANS in terms of accuracy and computational cost. In LES, the turbulent fields are separated into large-scale resolved and small-grid-scale (SGS) unresolved contributions. The dynamics of the large-scale motions are computed directly, while the influence of the small-scale motions (which is considered to have a universal character) are represented by simple models. The separation of the scales is achieved by a filtering process, which can be seen as an averaging of quantities in a given volume of size Δ in physical space (or a cut-off filtering in the wavenumber space in the LES energy spectrum, see Ref. [103]):

$$\bar{\phi}(\mathbf{x}, t) = \int_{\Omega} G(\mathbf{x} - \mathbf{x}')\phi(\mathbf{x}', t)d\mathbf{x}' \tag{2.62}$$

where the LES filtering is denoted with $\bar{\cdot}$, and the filter function G must be positive and definite so that the filtered values of scalars are bounded, and the nature of source terms is preserved. Frequently, $G \geq 0$ integrates to unity, indicating that it has the properties of a PDF. The integration is defined over the entire flow domain Ω, and the filter function has a characteristic width of Δ, which is often defined as the cubic root of the local cell volume. The simplest box filter for filter function $G(\mathbf{x}, \mathbf{x}')$ can be written as:

$$\begin{aligned} G(\mathbf{x}-\mathbf{x}') &= \frac{1}{\Delta^3} \qquad \text{for } |\mathbf{x}-\mathbf{x}'| \leq \frac{\Delta}{2} \\ &= 0 \qquad \text{otherwise} \end{aligned} \tag{2.63}$$

This box filter applies a cell-average within the cell volume and is complementary to a finite volume-based spatial discretisation scheme, which is the basis of an in-house CFD code BOFFIN. Since the filter function Eq. 2.63 is homogeneous (i.e., independent of $\mathbf{x}$) and varies smoothly with position, the filtering operation Eq. 2.62 obtains the following commutation properties:

$$\overline{\frac{\partial \mathbf{u}(\mathbf{x},t)}{\partial t}} = \frac{\partial \overline{\mathbf{u}}(\mathbf{x},t)}{\partial t} \tag{2.64}$$

$$\overline{\frac{\partial \mathbf{u}(\mathbf{x},t)}{\partial x_i}} = \frac{\partial \overline{\mathbf{u}}(\mathbf{x},t)}{\partial x_i} \tag{2.65}$$

By design, all the scales above the filter size Δ are resolved directly, while the smaller scales are modelled. Ideally, the filter size Δ is supposed to be smaller than l_E, the size of the smallest energy-containing motions as presented in Fig. 2.3. The unclosed terms due to LES filtering in the governing equations require further modelling, e.g., the standard Smogorinsky model.

2.4.3 LES for variable-density flows

In turbulent flames, fluctuations of density are observed and can be treated by a density-weighted average, Favre average, to circumvent the closure problem posed by the correlations between density fluctuations and scalar fluctuations in RANS. In LES, a density-weighted filtering, named Favre filtering, can be applied to address the strong density variations in the unresolved scales. The definition of Favre filtering of a scalar $\phi(\mathbf{x}, t)$ follows:

$$\widetilde{\phi}(\mathbf{x}, t) = \frac{\overline{\rho(\mathbf{x}, t)\phi(\mathbf{x}, t)}}{\overline{\rho}(\mathbf{x}, t)} \tag{2.66}$$

With the amid of Eq. 2.64, 2.65 and 2.66, applying the LES filtering $\overline{\cdot}$ to the continuity and momentum equations (Eq. 2.31 and 2.32) results in:

$$\frac{\partial \overline{\rho}}{\partial t} + \frac{\overline{\rho}\widetilde{u}_j}{\partial x_j} = 0 \tag{2.67}$$

$$\frac{\partial \overline{\rho}\widetilde{u}_i}{\partial t} + \frac{\partial \overline{\rho}\widetilde{u}_i\widetilde{u}_j}{\partial x_j} = -\frac{\partial \overline{p}}{\partial x_i} + \frac{\partial(\widetilde{\tau}_{ij} - \tau^*_{ij})}{\partial x_j} + \overline{\rho}g_i \tag{2.68}$$

where $\widetilde{\tau}_{ij}$ denotes the resolved viscous stress tensor associated with the Favre-filtered velocity field $\widetilde{\mathbf{u}}(\mathbf{x}, t)$ [106] and $\tau^*_{ij} = \overline{\rho}(\widetilde{u_i u_j} - \widetilde{u}_i\widetilde{u}_j)$ represents the SGS stress tensor which involves the unresolved SGS term and thus requires modelling. Since the unresolved SGS stresses in LES are expected to be small if the filter width is chosen in such a manner that most of the energy-containing spectrum is resolved, applying simple closure models appears to be a reasonable option. In my work, I also adopt the standard Smagorinsky model for the deviatoric part of the SGS stress tensor [106]:

$$\tau^*_{ij} - \frac{\delta_{ij}}{3}\tau^*_{kk} = -2\mu_{sgs}\widetilde{e}_{ij} \tag{2.69}$$

with the SGS turbulent viscosity μ_{sgs}:

$$\mu_{sgs} = \overline{\rho}(C_S\Delta)^2\,||\widetilde{e}_{ij}|| \tag{2.70}$$

where the symbol $||.||$ represents the Frobenius norm, the resolved rate of strain tensor $\widetilde{e}_{ij} = 0.5\left(\frac{\partial \widetilde{u}_i}{\partial x_j} + \frac{\partial \widetilde{u}_j}{\partial x_i}\right)$ and the Smagorinsky constant is $C_S = 0.1$. As with the isotropic part of the viscous stress, the isotropic part of the SGS stress is absorbed into the filtered pressure [106]. Thus, the Favre-filtered momentum equation follows:

$$\frac{\partial \overline{\rho}\widetilde{u}_i}{\partial t} + \frac{\partial \overline{\rho}\widetilde{u}_i\widetilde{u}_j}{\partial x_j} = -\frac{\partial \overline{p}}{\partial x_i} + \frac{\partial}{\partial x_j}\left(2\mu\widetilde{e}_{ij}\right) + \frac{\partial}{\partial x_j}\left(2\mu_{sgs}\widetilde{e}_{ij}\right) + \overline{\rho}g_i \tag{2.71}$$

In my turbulent flame application (Chapter 5 and 6), Eq. 2.67 and Eq. 2.71 represent the closed form of the conservation equations for the flow field.

2.5 Turbulence-chemistry interaction

In turbulent flames, the processes for which closure assumptions are needed include turbulent transport, as discussed in the previous section, and the so-called turbulence-chemistry interaction, which is the main challenge in modelling of turbulent combustion. The latter refers to the highly non-linear feature of the chemical source term $\dot{\omega}_k$ (see Section 2.3.5) in the transport equations for the mass fraction of each chemical species (e.g., Eq. 2.49) that poses severe modelling challenges, due to the fact that $\langle\dot{\omega}_k(\mathbf{Y},\mathbf{x})\rangle \neq \dot{\omega}_k(\langle\mathbf{Y}\rangle,\mathbf{x})$ in RANS or $\overline{\dot{\omega}}_k(\mathbf{Y},\mathbf{x}) \neq \dot{\omega}_k(\overline{\mathbf{Y}},\mathbf{x})$ in LES. A proper combustion model is of paramount importance, especially for the prediction of soot whose formation is closely-associated with the thermochemical state of the system.

There are a large number of combustion models, or closure assumptions, that have been proposed over the past few decades. With the rapid growing complexity of the chemistry, simple method such as the neglect of fluctuations such that $\langle\dot{\omega}_k(\mathbf{Y},\mathbf{x})\rangle = \dot{\omega}_k(\langle\mathbf{Y}\rangle,\mathbf{x})$ is no longer considered accurate or acceptable, and the growing needs for an accurate prediction of pollutants lead to more advanced combustion models that better account for the turbulent-chemistry interactions. Overall, three cases can be identified: slow chemistry (chemical time scales all larger than turbulent flow time scale τ_t); infinitely fast chemistry (all chemical time scales smaller than τ_t); and finite rate chemistry. The ratio of the chemical time scale τ_c and turbulent flow time scale

τ_t defines the dimensionless Damköhler number:

$$\mathrm{Da} = \frac{\tau_t}{\tau_c} \tag{2.72}$$

Consideration of the Damköhler number should be taken into account in closure models for chemical source term, as it is generally used to distinguish different flame structures along with other dimensionless numbers (e.g., Reynolds number). In fact, the structures of the turbulent flames may differ considerably depending on the relative comparison of the chemical scale and turbulent flow scale, which leads to various combustion models. A comprehensive discussion of models can be found in Veynate and Vervisch [107]. As the test case in my work is a turbulent non-premixed flame, I focus on the closure strategies associated with non-premixed combustion in the following discussion.

In non-premixed combustion, fuel and oxidiser are injected separately. The diffusive mixing of the chemical species is the main driving force for the chemical reaction. For hydrocarbon chemistry in turbulent flames, the reaction is typically controlled by the rate of turbulent mixing, described in terms of scalar dissipation rates, as a medium to high Da number is frequently observed. The chemistry can also be important if the chemical time scale τ_c is of comparable magnitude with the flow time scale τ_t, in which case local flame extinction might be observed. The most prevalent models are focused on geometrical or statistical concepts. The former has laid the foundation of the flamelet-based models, in which the transport equations for scalars are simplified to only one-dimension with the direction normal to the flame surface; the latter necessitates the statistical approaches, in which the probability density function (PDF) is used to extract the mean or filtered values and correlations. Some variants of these models are also extended to the modelling of soot particles.

Since combustion occurs at the unresolved scales of the computations, either in RANS or LES, the basic concepts of turbulent combustion modelling are similar for both methods. Furthermore, most RANS combustion models can be adapted to LES.

Among all combustion models, three families of closure approaches that are in frequent use will be introduced briefly:

- Flamelet-based methods
- Conditional moment closure (CMC)
- Transported PDF method

In some combustion models, the solution of the transport equation for the mixture fraction Z is needed. The mixture fraction Z is an overall measure of the mixing between fuel and oxidiser. It is an important parameter that measures the mass fraction of fuel and is related to the mass fraction of elements under certain conditions. As the transport equation for Z contains no source term, Z is a conserved scalar, and combustion models based on the transport of this quantity are also referred to as conserved scalar methods (e.g., flamelet-based method and CMC method). Here, I do not aim for a detailed review. Readers may refer to the work of Veynante and Vervisch [107] and Peters [108] for a comprehensive review of the combustion models in RANS, and the work of Pitsch [109] for the combustion models in LES. A thorough review of the PDF method can be found in the work of Jones [110].

2.5.1 Flamelet-based method

The concept of flamelet was introduced to non-premixed combustion by Peters [111, 112]. The basic assumption includes fast equilibrium chemistry, in which the chemical timescales are short such that reactions are limited in a thin region around stoichiometric mixture whose size may be smaller than the Kolmogorov scale. Consequently, the structure of the thin reaction zone can be treated as laminar, and the diffusive transport can be simplified by assuming the transport only occurs in the direction normal to the surface of the stoichiometric mixture. By doing so, the scalar transport equations are transformed into a system where the mixture fraction Z is the only independent coordinate:

$$\frac{\partial Y_k}{\partial t} = \frac{\chi}{2}\frac{\partial^2 Y_k}{\partial Z^2} + \dot{\omega}_k \tag{2.73}$$

where χ represents the scalar dissipation rate, a fundamental parameter that is needed in most of the combustion models, has been introduced as:

$$\chi = 2\nu_t \left(\nabla Z\right)^2 \tag{2.74}$$

In LES studies, the filtered properties of the flame, for example, can be calculated as:

$$\overline{Y}_k = \int_0^\infty \int_0^1 Y_k(\chi, Z)\overline{f}(\chi, Z; \mathbf{x}, t) dZ d\chi \tag{2.75}$$

where $\overline{f}$ denotes a filtered probability density function (this quantity will be introduced later and elucidated in detail in Chapter 5). Clearly, if $\overline{f}$ is known, one can calculate $\overline{Y}_k$ with the thermochemical relations obtained via Eq. 2.73. Most commonly, a β-PDF is assumed for the filtered PDF $\overline{f}$, which is formulated by the filtered mixture fraction $\overline{Z}$ and the mixture fraction variance $\overline{Z'^2}$ (e.g., see the work of Cook et al. [113]). Since the filtered mixture fraction $\overline{Z}$ can be calculated through the associated transport equation, the filtered reactive scalars can be calculated if $\overline{Z'^2}$ can be obtained from the filtered scalar fields. Commonly, the mixture fraction variance $\overline{Z'^2}$ can be computed by solving a transport equation [114] or by a dynamical model proposed by Pierce and Moin [115], formulated as:

$$\overline{Z'^2} = c_V \Delta^2 \left(\nabla \overline{Z}\right)^2 \tag{2.76}$$

where coefficient c_V is determined dynamically, and the nabla symbol ∇ denotes the vector differential operator.

In steady flamelet models, the transient term in Eq. 2.73 is neglected, and the thermochemical relations further reduce to:

$$\dot{\omega}_k = -\frac{\chi}{2}\frac{\partial^2 Y_k}{\partial Z^2} \tag{2.77}$$

With boundary conditions, the reactive scalar $Y_k(\chi, Z)$ can be characterised by only scalar dissipation rate χ and mixture fraction Z, and thus can be precomputed and tabulated in terms of $\overline{Z}$, $\overline{Z'^2}$ and $\overline{\chi}$ [115]. However, the steady flamelet model will fail to account accurately for the turbulence-chemistry interaction if Da is not large, which is often the case for the prediction of soot.

An alternative model designed specifically for LES is the flamelet/progress variable model (FPV) by Pierce and Moin [116], in which the steady-state flamelet library is characterised by the mixture fraction and a reaction progress variable. To retrieve the variables of the table, transport equation for the progress variable is solved, in which the closure can be achieved by using the flamelet library and a presumed joint filtered PDF of mixture fraction and reaction progress variable. Further model variants include radiative heat losses [117] (referred to as RFPV) and have been employed in several studies targeting soot formation (e.g., Refs. [118], [119] and [29])

2.5.2 Conditional moment closure method

The CMC model was originally proposed in the context of RANS by Klimenko [120] and Bilger [121], based on the observation that the conditional fluctuations of reactive scalars are considerably smaller than the unconditional fluctuations in the scatter plot, e.g., in Fig. 2.4.

In CMC method, transport equations are derived for mixture fraction-conditioned averages of the reactive scalar $\langle Y_k|Z\rangle$. In these equations, the unclosed source terms $\langle \dot{\omega}_k(\mathbf{Y})|Z\rangle$ can be approximated as $\dot{\omega}_k(\langle \mathbf{Y}|Z\rangle)$ (also known as first-order closure), based on the assumption that the fluctuations about the conditional averages are small and the conditional covariance can be neglected [122]. Subsequently, given a closure for $\langle Y_k|Z\rangle$ and the mixture fraction PDF, the unconditional Reynolds-averaged scalar $\langle Y_k\rangle$ or chemical source term $\langle \dot{\omega}_k\rangle$ can be obtained through an equation analogous to Eq. 2.75. A presumed PDF is often used, and it can be associated with the mean and variance of the mixture fraction that can be obtained from the flow field solution. The

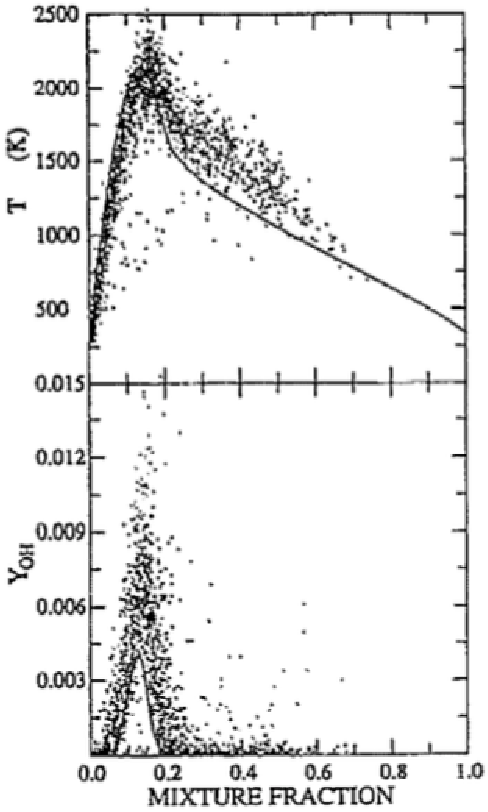

Figure 2.4: Scatter plots of all data and conditional averages conditional on the mixture fracture for the temperature and OH mass fraction in a piloted non-premixed flame of methanol at certain positions. The illustration is adapted from Fig. 5 in [121].

mixture fraction conditioning significantly simplifies the modelling of the chemical source term, but makes it hard to solve the transport equation for $\langle Y_k|Z\rangle$. Several models are proposed for the closure of the transport equation. A detailed summary in the context of RANS can be found in the work by Klimenko and Bilger [122], and the extension of CMC to LES can be found in the work of Navarro-Martinez et al. [123].

Both the flamelet-based method and the CMC method require the solution of the transport equation for a conserved scalar (e.g., mixture fraction in non-premixed flame). These methods are therefore referred to as conserved scalar methods and have many similarities. Compared to the prediction of unconditional expectations $\langle Y_k\rangle$, the CMC model, in general, provides much more detailed characteristics of the reactive scalar fields and has been used in a large number of studies with success, including the application in soot prediction [124–127]. In the study regarding soot formation, with the increasingly complex soot kinetics, an accurate prediction of the radical species (e.g., OH, H) that often peak in very thin layers on the small scales becomes critical, and the chemical time scales associated with PAH species are generally slow. Such feature of the problems may pose a challenge to both CMC and flamelet-based methods. In the next section, I shall introduce the next step, in which the shape of the joint scalar PDF is directly solved from its transport equation. This family of the method is commonly referred to as the transported PDF method.

2.5.3 The transported PDF method

The closure achieved by flamelet-based methods and CMC methods requires a priori assumptions concerning the shape of the PDF, which is commonly associated with the mean and variance of the mixture fraction in non-premixed flames. However, such a treatment may be inappropriate when chemical reaction timescale is relatively large, as it is in the case of soot formation. To reproduce finite rate effects, a multi-dimensional PDF is needed. In the transported PDF method, the joint PDF for a set of reactive scalars is solved from its own transport equation. In the present section, I discuss the main features of the method, leaving the details of the theory and equations for Chapter 5.

The joint PDF for a set of reactive scalars, $f(\mathbf{\Psi};\mathbf{x},t)$, contains all one-point, one-time information of the reactive scalar fields $\mathbf{\Phi}(\mathbf{x},t)$. To derive its evolution equation, one relies on the use of the conservation equations and the concept of a fine-grained density function $g(\mathbf{\Psi};\mathbf{x},t)$, pioneered by Lundgren [128] or Pope [103, 129]. $g(\mathbf{\Psi};\mathbf{x},t)$ is defined such that $g(\mathbf{\Psi};\mathbf{x},t)d\mathbf{\Psi}$ is the probability that $\psi_\alpha \leq \phi_\alpha(\mathbf{x},t) \leq \psi_\alpha + d\psi_\alpha$ for all $\alpha = 1, \ldots, N$ at position $\mathbf{x}$ and time t. Note that $\mathbf{\Psi}$ denotes $'$position$'$ in the PDF sample space of the random variable $\mathbf{\Phi}(\mathbf{x},t)$. Obviously, $g(\mathbf{\Psi};\mathbf{x},t)$ is a multi-dimensional quantity which represents the PDF for a single realisation of a turbulent flow. If $\psi_\alpha \leq \phi_\alpha(\mathbf{x},t) \leq \psi_\alpha + d\psi_\alpha$ for all $\alpha = 1, \ldots, N$ is not satisfied for all α, then $g(\mathbf{\Psi};\mathbf{x},t)d\mathbf{\Psi} = 0$, otherwise $g(\mathbf{\Psi};\mathbf{x},t)d\mathbf{\Psi} = 1$. Consequently, the fine-grained density function can be formulated via Dirac delta function:

$$g(\mathbf{\Psi};\mathbf{x},t) = \prod_{\alpha=1}^{N} \delta(\psi_\alpha - \phi_\alpha(\mathbf{x},t)) = \delta(\mathbf{\Psi} - \mathbf{\Phi}(\mathbf{x},t)) \tag{2.78}$$

And its relation to the joint scalar PDF $f(\mathbf{\Psi};\mathbf{x},t)$ follows (see Pope [129]):

$$f(\mathbf{\Psi};\mathbf{x},t) = E[g(\mathbf{\Psi};\mathbf{x},t)] \tag{2.79}$$

Note that symbol $E[\cdot]$ denotes the mean as a mathematical expectation. This definition of the mean is generally applicable to all the flows and is commonly estimated by the ensemble average in practical use. Other possible choices include the time average in RANS $\langle\cdot\rangle$ and the spatial filtering in LES $\bar{\cdot}$. A good source of discussion regarding the difference and connections between these measures can be found in Section 2.6 of [129]. In practice, $f(\mathbf{\Psi};\mathbf{x},t)$ represents an ensemble of realisations, such that its integral over a certain region of its sample space indicates the likelihood of occurrence for an event.

The details of the derivation for the transport equation for $f(\mathbf{\Psi};\mathbf{x},t)$ in either

RANS or LES can be found in several works including O'Brien [130], Pope [103, 129] or Colucci et al. [131]. Regardless of the derivation method, the final form of the transport equation for the Favre-weighed scalar PDF in LES is written as:

$$
\begin{aligned}
\overline{\rho}\frac{\partial \widetilde{f}(\boldsymbol{\Psi})}{\partial t} + \overline{\rho}\widetilde{u}_j\frac{\partial \widetilde{f}(\boldsymbol{\Psi})}{\partial x_j} + \underbrace{\frac{\partial}{\partial x_j}\left(\overline{\rho u_j f(\boldsymbol{\Psi})} - \overline{\rho}\widetilde{u}_j\widetilde{f}(\boldsymbol{\Psi})\right)}_{\text{I. turbulent convection in physical space}} &= \\
-\underbrace{\sum_{\alpha=1}^{N}\frac{\partial}{\partial \psi_\alpha}\left(\overline{\rho}\dot{\omega}_\alpha(\boldsymbol{\Psi})\widetilde{f}(\boldsymbol{\Psi})\right)}_{\text{II. chemical reaction in composition space}} & \\
\underbrace{-\sum_{\alpha=1}^{N}\frac{\partial}{\partial \psi_\alpha}\left(\overline{\rho}\widetilde{f}(\boldsymbol{\Psi})\overline{\left(\frac{1}{\rho}\frac{\partial}{\partial x_j}\left(\Gamma_\phi\frac{\partial \phi_\alpha}{\partial x_j}\right)\middle|\boldsymbol{\Psi}\right)}\right)}_{\text{III. conditional diffusion in composition space}} &
\end{aligned}
\tag{2.80}
$$

where the spatial and temporal dependencies of the PDF is omitted for clarity. A detailed derivation will be given later in Section 5.1.2.

Inspection of Eq. 2.80 shows that the notable chemical source term II is in an exact and closed form, which is known in terms of $\boldsymbol{\Psi}$ and $\widetilde{f}(\boldsymbol{\Psi})$. This feature reveals the major benefit of adopting the PDF method in reacting flows. The chemistry involving finite-rate kinetics can be incorporated without an assumed flame structure to characterise the thermochemical state. And the concept can be easily extended to incorporate the turbulent-chemistry-particle interaction, which will be explained later in the next section and Chapter 5.

Term I of Eq. 2.80 represents the turbulent convection at SGS level. Its closure can be made by a simple gradient diffusion hypothesis directly analogous to the Smagorinsky model in the LES scalar transport equation (see ...todo):

$$
\overline{\rho u_j f(\boldsymbol{\Psi})} - \overline{\rho}\widetilde{u}_j\widetilde{f}(\boldsymbol{\Psi}) = -\overline{\rho}\Gamma_{sgs}\frac{\partial \widetilde{f}(\boldsymbol{\Psi})}{\partial x_j}
\tag{2.81}
$$

Although in the joint velocity-composition PDF the turbulent transport term appears in closed form, the introduction of the velocity brings further unknown terms and extra independent variables to the equation. Note that the quantity u_j in Eq 2.80 is unknown, but conventionally supplied through the solution of the LES filtered Navier-Stokes equation using a turbulent model.

Term III of Eq. 2.80 represents the conditional diffusion in composition space, which is also referred to as the micromixing. It appears in unclosed form as one-point one-time joint scalar PDF does not contain information regarding spatial gradient of scalars, and stems directly from the molecular diffusion term in the instantaneous species conservation equation. As molecular diffusion is essential to the reaction process, an accurate description for the diffusion term is vital to determining the evolution of the joint scalar PDF. In general, a micromixing model should follow several principles, which slightly differ depending on the average approach. Discussion regarding micromixing in RANS can be found in Fox [132]. Here, I list the most desirable properties of an ideal micromixing model in the LES context, see, e.g. McDermott and Pope [133]: a) the model accounts for the spatial transport of the filtered PDF and consequently all moments of the filtered PDF, b) the model captures the decay of the SGS covariance, and this term vanishes in the DNS limit, and c) the model should preserve the realisability principle (e.g., guarantee that species mass fractions are positive and sum to unity) and scalars boundedness (e.g., the mass fraction stays strictly between $[0,1]$). The most basic mixing model is the linear mean square estimation (LMSE), also known as interaction by exchange with the mean (IEM) [134]. In this work, I adopt the model proposed by McDermott and Pope [133], in which the concept of IEM is combined with a spatial transport of the mean, written as:

$$\overline{\left(\frac{1}{\rho}\frac{\partial}{\partial x_j}\left(\Gamma_\phi \frac{\partial \phi_\alpha}{\partial x_j}\right)\middle|\boldsymbol{\Psi}\right)} = \frac{1}{\overline{\rho}}\frac{\partial}{\partial x_j}\left(\Gamma_{sgs}\frac{\partial \widetilde{\phi}_\alpha}{\partial x_j}\right) + \kappa\left(\widetilde{\phi}_\alpha - \phi_\alpha\right) \tag{2.82}$$

where the micromixing frequency κ represents the reversed SGS mixing time scale common to all scalars, formulated as:

$$\kappa = \frac{C_\kappa}{2}\frac{\Gamma_{sgs}}{\Delta^2} \tag{2.83}$$

where C_κ represents the SGS micromixing constant. In RANS applications to inert flows, a constant of 2 predicts correctly the scalar dissipation rate for a passive scalar in equilibrium conditions. Albeit the fact that this value is not universal, a constant 2 may be adequate in many situations, see e.g. [11, 106]. Finally, substituting Eqs. 2.81 and 2.82 into Eq. 2.80, the transport equation for the joint scalar PDF is in closed form.

Clearly, the PDF transport equation is high dimensional, which means that standard numerical solution algorithms such as finite-difference or finite-volume methods are computationally intractable [135]. The alternative to a discretisation of the transported PDF is to use Monte-Carlo (MC) method, in which computational cost increases only linearly with the number of independent variables. The MC methods in use can be categorised as either Eulerian or Lagrangian [132]. In any method, the fundamental concept is to construct a system of stochastic differential equations whose evolution pattern is statistically equivalent to the evolution of the transported PDF. In other words, the MC method estimates the expectations associated with the joint PDF. The stochastic field method [136–138] used in my study will be elucidated in Section 5.3. More details can also be found in Ref. [110]

Although, as pointed out in Ref. [110], the closure for the chemical term is the consequence of the mathematical manipulations employed to derive such a transport equation, the unique nature of the PDF method in dealing with the non-linear terms facilitates its extension to incorporate the aerosol dynamics. It can also be a powerful tool in dealing with turbulence-chemistry-soot interaction, which will be discussed in the next section.

2.6 Turbulence-chemistry-soot interaction

The coupling of the soot model with turbulent reacting flow brings out a further level of complexity, as various non-linear interactions between turbulent flow, chemistry and soot model must be properly addressed. As soot kinetics depend on the thermochemical state of the system, various methods for predicting soot in turbulent flame have been developed considering several aspects: a) the combustion model accounting for the turbulence-chemistry interactions, b) the method accounting for aerosol dynamics (e.g., moment-based method or discretised PBE), and c) the comprehensiveness of the soot kinetics. From the model validation perspective, measurements in sooting flames often do not provide joint data, posing a significant challenging model validation issue [119]. Apart from that, recent advances in soot studies have shown that polycyclic aromatic hydrocarbons (PAHs) are of paramount importance in the process of soot formation [12]. In turbulent flow, PAH species related to soot precursors are highly sensitive to the turbulent mixing and scalar dissipation rate [139, 140], while their chemical reaction rates are relatively slow and do not respond promptly to the mixing phenomena [141]. Consequently, in order to formulate a comprehensive model, one must properly address the complex nature of interaction between turbulence, chemistry and particle formation [23, 59, 142].

From the mathematical formulation, the interactions to be addressed appear as unclosed terms in the processed governing equations, either by averaging (in RANS) or filtering (in LES). As pointed out by Rigopoulos [9], the averaging of the discretised PBE gives rise to three kinds of unknown terms:

1. Correlation between reactive scalars
2. Correlation between reactive scalars and number density
3. Correlation between number density

The correlations of type 1 are due to nucleation and surface reaction, whose reaction rates are normally non-linear as shown in Section 2.1. They are accounted for depending on the turbulence-chemistry model adopted (similar to the chemical reaction source term). The correlations of type 2 and 3 are unique to turbulent flames with aerosols. The former arise due to the growth term Gn (e.g., see Eq. 2.40), while the latter arise because of the product of number density in coagulation terms. Regrouping the terms associated with aerosol dynamics in Eq. 2.40 into a source term, the transport equation for the PBE takes the following form:

$$\frac{\partial \phi_n}{\partial t} + \frac{\partial (u_j \phi_n)}{\partial x_j} = \frac{\partial}{\partial x_j}\left(D_n \frac{\partial \phi_n}{\partial x_j}\right) + \dot{\omega}_n \tag{2.84}$$

where D_n indicates the diffusion coefficient associated with the particle scalars ϕ_n of interest, which can be either the discretised PBE section or the moments of the PBE, and the source term $\dot{\omega}_n$ encompasses all the terms associated with aerosol dynamics (nucleation, surface reaction, coagulation and possibly other terms of interest). As can be seen, the closure challenges here have close similarities with the closure challenges of the chemical source term.

Substantial efforts have been devoted to the numerical prediction of soot formation in turbulent combustion [23]. RANS-based models have been the focus of sooting flame studies until the past decade, and a review of these works can be found in Ref. [23]. While RANS-based models have a low computational cost, they rely heavily on modelling choices in order to account for the effect of turbulent fluctuations and for the interactions between turbulence, chemistry and soot, as the effects of fluctuations and non-linear interactions at all scales must be accounted for by the model. DNS provides detailed, complete and spatially and temporally fully resolved data that is invaluable for model development, but there have been only a few such studies of sooting flames dealing with simplified cases with moderate Reynolds numbers due to the high CPU requirements [27,119,139–141,143–145]. In LES, only the more energetic flow structures are simulated, and therefore accurate predictions of flame dynamics and mixing patterns can be accomplished at an affordable computational cost. LES-based studies of sooting flames and combustors have been appearing with increasing frequency, especially during the last decade (e.g. [11, 27–29, 118, 119, 124, 146–157]). The applications of LES to soot differ in three main aspects, namely the description of the turbulent-chemistry/soot formation interaction and subsequent closure strategy, the level of detail in soot kinetics and the aerosol dynamics formulation. With respect to the last of these, the majority of studies have employed moment methods; only recently have sectional methods started to be applied [11,29], which is one of the main aspects of this thesis.

The first (to my knowledge) LES of a turbulent non-premixed flame was conducted by El-Asrag and Menon [147], where a moment method for soot was included under the framework of the Linear Eddy Model (LEM) for the subfilter process. Later, Mueller and Pitsch [118] combined PAH inception kinetics and a moment-based soot model with an extended Flamelet/Progress Variable (FPV) model that accounts for radiative heat loss (RFPV) [117], and applied their approach to the Delft flame III [158]. The small-scale interaction between turbulence and soot was addressed by a presumed PDF method [148]. Specifically, the joint PDF was split into the PDF of the thermochemical variables and a conditional PDF of the soot scalars on the thermochemical variables, based on the assumption that the characteristic timescales related to soot precursors PAH and soot are much longer than that of the main heat-releasing thermochemical variables. Subsequently, the PDF of the thermochemical variables was modelled by a beta distribution for the mixture fraction and delta functions for variables related to progress variable and heat loss parameter, while a double delta function was used to model the soot-related PDF. To accommodate the slow chemistry of PAH, the authors added a separate transport equation for a "lumped" PAH mass fraction. In a subsequent study, Xuan and Blanquart [27] solved the filtered transport equations for benzene (C_6H_6) and naphthalene ($C_{10}H_8$) as an alternative approach to the lumped PAH evolution equation in [118]. The associated closure for the filtered source terms was achieved by a PAH relaxation model. As the soot evolution in these studies was described by moment-based method, no information on the soot PSD was predicted. A recent study by Rodrigues et al. [29] applied a soot sectional method within the scope of LES-presumed PDF model of Mueller and Pitsch [118], in which some qualitative trends for soot measurements were reproduced. Donde et al. [149] utilised the concept of the transported PDF approach based on the IEM micromixing model to account for the turbulence-chemistry/soot interaction. The associated high-dimensional PDF was solved via a Lagrangian Monte-Carlo method. Similarly, the gas-phase turbulent combustion was described via a flamelet-based model. Another mixture fraction-based method that has been employed in soot modelling is the LES-CMC approach. In an early study, Navarro-Martinez and Rigopoulos [124] incorporated a two-equation semi-empirical soot model of Leung et al. [30] into an LES-CMC framework to model a turbulent non-premixed flame. Recently, the LES-CMC approach and the two-equation soot model were employed to study soot formation in a single sector model combustor by Giusti et al. [154]. Both studies assumed a presumed β-function to compute unconditional filtered values.

Although progress has been made in the aforementioned studies regarding the prediction of soot formation in turbulent combustion, several open questions remain. Firstly, the steady flamelet model ignores the unsteady term, which impacts the species significantly with slow chemistry. As indicated in the DNS study of Bisetti et al. [139], the unsteady effects must be addressed for slowly adjusting PAH species such as naphthalene. The customary approach to remedy the issue is to solve extra spatially filtered transport equations for PAHs. This closure strategy, however, would bring a new source of uncertainty into the system. Furthermore, the LES-presumed PDF method decouples the correlation between soot and gas-phase chemistry based on the assumption of the timescale separation. This assumption, however, could potentially be violated if the timescale of the processes associated with soot-chemistry interaction (i.e. soot oxidation) is comparable with the timescale of gas-phase chemistry. The performance of the LES-CMC approach for complex chemistry with more advanced soot models needs further investigations, especially in turbulent flames which experience extinction or reignition. When moment methods are employed for the solution of the PBE, the resulting moment equations are unclosed and modelling assumptions are required to obtain closure. Sectional methods, on the other hand, require accurate methods to avoid issues with conservation of moments and numerical diffusion and have been largely unexplored. As of current, quantitative agreement between simulations and experiments cannot be accomplished for soot in turbulent flows [23].

Alternatively, the turbulence-chemistry-soot interaction can be accounted for by an evolution equation for the one-point, one-time joint probability density function associated with reactive scalars and the particle number density, named as PBE-PDF approach. This concept was proposed by Rigopoulos [9], in the context of RANS, to account for the unclosed terms resulting from three sources: functions of reactive scalars, such as nucleation, terms involving correlations of scalars and number density, such as surface growth, and terms involving products of number densities, such as aggregation and condensation. This approach overcomes the closure problem and establishes a link between the transport equations for reactive scalars and discretised PBE scalars in turbulent flow (see Ref. [23] for further discussion). Later on, the idea was revisited by Sewerin and Rigopoulos [10] who formulated, within the scope of LES, a joint scalar-number density PDF transport equation in which the physical processes related to chemical reactions and soot formation are naturally in closed form, and referred as LES-PBE-PDF approach. More recently, Sewerin and Rigopoulos [11] generalised this approach to polydispersed particle formation in variable density flows of gases at low Mach number. The LES-PBE-PDF approach allows for introducing the PBE to LES without closure assumptions regarding the turbulence-soot interaction. The RANS PBE-PDF was first applied to precipitation of particles in liquid turbulent reacting flows [159,160] and to aerosol condensation in a turbulent jet [161], while the LES-PBE-PDF was applied to aerosol condensation in a turbulent mixing layer [10] and soot formation in a turbulent jet flame [11]. Despite the encouraging progress, the kinetic models employed was relatively simple, and only nucleation and surface reactions were considered, leaving the full potential of the LES-PBE-PDF approach unexplored. These matters facilitate the second objective of my thesis.

Chapter 3

Population balance modelling of soot formation in laminar flames

The main objective of this chapter is to demonstrate how to extend the conservative finite volume method for the solution of the PBE proposed by Liu and Rigopoulos [7], originally formulated for a single PBE (CFV-1PBE), to a two-PBE formulation (CFV-2PBE) that allows for a more accurate modelling of primary particle surface growth and oxidation and furthermore involves a timescale for the fusing of primary particles.

As the research challenges behind this development was presented in Section 2.2.2, here I review the one-PBE model of aggregation and the conservative finite volume method, addressing their inherent defects, then introducing the two-PBE model of coalescence and aggregation and its discretised form, in which the coupling of the two-PBE model with CFD and associated numerical aspects are addressed. Subsequently, numerical validations for the CFV-2PBE are presented. In particular, the spatial transport for primary particles is shown to be consistent to the spatial transport for aggregates, and the extended method is shown to reproduce the self-preserving distributions correctly in the two asymptotic cases of coagulation of spherical particles and aggregation to fractal aggregates.

3.1 The one-PBE model of aggregation

In this section, I summarise the concepts underlying the CFV-1PBE method. As the method has been described in detail in [7], the emphasis here is on explaining its deficiencies when it comes to the modelling of fractal aggregates.

The CFV-1PBE method is a finite volume method for the solution of the one-dimensional PBE with nucleation, condensation, growth (or oxidation) and aggregation. For a spatially homogeneous system, the equation is shown below (the coupling with flow will be discussed later):

$$\begin{aligned}\frac{\partial n(v,t)}{\partial t} + \frac{\partial (G(v,\mathbf{Y})n(v,t))}{\partial v} &= B\delta(v-v_0) + \dot{C}(\mathbf{Y},v) \\ &+ \frac{1}{2}\int_0^v \beta(w,v-w)n(w,t)n(v-w,t)dw - n(v,t)\int_0^\infty \beta(v,w)n(w,t)dw \quad (3.1)\end{aligned}$$

where B, G, and $\dot{C}$ are the nucleation, growth and condensation rates, respectively, and $\beta(v,w)$ is the aggregation kernel (the models for these processes will be discussed in Section 4.1). The objectives of this method are to attain: a) accurate prediction of the distribution with a small number of sections, b) conservation of the first moment (or any other single moment) in aggregation, c) applicability to any non-uniform grid (even an adaptive one), and d) speed and robustness for coupling with CFD. The method is based on the framework of finite volume methods, which are endowed with the conservation property by balancing the inflow and outflow fluxes at a computational cell. In the PBE, however, due to the presence of the integral terms, the fluxes originate in various parts of the domain, and furthermore the convolution-resembling aggregation birth term prevents their identification in order to satisfy the conservation property. In this method, a transformation is used to decompose the birth term into its constituent fluxes, and a map is constructed to record them. An important part of the method is the algorithm for constructing this map in an arbitrary non-uniform grid. The aggregation birth and death terms are then calculated via these fluxes, and the conservation of mass is ensured without introducing correction terms. The map is constructed in the beginning and accessed during the simulation, and the method is thus computationally efficient and easy to couple with CFD. Test cases, including analytical solutions and a co-flow laminar flame [7], have shown that the method produces very accurate solutions that conserve the first moment, even on coarse grids.

When it comes to the modelling of fractal aggregates, the previous applications of the CFV-1PBE method [1,7] employed the first of the three approaches mentioned in Section 2.2.2, which is to impose a cut-off size between spherical particles and fractal aggregates and assume that aggregates are composed of a number of equally sized primary particles. In this approach, the only modification needed in Eq. 3.1 is to formulate the aggregation kernel in terms of the aggregate collision diameter, d_g, which is related to the volume of the aggregate v via the following equation [57]:

$$\frac{v}{v_p} = k_f \left(\frac{d_g(v)}{d_p} \right)^{D_f} \tag{3.2}$$

where v_p and d_p are the volume and diameter of the primary particles, respectively, k_f is the fractal prefactor and D_f is the fractal dimension. The latter has the value 3 for spherical particles and 1 for linear ones, with fractal aggregates having values in between. A constant fractal dimension is usually assumed in population balance models (see e.g., [8,162,163]), based on observations from experiments (see e.g., [67,69, 164,165]) that the fractal dimension of aggregates exhibits values around 1.8. Spherical particles can exhibit a range of diameters up to the cut-off size, while all primary particles within aggregates are assumed to have a diameter d_p equal to the cut-off size. The implementation of aggregates in the context of the CFV-1PBE method is thus straightforward, as no modifications in the overall structure of the PBE are involved. As mention in Section 2.2.2, however, this approach has two significant limitations: it employs an artificial and non-physical parameter, the cut-off size, and it results in an inconsistent calculation of oxidation and growth, due to the surface area not being consistent with the volumetric growth rate. These limitations originate in the fact that the one-dimensional PBE is inherently inadequate to provide an accurate description of aggregates due to the lack of morphological parameters in the formulation.

3.2 The two-PBE model of aggregation

To provide a consistent and physical account of aggregation, the population balance model must address the two limitations mentioned at the end of the last section. The introduction of an additional variable, rather than a parameter such as the cut-off point, is essential to account for aggregate morphology. As discussed in Section 2.2.2, both surface area and the average number of primary particles per aggregate have been employed as the second variable for describing aggregate morphology, and the latter approach is employed in this work.

A schematic illustration of the concepts underlying the one-PBE and two-PBE models is shown in Fig. 3.1. Note that it is still necessary to distinguish between the coalescence of incipient particles, which is virtually instantaneous, and the gradual fusing of primary particles within aggregates. While a critical diameter is employed in both models, its impact in the one-PBE model is far greater, as all primary particles within aggregates are assumed to have this diameter, while in the two-PBE model it just distinguishes the incipient particles from the rest. If the same critical diameter is employed in both models and no finite-rate fusing is introduced in the two-PBE model, both models would yield the same self-preserving distribution (as shown later in Section 3.4.2, Fig. 3.5). The determination of this diameter will be addressed in Section 4.1.5.

The first equation of the model is the PBE for the number density of soot particles, whether primary ones or aggregates, with the addition of transport in physical space:

$$\begin{aligned}\frac{\partial n}{\partial t} + \frac{\partial (G(v,\mathbf{Y})n)}{\partial v} + \frac{\partial (u_j n)}{\partial x_j} &= \frac{\partial}{\partial x_j}\left(D_p \frac{\partial n}{\partial x_j}\right) + B(\mathbf{Y})\delta(v-v_0) \\ &+ \dot{C}(v,\mathbf{Y}) + \frac{1}{2}\int_0^v \beta(w,v-w)n(w)n(v-w)dw - \int_0^\infty \beta(v,w)n(v)n(w)dw \quad (3.3)\end{aligned}$$

where D_p denotes the particle diffusion coefficient, which is size-dependent [57]. In

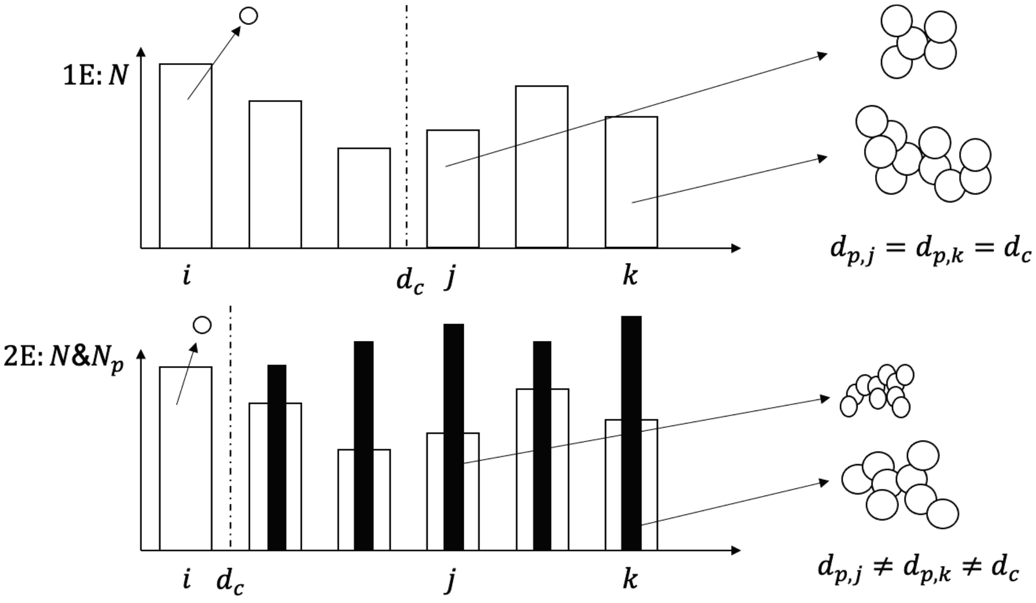

Figure 3.1: A schematic illustration of the concepts involved in the one-PBE and two-PBE models. The white histogram represents the number of aggregates, while the black histogram represents the number of primary particles.

this and the following equations, the dependence on v, $\mathbf{x}$ and t will be omitted except when necessary. This equation is coupled with the equations of fluid dynamics and species transport equations via the velocity field, u_i, and the concentrations of chemical species, Y_α. Two issues must be addressed when fractal aggregates are present: the aggregation kernel must be formulated in terms of their collision diameter, and the calculation of the surface area, which appears in the growth function, must take into account the structure of the aggregates. The first issue is straightforward, as the aggregate collision diameter can be related to the aggregate volume via Eq. 3.2; it must be noted that, unlike the case of the one-PBE model, the average primary particle volume does not remain constant here. The second issue is the source of the inconsistent calculation of growth in the one-PBE model and will be addressed via the second PBE, in the context of which I will introduce the finite-rate fusing of primary particles.

The second equation is the PBE for the number density of primary particles. I denote by $n_{av}(v,t)$ the average number of primary particles per aggregate having volume v at time t:

$$n_{av}(v,t) = \frac{n_p(v,t)}{n(v,t)} \tag{3.4}$$

where $n_p(v,t)$ represents the number density of primary particles that form aggregates of volume v (as before, in the following the dependence on v and t will be omitted for brevity). According to Eq. 3.2, this can be related to the collision diameter d_g as follows:

$$n_{av} = k_f \left(\frac{d_g}{d_p}\right)^{D_f} \tag{3.5}$$

The gradual fusing of primary particles within an aggregate results in a change in surface area, a, according to the following equation formulated by Koch and Friedlander [88]:

$$\frac{da}{dt} = -\frac{1}{\tau_s}(a - a_s) \tag{3.6}$$

where τ_s denotes the characteristic timescale. Eq. 3.6 expresses the fact that the driving force for fusing is the deviation of the surface area of an aggregate from that of a sphere with equal volume, a_s. It is now possible to obtain an equation for the rate of change of the primary particles, as shown in [94]. Considering an aggregate composed of n_p spherical primary particles of radius r, its volume v and surface area a have the following expressions:

$$v = n_p v_p = \frac{4\pi}{3} n_p r^3 \tag{3.7}$$

$$a = n_p a_p = 4\pi n_p r^2 \tag{3.8}$$

where a_p is the surface area of a primary particle. Using Eqs. 3.7 and 3.8, the surface area a can be expressed in terms of v and n_p as follows:

$$a = \left(36\pi v^2 n_p\right)^{1/3} \tag{3.9}$$

As the volume of the aggregate does not change during the fusing of primary particles, Eq. 3.9 can be differentiated to obtain:

$$\frac{da}{dt} = \left(\frac{\frac{4}{3}\pi v^2}{n_p^2}\right)^{1/3} \frac{dn_p}{dt} \tag{3.10}$$

Similarly, the surface area of the sphere a_s can be expressed in terms of v as:

$$a_s = \left(36 v^2 \pi\right)^{1/3} \tag{3.11}$$

At this point, by substituting Eq. 3.9 and Eq. 3.11 into Eq. 3.6 and replacing da/dt with the help of Eq. 3.10, the following expression can be derived:

$$\frac{dn_p}{dt} = -\frac{3}{\tau_s}\left(n_p - n_p^{2/3}\right) \tag{3.12}$$

Finally, the rate of change of the average number of primary particles per aggregate due to fusing can be obtained as follows [94]:

$$\left.\frac{dn_{av}}{dt}\right|_{sint} = -\frac{3}{\tau_s}\left(n_{av} - n_{av}^{2/3}\right) \tag{3.13}$$

The derivation of the aggregation term for primary particles is based on the following consideration: the increase in the number of primary particles of size v due to the collision must account for the primary particles originating from both particle $v - w$ and w, and the aggregation terms for n_p can thus be written in terms of n and n_{av}. The PBE for the primary particles, including transport terms, can therefore be written as follows:

$$\begin{aligned}
\frac{\partial n_p}{\partial t} + \frac{\partial\left(G(v,\mathbf{Y})n_p\right)}{\partial v} + \frac{\partial(u_j n_p)}{\partial x_j} &= \frac{\partial}{\partial x_j}\left(n_{av} D_p \frac{\partial n}{\partial x_j}\right) \\
&+ B(\mathbf{Y})\delta(v - v_0) - \frac{3}{\tau_s}\left[\frac{n_p}{n} - \left(\frac{n_p}{n}\right)^{2/3}\right] n + \dot{C}_p(v,\mathbf{Y}) \\
&+ \frac{1}{2}\int_0^v \beta(w, v-w) n(w) n(v-w)(n_{av}(v-w) + n_{av}(w)) dw \\
&- \int_0^\infty \beta(v,w) n(w) n(v) n_{av}(v) dw
\end{aligned} \tag{3.14}$$

All the terms associated with primary particles are denoted with the subscript p, except for the diffusion coefficient D_p, which indicates diffusion of corresponding aggregates associated with primary particles. As mentioned, the coalescence of incipient particles is assumed to be instantaneous, hence Eq. 3.14 is invoked only for sections where the particle diameter exceeds the critical diameter.

3.3 The conservative finite volume method for the two-PBE model

In this section, I will show how the CFV-1PBE method can be extended to the two-PBE model (CFV-2PBE). The number density distribution of particles in the volume section (v_{i-1}, v_i) (referred to as section i in the following) is assumed to be uniform and will be written as N_i for aggregates and $N_{p,i}$ for primary particles (note that the meaning of N_i here is different from the number concentration used for discrete PBE in Section 2.2), while the corresponding average number of primary particles per aggregate will be denoted as $n_{av,i}$.

3.3.1 Nucleation and growth

The finite volume discretisation for the nucleation and growth terms of the aggregates can be written as:

$$\left.\frac{dN_i}{dt}\right|_{nuc,gr} = -\frac{1}{\Delta v_i}\left[nG(v,\mathbf{Y})\right]\Big|_{v_{i-1}}^{v_i} + \frac{1}{\Delta v_i}\int_{v_{i-1}}^{v_i} B_i dv_i \tag{3.15}$$

where the nucleation rate, B_i, is non-zero only over the interval including the nuclei volume v_0. For primary particles, the growth term is formulated as follows:

$$\left.\frac{dN_{p,i}}{dt}\right|_{gr} = -\frac{1}{\Delta v_i}\left[n_pG(v,\mathbf{Y})\right]\Big|_{v_{i-1}}^{v_i} \tag{3.16}$$

No nucleation term is included in the equation for $N_{p,i}$, as this PBE is solved only for particles greater than the critical diameter where coalescence is not instantaneous.

The treatment of the growth term in the two-PBE model must be guided by the principle that the growth of primary particles is related to that of aggregates, and thus an identical growth rate G must be employed. For example, when an aggregate enters section $i+1$ from section i, all of the primary particles within that aggregate will enter section $i+1$. Assuming that an aggregate experiences only surface growth, the aggregate volume increases while the number of primary particles maintains the same, leading to an increased primary particle size. Subsequently, the model provides a consistent description for the growth, compared to the one-PBE model that was based on the assumption of constant primary particle size. Therefore, the finite volume discretisation for the growth term is identical in both PBEs, a fact that circumvents the need for calculating two growth terms, and it will be shown below for the aggregates only. I employ a total variation diminishing (TVD) scheme [166], employed for the PBE by Qamar et al. [167, 168] for an arbitrary non-uniform grid:

$$(nG(v,\mathbf{Y}))_{v_i} = G(v,\mathbf{Y})\left[N_{u(v_i)} + \frac{1}{2}\phi(r_i)(N_{u(v_i)} - N_{uu(v_i)})\right] \tag{3.17}$$

where the $N_{u(v_i)}$ and $N_{uu(v_i)}$ are the number densities of the two cells upstream of node v_i, and $\phi(r_i)$ is the flux limiter at node v_i [169]:

$$\phi(r_i) = \max\left[0, \min\left[2r_i, \min\left(\frac{1}{3}\frac{v_i - v_{i-1}}{v_{m,i} - v_{m,i-1}} + \frac{2r_i}{3}\frac{v_i - v_{i-1}}{v_{m,i+1} - v_{m,i}}, 2\right)\right]\right] \tag{3.18}$$

where $v_{m,i} = 0.5(v_i + v_{i-1})$ and r_i is the upwind ratio of two consecutive number density gradients [166]:

$$r_i = \frac{N_{i+1} - N_i + \epsilon}{N_i - N_{i-1} + \epsilon} \tag{3.19}$$

and ϵ is a small number employed to avoid division by zero.

The growth rate depends on the surface area of soot aggregates. In my study, the following expression is used for the surface area [69]:

$$a_i = a_{(C_{ov}=0),i}\left[1 - \phi C_{ov}\left(1 - \frac{1}{n_{av,i}}\right)\right] \tag{3.20}$$

where $\phi = 1.3$ denotes the averaged number of contacts per primary particles, C_{ov} is the overlap parameter for which the value 0.15 is used [69], and $a_{(C_{ov}=0)}$ denotes the surface area of the aggregates when there is no overlap between primary particles (point contact).

3.3.2 Aggregation

In the CFV-1PBE method, the discretisation of the aggregation terms can be written as follows:

$$\begin{aligned} \left.\frac{dN_i}{dt}\right|_{agg} &= \frac{1}{\Delta v_i}\int_{v_{i-1}}^{v_i}\int_{v_0}^{\frac{v}{2}} \beta(w, v-w)n(w)n(v-w)dwdv \\ &- \frac{1}{\Delta v_i}\int_{v_{i-1}}^{v_i}\int_{v_0}^{v_{max}} \beta(v, w)n(v)n(w)dwdv \end{aligned} \tag{3.21}$$

The main challenge addressed by this method is the evaluation of the double integrals for an arbitrary non-uniform grid. The details of how this is carried out and the final discretised equations can be found in [7].

To extend the method to the two-PBE model, the corresponding terms for the equation for the primary particle number density need to be evaluated. A case where a particle at interval j collides with a particle at interval k forming a new particle at interval i is considered. The change in the number of aggregates dN_i and the change in the number of primary particles $dN_{p,i}$ are then related as follows:

$$dN_i = -dN_j = -dN_k \tag{3.22}$$

$$dN_{p,i} = -n_{av,j}dN_j + -n_{av,k}dN_k \tag{3.23}$$

The change in primary particle number density $dN_{p,i}$ can thus be extracted from the aggregation term in the PBE for the aggregates, and no further calculation is needed.

3.3.3 Sintering of primary particles

The discretised form of the term corresponding to the sintering of primary particles in the PBE for the primary particles can be derived from Eqs. 3.4 and 3.13 in a straightforward manner:

$$\left.\frac{dN_{p,i}}{dt}\right|_{sint} = \left.\frac{dn_{av,i}}{dt}\right|_{sint} N_i = -\frac{3}{\tau_s}\left[\frac{N_{p,i}}{N_i} - \left(\frac{N_{p,i}}{N_i}\right)^{2/3}\right] N_i \tag{3.24}$$

where the models for characteristic sintering timescale τ_s will be discussed in Section 4.1.5.

3.3.4 Coupling with flow

In order to account for transport in physical space, convection and diffusion terms must be introduced into the PBE. For the CFV-2PBE method, the transport equation for the spatially varying number density $N_i(x,t)$ and $N_{p,i}(x,t)$ has the following form:

$$\frac{\partial N_i}{\partial t} + \frac{\partial (u_j N_i)}{\partial x_j} = \frac{\partial}{\partial x_j}\left(D_{p,i}\frac{\partial N_i}{\partial x_j}\right) + S_a \tag{3.25}$$

$$\frac{\partial N_{p,i}}{\partial t} + \frac{\partial \left(u_j N_{p,i}\right)}{\partial x_j} = \frac{\partial}{\partial x_j}\left(n_{av,i} D_{p,i}\frac{\partial N_i}{\partial x_i}\right) + S_p \tag{3.26}$$

where all PBE terms apart from spatial convection and diffusion have been grouped into the source terms S_a and S_p, while $D_{p,i}$ denotes particle diffusion for section i. Here, the velocity u_j is a cumulative velocity encompassing the flow velocity, U_j, and the thermophoretic velocity, u_j^t. The latter can be computed from the following equation [57]:

$$u_j^t = -0.55\frac{\mu}{\rho T}\frac{\partial T}{\partial x_j} \tag{3.27}$$

where μ and ρ are the gas viscosity and density respectively.

It is important to ensure that the flux of the primary particle number density $N_{p,i}(\mathbf{x},t)$ within a volume section i is consistent with that of the aggregate number density $N_i(\mathbf{x},t)$ within the same volume section i. For the convective fluxes, the primary particles experience the same spatial convection as the aggregates and both convective terms share the same velocity. A slightly different treatment is employed for the diffusion of primary particles, $\frac{\partial}{\partial x_j}\left(n_{av,i} D_{p,i}\frac{\partial N_i}{\partial x_j}\right)$, where the term $D_{p,i}\frac{\partial N_i}{\partial x_j}$ is multiplied with $n_{av,i}$. By doing so, the spatial transport of primary particles are in consistent with that of aggregates. Subsequently, introducing Eq. 3.4, Eq. 3.26 can be written as follows:

$$\frac{\partial N_{p,i}}{\partial t} + \frac{\partial u_j N_{p,i}}{\partial x_j} = \frac{\partial}{\partial x_j}\left[n_{av,i} D_{p,i}\frac{\partial}{\partial x_j}\left(\frac{N_{p,i}}{n_{av,i}}\right)\right] + S_p \tag{3.28}$$

The chain rule in the r.h.s. of the equation can be applied now to obtain:

$$\begin{aligned} \frac{\partial N_{p,i}}{\partial t} + \frac{\partial u_j N_{p,i}}{\partial x_j} &= \frac{\partial}{\partial x_j}\left(D_{p,i}\frac{\partial N_{p,i}}{\partial x_j} - D_{p,i}\frac{N_{p,i}}{n_{av,i}}\frac{\partial n_{av,i}}{\partial x_j}\right) + S_p \\ &= \frac{\partial}{\partial x_j}\left(D_{p,i}\frac{\partial N_{p,i}}{\partial x_j}\right) - \frac{\partial}{\partial x_j}\left(D_{p,i}\frac{N_{p,i}}{n_{av,i}}\frac{\partial n_{av,i}}{\partial x_j}\right) + S_p \end{aligned} \tag{3.29}$$

where the second term in the r.h.s. of the equation accounts for the connection between the transport of soot aggregates and primary particles. A numerical test for the particle transport will be presented in Section 3.4.1.

3.3.5 Complete discretised equations for CFV-2PBE

Assembling all terms, the complete discretised equations for the CFV-2PBE method are:

$$\begin{aligned} \frac{dN_i}{dt} + \frac{\partial (U_j + u_j^t) N_i}{\partial x_j} &= \frac{\partial}{\partial x_j}\left(D_{p,i}\frac{\partial N_i}{\partial x_j}\right) - [NG(v,\mathbf{Y})]\,\Big|_{v_{i-1}}^{v_i} \\ &\quad + \dot{C}_i(v,\mathbf{Y}) + \left.\frac{dN_i}{dt}\right|_{agg} + B_i(\mathbf{Y})\delta(v - v_0) \end{aligned} \tag{3.30}$$

$$\begin{aligned} \frac{dN_{p,i}}{dt} + \frac{\partial (U_j + u_j^t) N_{p,i}}{\partial x_j} &= \frac{\partial}{\partial x_j}\left(n_{av,i} D_{p,i}\frac{\partial N_i}{\partial x_j}\right) - [N_p G(v,\mathbf{Y}))\,\Big|_{v_{i-1}}^{v_i} \\ &\quad + \dot{C}_{p,i}(v,\mathbf{Y}) + \left.\frac{dN_{p,i}}{dt}\right|_{agg} - \frac{3}{\tau_s}\left[\frac{N_{p,i}}{N_i} - \left(\frac{N_{p,i}}{N_i}\right)^{2/3}\right] N_i \end{aligned} \tag{3.31}$$

3.3.6 Coupling of CFV-2PBE with CFD

The CFV-2PBE model has been implemented in the in-house research code BOFFIN. The solution method is based on a second-order finite volume scheme. A fractional step method is adopted with separate fractional steps for convection/diffusion, chemical reaction and PBE. A second-order central difference scheme is applied to discretise the diffusion terms, while a TVD scheme with van Leer's limiter is implemented for the convective terms. For the temporal integration of the convection/diffusion process, the second-order accurate Crank-Nicolson method is applied. The calculation of the chemical reaction step is performed with a backward Euler method, and a modified Newton-Raphson scheme is implemented for solving the resulting system of non-linear equations. The temporal integration of the discretised PBE is not stiff, and therefore the explicit Euler method is used in the PBE fractional step.

3.4 Numerical validation for the CFV-2PBE method

3.4.1 Validation for the convection/diffusion process

In this section, I validate the consistency of the discretisation scheme for the convection/diffusion process of primary particles via a simplified test case, where a fuel jet containing soot aggregates is injected into air. The particle size distribution of the soot aggregate is initialised to have a linear profile. To be more specific, 20 consecutive PBE effective sections are picked randomly (from PBE section 11 to section 30) and initialise these sections with the number density of soot aggregates ranging from 10^{11} to 10^{30} as a geometric sequence with the common ratio of 0.1. Furthermore, this work assumes that each soot aggregate contains ten primary particles and the diffusion coefficient $D_{p,i}$ for each section is the same. Since soot aggregates only experience convection and diffusion process in the test case, the theoretical value for the average number of primary particle per aggregate in the domain should always remain 10 for each effective section. The test case undergoes 2000 time steps with $dt = 1 \times 10^{-5}$ s and the results are collected at two heights (HAB = 5 mm and 20 mm) along the centreline.

Under the assumption of an identical diffusion coefficient, the correct transport of the particles via convection and diffusion should yield a PSD of the same shape at different spatial locations. This is indeed accomplished, as shown in Fig. 3.2a. Fig. 3.2b shows that, at two probe locations in the domain, each effective volume section contains soot aggregates that have ten primary particles per aggregate. Another two probes are placed in a different radial location, $r = 10$ mm, to validate the transport along the radial direction. The results are identical and thus not shown for brevity.

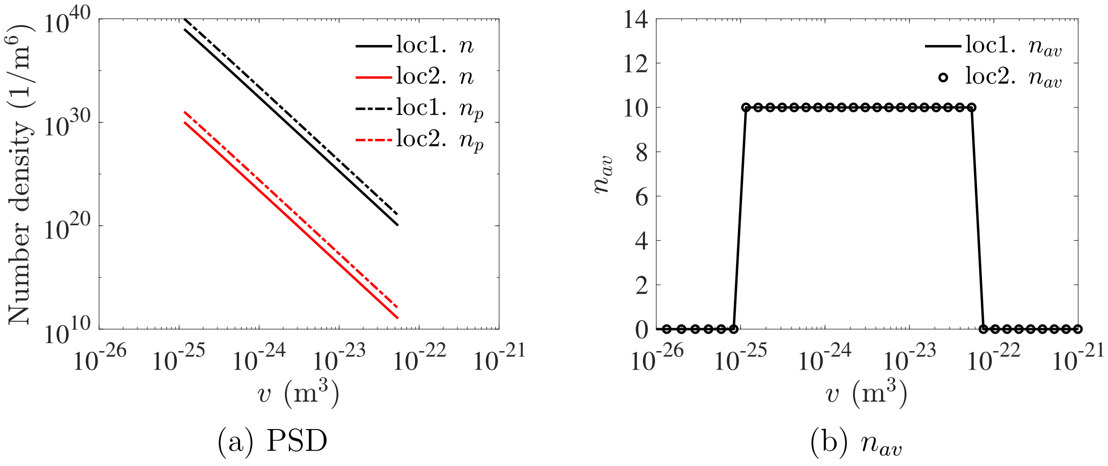

(a) PSD (b) n_{av}

Figure 3.2: (a) PSD of soot particles, and (b) the average number of primary particle per aggregates collected at two probe locations along the centreline. The black line represents location 1 at HAB 5 mm; the red line represents location 2 at HAB 20 mm.

3.4.2 Self-preserving distribution of aggregates

Prior to be employed in the flame, the CFV-2PBE method will be validated by computing the self-preserving distribution of aggregates and comparing it to the study of Vemury and Pratsinis [170]. In these calculations, it is assumed that the primary particle size remains the same and the particle growth is only by aggregation in both the free molecule and continuum regimes. The expressions for the collision frequencies

β are the same as in Eqs. 4 and 6 in Ref. [170] and are reminded here:

$$\begin{aligned}\beta^f(v_i, v_j) =& \sqrt{\frac{\pi k_b T}{2\rho_s}}(\frac{1}{v_i} + \frac{1}{v_j})^{\frac{1}{2}}(d(v_i) + d(v_j))^2 \\ \beta^c(v_i, v_j) =& \frac{2k_b T}{3\mu}(\frac{1)}{d(v_i)} + \frac{1)}{d(v_j)})(d(v_i) + d(v_j))\end{aligned} \tag{3.32}$$

The process is simulated in a batch reactor via the in-house code CPMOD. In all computations, the number density of the initially monodisperse particles is $N_0 = 1 \times 10^{13}$ m^{-3}, the initial particle size is $v_{p_0} = 1 \times 10^{-27}$ m^3 and the fractal prefactor (Eq. 3.5) is $k_f = 1$. The particle density is that of soot particles, and the temperature is set to $T = 1700$ K. The dimensionless particle volume is $\eta = Nv/V$, and the dimensionless particle number density function is $\Phi = Vn/N^2$, where V and N are the total particle volume fraction and number concentration respectively [171]. For a given D_f, the self-preserving distribution is attained when the distribution in the (η, Φ) coordinates does not change any more with time. In the first calculation, all the particles are assumed to be aggregates (by setting the critical diameter d_c smaller than the volume-equivalent diameter of the first volume section), and no sintering is considered. Fig. 3.3 shows the self-preserving distribution of aggregates in the free molecule and continuum regime for several values of D_f, while Fig. 3.4 shows the geometric standard deviation as a function of D_f. In all cases, the results are in excellent agreement with those of Vemury and Pratsinis [170].

The impact of sintering is now introduced by employing different sintering rates over the entire size range. Figure. 3.5 shows the self-preserving distribution of aggregates with $D_f = 2.0$ in the free molecule regime, with the sintering rate increasing from zero (Case 4) to instantaneous coalescence (Case 1). Case 4 yields the same self-preserving distribution as that of $D_f = 2.0$, while instantaneous coalescence yields the self-preserving distribution for spherical particles. When a finite sintering rate is employed, self-preserving distributions with intermediate shapes are obtained. A similar pattern is found in both free molecule and continuum regimes, and only the case for $D_f = 2.0$ in the free molecule regime is shown.

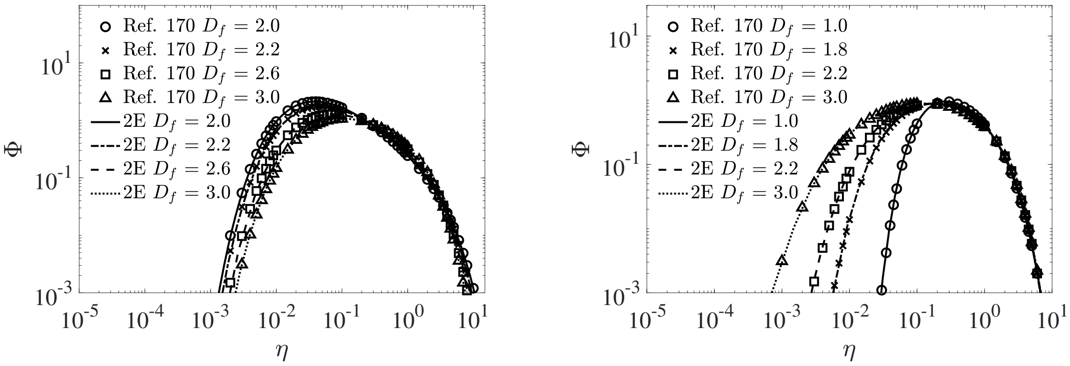

(a) Free molecule regime (b) Continuum regime

Figure 3.3: Self-preserving distribution of aggregates with varying D_f in the free molecule and continuum regimes, comparison with the results by Vemury and Pratsinis [170].

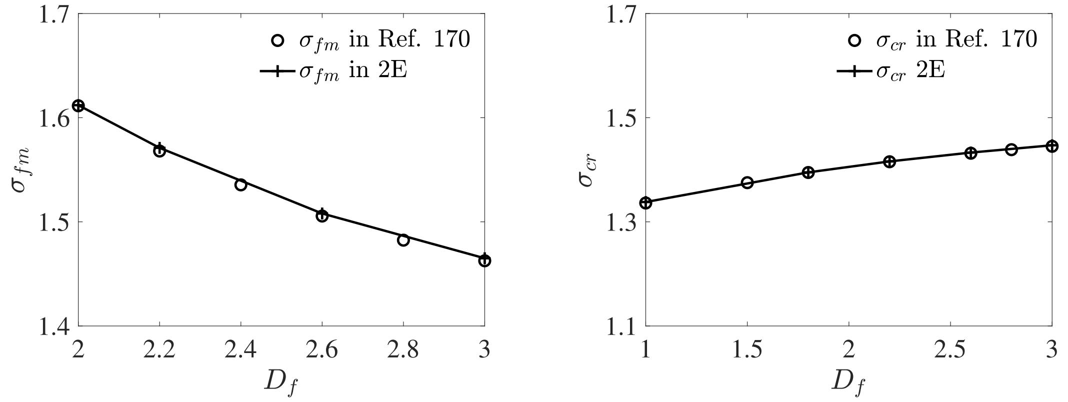

(a) Free molecule regime (b) Continuum regime

Figure 3.4: Geometric standard deviation of the self-preserving distribution of aggregates as a function of D_f in the free molecule and continuum regimes, comparison with the results by Vemury and Pratsinis [170].

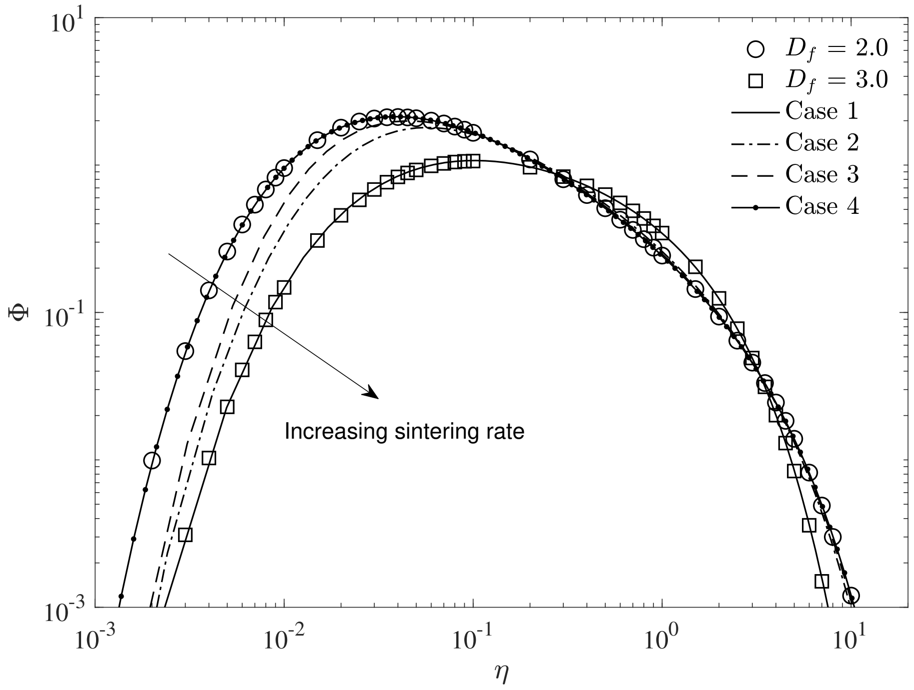

Figure 3.5: Self-preserving distribution of aggregates having $D_f = 2.0$ in free molecule regime under different sintering rates. The dots and the squares represent the results by Vemury and Pratsinis [170] for $D_f = 2.0$ and spherical particles, respectively. The sintering rate increases from zero (Case 4) to instantaneous coalescence (Case 1).

Chapter 4

Application to the Santoro laminar non-premixed sooting flame

In this chapter, the one-PBE and two-PBE approaches are coupled with CFD and applied to the simulation of the Santoro laminar non-premixed co-flow sooting flame. The main objective is to conduct a systematic study of the two-PBE approach, by comparing it with the one-PBE approach and investigating the effect of key parameters related to the evolution of soot morphology in both cases. Moreover, as one of the objectives is to discover the potential of CFD-PBE method for applications in the turbulent flame, I choose the Santoro laminar non-premixed co-flow sooting flame for: a) the flame has been studied extensively, providing a detailed data set to compare with, and b) the flame requires at a minimum a 2D simulation, in which case PBE must be coupled with CFD, and c) the simulation shares some similarities with applications in turbulent flame in terms of the fact that the interaction between flow, chemistry and soot must be resolved properly coupled with a CFD code and applied to the modelling of the laminar co-flow diffusion flame of Santoro et al. [172].

In the following, I first present a comprehensive soot kinetic model with the finite rate of fusing process for soot primary particles, followed by a brief introduction of the experiment and numerical set-up. Subsequently, the method is coupled with a CFD code and applied to the modelling of the laminar co-flow diffusion flame of Santoro et al. [172]. Apart from comparison with experimental results, an analysis of the effect of key parameters is conducted, which allows a discussion of the potential and limitations of the one-PBE and two-PBE approaches.

4.1 Soot kinetics

4.1.1 Gas-phase chemistry and radiation

A detailed chemical mechanism, due to Blanquart et al. [46], is employed in this study. The mechanism was developed based on a series of earlier mechanisms starting from the GRI 3.0 mechanism, focusing on the important species for soot formation such as acetylene, the C_3H_4 isomers, propene and butadiene. It contains 149 species and 1651 reactions, accounting for the formation of larger PAH species up to cyclopenta[cd]pyrene ($C_{18}H_{10}$). The complete mechanism has been validated for a large set of fuels ranging from methane to iso-octane in laminar premixed and counterflow diffusion flames.

The radiation model in my study is based on the hypothesis of optical thinness. Following [173], the radiation heat loss $\dot{Q}$ (in Eq. 2.48) in enthalpy $h(\mathbf{Y}, \mathbf{N})$ due to gas phase species and soot yields the following expression:

$$\dot{Q} = -\frac{4\sigma}{\hat{\rho}} \left(T^4 - T_b^4\right) \sum_{i=1}^{4} a_{p,i}(T) p_i - \frac{4\sigma}{\hat{\rho}} C_s f_v \left(T^5 - T_b^5\right) \tag{4.1}$$

where σ is the Stefan-Boltzmann constant, T indicates temperature, $i = 1, ..., 4$ represents index for major radiating species H_2O, CO_2, CH_4 and CO, p_i denotes the partial pressure of species i and $a_{p,i}(T)$ is the corresponding Planck mean absorption coefficient dependent on temperature. For the soot radiation, a polynomial curve fit expression of the RADCAL model is adopted [174]. The ambient temperature $T_b = 295$ K, f_v is the soot volume fraction and constant $C_s = 1307$ [173].

4.1.2 Nucleation and condensation

The model for soot nucleation and condensation employed in this study is due to Blanquart and Pitsch [53]. In this model, the self-collision of two PAHs forms a dimer, which is an intermediate state between the gaseous polycyclic aromatic hydrocarbons (PAH) and solid soot particles. The dimers are then consumed either by self-coalescence to form soot nuclei or by condensation onto the surface of soot particles. These processes are depicted in Fig. The dimerisation of eight PAHs, from naphthalene ($C_{10}H_8$) up to cyclopenta[cd]pyrene, ($C_{18}H_{10}$) is considered. The self-collision rate $\omega_{\mathrm{PAH},i}$ for a certain PAH_i is given by the following expression:

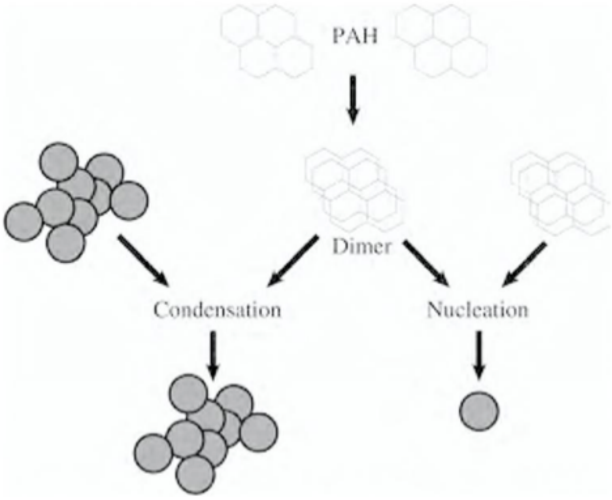

Figure 4.1: Nucleation and condensation of dimers. The illustration is adapted from [53].

$$\omega_{\mathrm{PAH},i} = \gamma_i \sqrt{\frac{4\pi k_\mathrm{B} T}{m_i}} d^2_{\mathrm{PAH},i} [\mathrm{PAH}]_i^2 {N_\mathrm{A}}^2 \tag{4.2}$$

where γ_i is the sticking coefficient factor for PAH_i, N_A is the Avogadro number, k_B is the Boltzmann constant, m_i is the mass of the particle PAH_i, T is the gas temperature and $d_{\mathrm{PAH},i}$ is the diameter of a PAH_i particle given by the following expression [40]:

$$d_{\mathrm{PAH,i}} = D_\mathrm{A} \sqrt{\frac{2n_{c,i}}{3}} \tag{4.3}$$

where D_{A} is the size of a single aromatic ring of $1.395\sqrt{3}$ Å and $n_{c,i}$ is the number of C atoms in a PAH$_i$ molecule. The PAHs involved in the dimerisation and their corresponding parameters are listed in Table 4.1:

Table 4.1: List of species involved in the dimerisation with their mass (in amu) and sticking coefficients [53].

Species name	**Formula**	m_i	γ_i
Naphthalene	$C_{10}H_8$	128.17	0.0010
Acenaphthylene	$C_{12}H_8$	152.20	0.0030
Biphenyl	$C_{12}H_{10}$	154.21	0.0085
Phenathrene	$C_{14}H_{10}$	178.24	0.0150
Pyrene	$C_{16}H_{10}$	202.26	0.0250
Acephenanthrylene	$C_{16}H_{10}$	202.26	0.0250
Fluoranthene	$C_{16}H_{10}$	202.26	0.0250
Cyclo[cd]pyrene	$C_{18}H_{10}$	226.28	0.0390

Because of the small size of the PAH molecule, an average volume v_{dimer} is used to represent the different volume of dimers produced by the self-collision of the eight PAHs ($m = 8$):

$$v_{\mathrm{dimer}} = \frac{\sum\limits_{i=1}^{m} \omega_{\mathrm{PAH},i} 2 v_{\mathrm{PAH},i}}{\sum\limits_{i=1}^{m} \omega_{\mathrm{PAH},i}} \tag{4.4}$$

where m is the number of PAHs considered. Note that v_{dimer} will vary in the calculation depending on the local PAHs concentration. The dimers are assumed to be in quasi-steady state as a result of the high collision frequency with other dimers or soot particles. Consequently, their production and consumption rates are equal and a quadratic equation of the following form is solved to obtain the dimer concentration:

$$a_{nuc}[\mathrm{dimer}]^2 + b_{cond}[\mathrm{dimer}] = \sum_{i=1}^{m} \omega_{\mathrm{PAH},i} \tag{4.5}$$

The coefficients a_{nuc} and b_{cond} are determined by the dimer consumption due to nucleation and condensation respectively, and the expressions that yield them will be shown in the following discussion. The positive root of Eq. 4.5 is accepted as the dimer concentration.

Coalescence of two dimers leads to the formation of soot nuclei [53]. The nucleation rate, w_{nuc}, takes the following form:

$$w_{nuc} = E_F \left(\frac{3}{4\pi}\right)^{1/6} \sqrt{\frac{6k_{\mathrm{B}}T}{\rho_s}} 4\sqrt{2} v_{\mathrm{dimer}}^{1/6} [\mathrm{dimer}]^2 {N_{\mathrm{A}}}^2 \tag{4.6}$$

where $E_F = 2.2$ is the Van der Waals enhancement factor [175] and $\rho_s = 1800$ kg/m^3 is the density of soot particle. Thus, the nucleation source term B in Eq. 3.1 is written as:

$$B = w_{nuc} \frac{2v_{\mathrm{dimer}}}{dv_{nuc} v_{m,nuc}} \tag{4.7}$$

where $v_{m,nuc}$ is the representative volume (midpoint) in the section that covers the volume of nuclei and dv_{nuc} is the interval of that section, respectively. The coefficient a_{nuc} in Eq. 4.5 takes the form:

$$a_{nuc} = 2 \frac{w_{nuc}}{[\mathrm{dimer}]^2} \tag{4.8}$$

where the term 2 indicates the fact that two dimers are consumed to form a soot nucleus.

When a dimer collides with a large soot particle, the two PAH molecules will deposit on the surface [53]. In a section i, the change of the number density due to condensation is classified into three types: a) condensation of dimers on particles of section i, $\omega_{cond,dimer \to i}$, b) condensation of dimers on particles of section $i-1$ that will enter into section i, $\omega_{cond,i-1 \to i}$, and c) condensation of dimers on particles of section i that will go to section $i+1$, $\omega_{cond,i \to i+1}$. These contributions will be included via a condensation source term $\dot{C}(v, \mathbf{Y})$ into Eq. 3.3 in a manner ensuring that the total volume added by condensation is conserved. The impact on primary particle number density is addressed later in this section. The condensation rate for each of the aforementioned types is evaluated as follows [29]:

$$\omega_{cond,\text{dimer}\to i} = [\text{dimer}]N_\text{A}\int_{v_{i-1}}^{v_i-v_\text{dimer}} \beta_{d,i}N(w)dw \qquad = [\text{dimer}]N_\text{A}\beta_{d,i}(dv_i - v_\text{dimer})N_i \tag{4.9}$$

$$\omega_{cond,i-1\to i} = [\text{dimer}]N_\text{A}\int_{v_{i-1}-v_\text{dimer}}^{v_{i-1}} \beta_{d,i-1}N(w)dw = [\text{dimer}]N_\text{A}\beta_{d,i-1}v_\text{dimer}N_{i-1} \tag{4.10}$$

$$\omega_{cond,i\to i+1} = [\text{dimer}]N_\text{A}\int_{v_i-v_\text{dimer}}^{v_i} \beta_{d,i}N(w)dw \qquad = [\text{dimer}]N_\text{A}\beta_{d,i}v_\text{dimer}N_i \tag{4.11}$$

where the collision frequency of a dimer and a soot particle in the section (v_{i-1}, v_i) has been regarded as constant and calculated with the representative volume, $v_{m,i}$, as follows:

$$\beta_{d,i} = 1.3\sqrt{\frac{\pi k_\text{B}T}{2\rho_s}}\left(d_\text{dimer} + d_{g,i}\right)^2\sqrt{\frac{1}{v_\text{dimer}} + \frac{1}{v_{m,i}}} \tag{4.12}$$

where the collision diameter of the particle $d_{g,i}$ at section i is evaluated according to Eqs. 3.4 and 3.5, and the amplification factor of 1.3 is due to Van der Waals interactions [176]. Therefore, the coefficient b_{cond} in Eq. 4.5 is determined as:

$$b_{cond} = \frac{\sum\left(\omega_{cond,\text{dimer}\to i} + \omega_{cond,i-1\to i} - \omega_{cond,i\to i+1}\right)}{[\text{dimer}]} \tag{4.13}$$

where special treatment is applied for the first volume section to cancel type 2 condensation $\omega_{cond,i-1\to i}$. With the help of Eq. 4.8 and Eq. 4.13, one solves the quadratic equation Eq. 4.5 to obtain the concentration of dimer. Now the condensation source term $\dot{C}_i(v, \mathbf{Y})$ for the number density of aggregates in the section (v_{i-1}, v_i) can be evaluated as:

$$\dot{C}_i(v, \mathbf{Y}) = \left(\omega_{cond,\text{dimer}\to i} + \omega_{cond,i-1\to i} - \omega_{cond,i\to i+1}\right)\frac{v_\text{dimer}}{v_{m,i}dv_i} \tag{4.14}$$

The first type of condensation will not alter the average number of primary particles per aggregate. As the mass added by condensation of dimer is conserved via a source term for the aggregate number density, it is assumed that the number of primary particle per aggregate for the newly generated aggregate is the same as that for the aggregates in the same section. Consequently, the condensation source term for primary particles is formulated as follows:

$$\dot{C}_{p,i}(v,\mathbf{Y}) = (\omega_{cond,\text{dimer}\to i} n_{av,i} + \omega_{cond,i-1\to i} n_{av,i-1} - \omega_{cond,i\to i+1} n_{av,i})\frac{v_{\text{dimer}}}{v_{m,i} dv_i} \tag{4.15}$$

4.1.3 Surface growth and oxidation

Soot surface growth and oxidation are modelled via the H-abstraction/C_2H_2 addition (HACA) mechanism, originally proposed by Frenklach and Wang [39]. The reaction rates are calculated based on the parameters of Tables 2 and 3 in [53]. The theoretical maximum value of the overall site density, χ_{soot}, has been estimated to be 2.3×10^{19} sites/m^2 [39]. The concept of surface reactivity was introduced in the HACA mechanism in the form of a parameter, α, and the main uncertainty in HACA lies in the determination of this parameter. Constant values were employed in early research [39], but later work considered it to be a function of the local temperature [54] and other parameters, such as particle size [41]. Recent studies [55,96] proposed a more complex model that accommodates the effects of both temperature and residence time. As the focus of this study is on the investigation of the CFV-2PBE method and the fusing of soot primary particles, a simple model for α was adopted, in which α is a function of temperature only, assuming the form $\alpha = \mathrm{a} \cdot \exp(9000/T)$ [54]. The pre-exponential factor, a, was adjusted such that the peak value for integrated soot volume fraction is matched to a satisfactory degree with the experimental data (Section 4.3.1). The net growth rate (including oxidation) is calculated as follows:

$$G(v,\mathbf{Y}) = \frac{a(v)}{\rho_s} R_g(\text{HACA}) \tag{4.16}$$

where $a(v)$ denotes the soot surface area and $R_g(\text{HACA})$ is the mass growth rate, which is a function of α, χ_{soot}, reaction rates and the local concentrations of species associated with HACA mechanism [39, 53]. The reaction rates are summarised in

Table 4.2 [53].

Table 4.2: Rate coefficients for surface reactions in Arrhenius form ($k = AT^n \exp(-E/RT)$). Units are m^3, K, kcal, kmol, s.

Reactions	A	n	E
$C(s)-H + H \rightleftharpoons C(s)- + H_2$	1.00×10^{5}	1.80	16.35
	8.68×10^{1}	2.36	6.09
$C(s)-H + OH \rightleftharpoons C(s)- + H_2O$	6.72×10^{-2}	3.33	1.46
	6.44×10^{-4}	3.79	6.67
$C(s)- + H \rightleftharpoons C(s)-H$	4.17×10^{10}	0.15	0.00
	1.13×10^{13}	-0.06	-113.78
$C(s)- + C_2H_2 \longrightarrow C(s)-H + H$	2.52×10^{6}	1.77	-3.24
$C(s)- + O_2 \longrightarrow 2CO + \text{products}$	2.20×10^{9}	0.00	-7.5
$C(s)- + OH \longrightarrow CO + \text{products}$	Reaction probability		0.13

4.1.4 Aggregation

The collision kernel β takes different forms depending on the Knudsen number, $\mathrm{Kn} = 2\lambda_g/d$, where λ_g is the gas mean free path and d is the particle diameter. Three regimes can be identified, namely the free-molecular regime $\mathrm{Kn} > 10$, continuum regime ($\mathrm{Kn} < 0.1$) and transition regime ($0.1 < \mathrm{Kn} < 10$). The equations are [62, 68]:

$$\begin{aligned}
\beta^f(v_i, v_j) =& E_F \sqrt{\frac{\pi k_\mathrm{B} T}{2\rho_s}} \left(\frac{1}{v_i} + \frac{1}{v_j}\right)^{\frac{1}{2}} (d(v_i) + d(v_j))^2 \\
\beta^c(v_i, v_j) =& \frac{2k_\mathrm{B} T}{3\mu} \left(\frac{\mathrm{Cu}(v_i)}{d(v_i)} + \frac{\mathrm{Cu}(v_j)}{d(v_j)}\right) (d(v_i) + d(v_j)) \\
\beta^t(v_i, v_j) =& \frac{\beta^{fm}(v_i, v_j)\beta^c(v_i, v_j)}{\beta^{fm}(v_i, v_j) + \beta^c(v_i, v_j)}
\end{aligned} \tag{4.17}$$

where $\mathrm{Cu}(v_i) = 1 + 1.257\mathrm{Kn}$ is the Cunningham slip correction factor and $d(v)$ represents either the spherical particle diameter or the collision diameter of an aggregate that can be evaluated from Eq. 3.5. For the current work, the fractal dimension and fractal prefactor for all aggregates are taken to be $D_f = 1.8$ [69] and $k_f = 2.4$ [67], respectively.

4.1.5 The fusing of primary particles

The term 'sintering' is usually employed in material science and also in the study of inorganic nanoparticles such as silica and titania to denote the fusing of primary particles. However, as recently discussed by Michelsen et al. [15], this terminology may be inappropriate for soot, where the physical mechanisms are different. In accordance with that recommendation, in this work, the term 'coalescence' refers to the instantaneous coagulation of incipient particles to form spherical particles (i.e. the coagulation events that occur below the cut-off point in the two-PBE model), while the merging of primary particles within aggregates will be referred to generally as fusing. The term 'sintering' is retained in this study when referring to inorganic nanoparticles.

The characteristic timescale of fusing plays an important role in shaping the structure of an aggregate. The sintering behaviour of several nanoparticles has been studied in the aerosol community but, to my knowledge, such information is not available on soot. As a result, the few studies that have attempted to employ a finite rate of the fusing of soot primary particles have been based on extrapolation from sintering models for different nanoparticles. In a study of laminar premixed ethylene sooting flames, Chen et al. [99] employed the expression of τ_s for silica particles [177]:

$$\tau_s = A_s d_{p,i} \exp\left[\frac{E_a}{T}\left(1 - \frac{d_c}{d_{p,i}}\right)\right] \tag{4.18}$$

where A_s, d_i and E_a are the pre-exponential factor, the diameter of the sintering primary particle and the activation energy, respectively. On the other hand, Veshkini et al. [98] employed an expression for the sintering of titanium oxide [178] in the Santoro laminar ethylene diffusion flame:

$$\tau_s = A_s d_{p,i}^4 T \exp\frac{E_a}{T} \tag{4.19}$$

The coalescence between two spherical particles in contact is a result of various molecular transport mechanisms in the contact region [57]. For liquid particles, such as

Table 4.3: Summary of parameters in the sintering models and their units.

Variable	Silica particle model	Titania particle model
	Range given in [99] (units)	Value given in [90, 178] (units)
A_s	1.1×10^{-14} (s/m)	7.44×10^{16} $\left(\mathrm{s}/\left(\mathrm{K}\cdot\mathrm{m}^4\right)\right)$
E_a	$1.8 \times 10^4 \leqslant E_a \leqslant 1.8 \times 10^5$ (K)	3.31×10^4 (K)
d_c	$1 \leqslant d_c \leqslant 5$ (nm)	-

silica, coalescence is driven by viscous flow. On the other hand, transport by diffusion is the dominant route for the coalescence of crystalline titania nanoparticles in contact. Even in the context of SiO_2, as indicated in a recent work by Goudeli et al. [179], different sintering models show distinct differences in the predicted primary particle diameter and collision diameter. The predicted fusing behaviour of soot particles could be significantly different depending on the sintering model employed, and transposing these kinetics to soot inevitably brings uncertainties into soot modelling. As the current information on the fusing of soot primary particles is not sufficient to reach consensus, in the current study models for both silica and titania will be applied and tested, and their impact on the model outcome will be investigated via a parametric analysis. As a base case for adopting the sintering model of silica particles, a set of optimised parameters from the work of Chen et al. [99] is employed, while for the titania model I adopt the data of [90, 178], also applied in Ref. [98]. A detailed summary can be found in Table 4.3.

Before applying the models to the flame, I conduct here a sensitivity analysis of the parameters in both sintering models to provide guidance for their use in the sooting flame simulation. In Fig. 4.2 I show, for each model, the sintering timescale at two thermal conditions that are typical of the regions of centreline (1600 K) and the flame front (2000 K) in the forthcoming application to the flame. Since varying the pre-exponential factor A_s in both models only causes a vertical movement of the curve, the impact of this parameter is not shown. The dotted line represents an effective sintering timescale, above which the sintering is nearly ceased. It can be seen that the temperature has a profound impact on the sintering rates for both models. At a

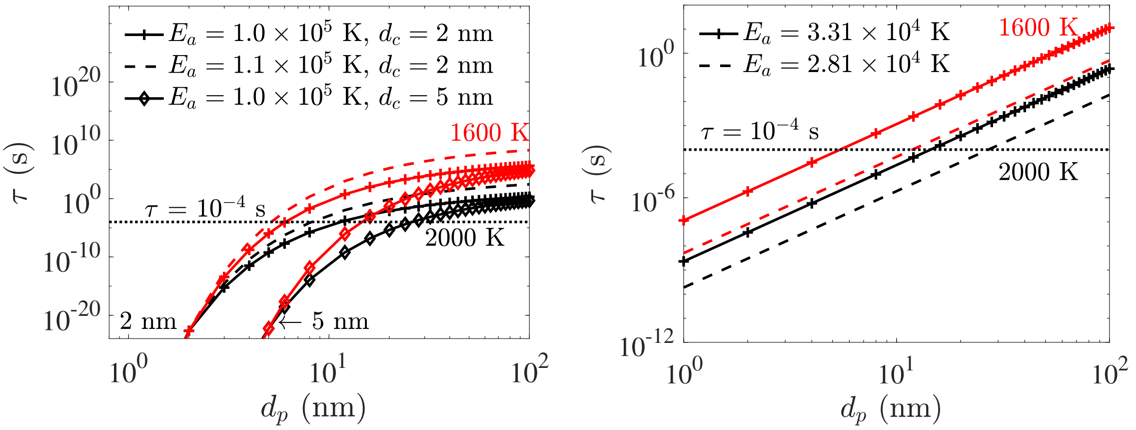

(a) Silica model (b) Titania model

Figure 4.2: The impact of varying each model parameter on the characteristic sintering time for (a) the silica model, (b) the titania model. The characteristic time τ is plotted as a function of primary diameter for two different temperatures. The sintering timescale at 1600 K is marked with red colour, while the sintering timescale at 2000 K is marked with black colour.

certain temperature, the characteristic sintering timescale reaches an asymptote with increasing primary particle diameter d_p in silica model. The position of this asymptote is affected by E_a. When employing the silica model, therefore, one needs to adjust both parameters with caution. On the other hand, there is only one parameter to be adjusted in the titania model. Moreover, the sintering rate is relatively large for smaller particles in titania model, justifying my approach of assuming sintering to be instantaneous for particles less than d_c (Section 3.3.1). In the following applications, the value of critical diameter d_c in the titania model is set to be 3 nm. Below that value, the results show little sensitivity to d_c.

4.2 Flame configuration and numerical set-up

The target flame here is the non-smoking ethylene-air diffusion flame at atmospheric pressure investigated by Santoro et al. [172, 180]. This flame was chosen due to the availability of experimental data [164,181,182] and the fact that it has been the subject of several modelling studies (Refs. [7, 8, 98, 183] among others). Furthermore, unlike flames that can be simulated via one-dimensional formulations, this flame requires full coupling with a CFD code and is thus an intermediate stage before applying the CFV-2PBE method to turbulent flames. The flame consists of a central fuel jet (pure ethylene) of diameter 11.1 mm surrounded by a concentric air co-flow of diameter 101.6 mm at atmospheric pressure and temperature. The inlet flow rates for the fuel and air are 3.85 cm^3/s and 713.3 cm^3/s, equivalent to velocities of 3.98 cm/s and 8.9 cm/s, respectively. An illustration of the burner is shown in Fig. 4.3. The computational domain is cylindrical in shape and spans 160 mm in the axial direction with 200 cells and 55.5 mm in the radial direction with 100 cells (Fig. 4.3). The grid is stretched axially and radially by factors of 1.01 and 1.03, respectively. A convergence study showed that further refinement of the grid was not needed. There is uncertainty regarding the inlet condition, as some amount of heat is transferred from the flame base to the burner nozzle, thus altering the inlet temperature and velocity profiles. According to Guo et al. [184], the prediction can be improved quantitatively with an increase in fuel temperature, and such a strategy has been adopted in several studies [8, 98] where the amount of preheating was chosen to obtain the best match of the results with the experimental data. Since my interest lies in the study of the two-PBE model and the CFV-2PBE method, rather than obtaining the best possible

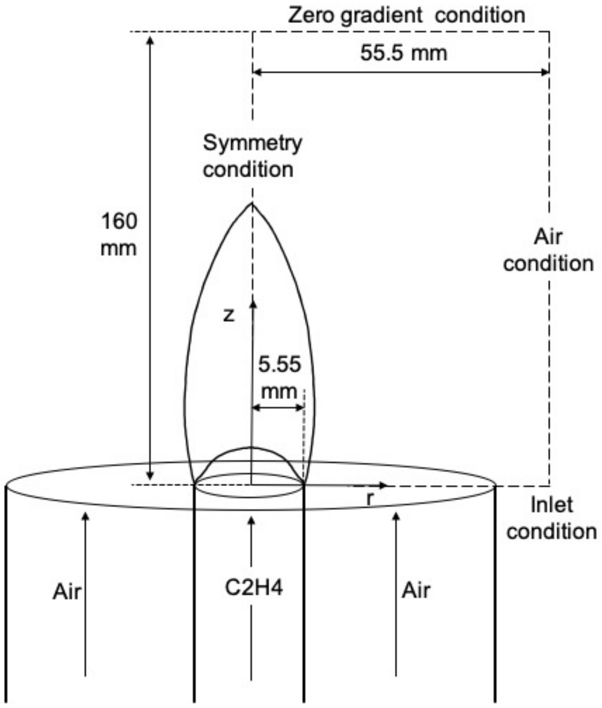

Figure 4.3: Illustration of the burner and the computational domain.

match with experimental data, it was decided to keep adjustments to a minimum, and therefore uniform velocity profiles for fuel at 300 K and air at 300 K have been employed. Regarding the discretisation of the PBE, a geometric grid with 60 intervals in the volume domain corresponding to particle size range from 0.72 nm to 1240 nm is employed, and again grid convergence was tested for cases with 40, 50, 60, 80, and 100 PBE intervals, among which the cases with more than 60 intervals showed converged results.

4.3 Results and discussion

4.3.1 Overall validation

In the following sections, I present the simulation results from both CFV-1PBE and CFV-2PBE methods in the following order. Comparisons of temperature, axial velocity, concentration and integrated soot volume fraction at different heights above burner (HAB) are presented first, followed by an investigation of soot morphology along the flame centreline and the pathline of maximum soot volume fraction at each axial location. Afterwards, a detailed parametric study of the key parameters in both CFV-1PBE and CFV-2PBE models will be conducted. The data available related to soot morphology are summarised in Table 4.4. At each spatial location, a geometric average [185] is applied over the volume-equivalent diameter ranging from 1.5 nm to 1024 nm to provide a good measure of particle size. Note that, for the base case of CFV-1PBE, the cut-off point $d_c = 30.8$ nm, a value that has also been adopted in a recent work of Liu et al. [1], while the sintering model parameters for the base case of CFV-2PBE are $d_c = 5$ nm, $E_a = 10.0 \times 10^4$ K for the silica model and $E_a = 3.31 \times 10^4$ K for the titania model. For the parameter A_s, one may refer to Table 4.3.

The numerical results from both CFV-1PBE and CFV-2PBE (with both sintering models) are both in good agreement with experiments regarding the radial distributions of temperature, axial velocity, OH and C_2H_2 at different HAB, and therefore

Table 4.4: Summary of experimental data on soot aggregates in the flame investigated in this study and their sources.

Soot data	Spatial position		Unit
	Centreline	Pathline having maximum soot f_v	
f_v	[172, 180]	[172, 180]	ppm
d_p	-	[181, 182]	nm
N	-	[180]	m^{-3}
N_p	-	[182]	m^{-3}
n_{av}	-	[182]	-

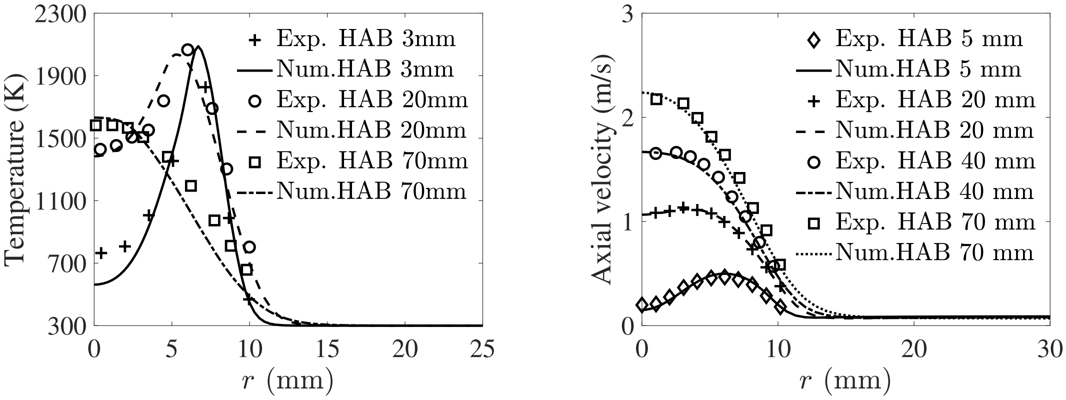

(a) Temperature (b) Axial velocity

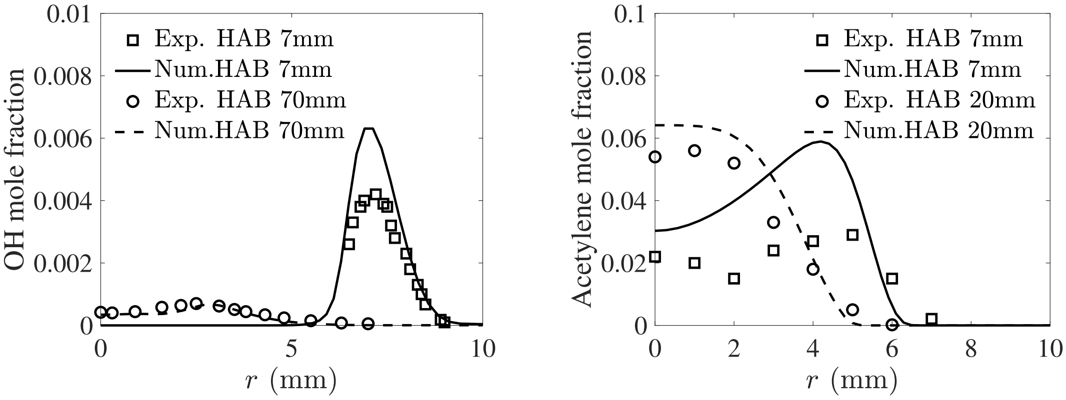

(c) Mole fraction of OH (d) Mole fraction of C_2H_2

Figure 4.4: Comparison of numerical predictions and experimental data in radial direction for (a) temperature (measurement from Ref. [180]), (b) axial velocity (measurement from Ref. [180]), (c) OH mole fraction (measurement from Ref. [180]), and (d) acetylene mole fraction (measurement from Ref. [186]). Only results from CFV-1PBE are shown, as the other models have a similar performance.

only the results generated from the CFV-1PBE method are shown. Fig. 4.4a shows the temperature profile at three different HAB, and the overall shape and trend of the experimental data are well represented. At 3 mm HAB, there is a slight underprediction between $r = 0.0$ mm and $r = 4.0$ mm, most likely due to the effect of preheating. The profiles of axial velocity are also reproduced very well, as shown in Fig. 4.4b. Predicted and measured OH mole fraction profiles are compared in Fig. 4.4c. The simulated profile captures the peak position of OH profiles at both HAB, yet with a considerable overprediction for peak values at 7 mm HAB. It should be noted that the experimental errors for OH measurement with laser-induced fluorescence (LIF) could be as much as 50% [186], hence the agreement is reasonable. Fig. 4.4d shows the acetylene mole fraction profile at 7 mm and 20 mm HAB. The general shape of the curves at both axial locations is well captured, despite some overprediction at the lower region of the flame. A similar level of overprediction can be found in the work by Zhang et al. [162], Veshkini et al. [55], and Akridis and Rigopoulos [34] and, again, a likely cause is fuel preheating. It is worth noting that, while most of the soot mass is added via acetylene addition, the rate-limiting reactions in the current HACA mechanism are the hydrogen abstraction reactions (the forward reactions of No.1 and No.2 in Ref. [53]). Therefore, an accurate prediction of H and, to some extent, OH radicals (which also contribute to oxidation) is more important for surface growth than C_2H_2 [55]. Overall, satisfactory agreement is achieved for the prediction of the thermal and chemical environments that are important in soot prediction.

The integrated soot volume fraction at different HAB, for which experimental data are available, can be examined now. This variable is likely to be dominated by surface reactions, which play a major role in soot mass growth, as has been confirmed by several studies [55,172,180,187,188]. However, as discussed by [188], current knowledge of the surface reactivity of soot is rather limited. The common site density $\chi = 2.3\times10^{19}$ sites/m^2 reported by Frenklach and Wang [39] is viewed as a theoretical limit, and no exact value of χ is currently available [188]. Fig. 4.5a compares the calculated and measured distributions of the integrated soot volume fraction along the flame axis for different values of the prefactor a in the expression for the surface reactivity. With increasing surface reactivity, the peak value of the integrated soot volume fraction experiences a significant increase. Fig. 4.5b shows that HACA surface growth is the dominant mechanism for the soot generation and that the position of the peak value for the profile of the integrated soot volume fraction coincides with the one in surface growth phenomena. As the intention is to investigate the impact of aggregation models, the pre-exponential factor in the surface reactivity expression was adjusted so that the peak value of the integrated soot volume fraction from the simulation is close to that of the experiment, while the values of all the other parameters of the soot model were adopted from the literature without modification. In the following analysis, therefore, the surface reactivity is yielded by the expression $\alpha = 0.0037 \times e^{9000/T}$.

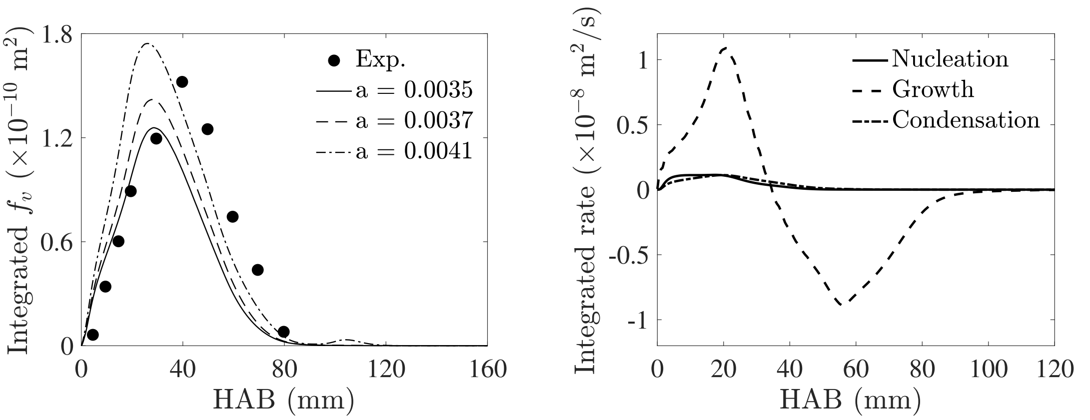

(a) Integrated soot volume fraction (b) Integrated rate for each processes

Figure 4.5: (a) Integrated soot volume fraction along the axial direction for different values of the prefactor a in the expression for the surface reactivity with the CFV-1PBE method (line: calculation, symbol: measurements [180]), and (b) breakdown of the integrated soot volume fraction rate of change due to nucleation, HACA surface reactions and condensation for the case of prefactor a = 0.0037.

Fig. 4.6 shows the calculated integrated soot volume fraction for the base case of CFV-1PBE and CFV-2PBE methods. It can be seen that the soot yield in the in CFV-2PBE method is similar to that from CFV-1PBE method. It must also be noted that, with the current chemical mechanism and soot model, the entire profile appears to be somewhat shifted towards the fuel nozzle, a fact that was also observed in [53].

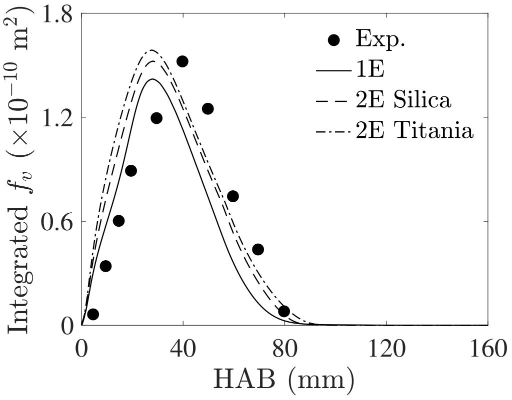

Figure 4.6: Comparison of the numerical predictions and experimental data for the integrated soot volume fraction along the axial direction from the base case of CFV-1PBE method and CFV-2PBE method.

4.3.2 Centreline comparisons

In this section, the numerical results predicted by CFV-1PBE method and CFV-2PBE method with the two sintering models discussed in Section 4.1.5 are presented. Fig. 4.7 shows comparisons of the soot volume fraction and temperature along the centreline with the experimental results. All three models give similar results and underpredict the soot volume fraction by an order of magnitude, while the temperature predictions are in good agreement with the measurements. A possible cause of the discrepancy could be the uncertainty involved in the experimental measurements. The soot volume fraction measurements by Santoro et al. [172, 180] employed the laser extinction/scattering approach with a constant refractive index (RI) without taking into account the soot composition and morphology which, as indicated in a recent work by to Kelesidis and Pratsinis [189], might lead to an overestimation of soot volume fraction by as much as 100%. The underprediction of the soot along the flame centreline has also been observed in the work of Dworkin et al. [8]. Another possible cause could be the soot kinetics. To probe further into this, a breakdown of the source terms contributing to soot volume fraction (nucleation, HACA surface growth, condensation, oxidation by OH and O_2) is shown in Fig. 4.8a. Between HAB 20 mm and 45 mm, nucleation and condensation are the dominant mechanisms. Although a rapid increase for soot surface growth can be seen after HAB 55 mm, this impact is soon cancelled by oxidation due to OH radicals. In the current soot kinetics, nucleation and condensation depend on the dimer concentration, which is highly sensitive to the concentration of PAHs. Fig. 4.8b shows the dominant PAHs (i.e. those whose mole fraction are lager than other PAHs by an order of magnitude). The formation of small PAHs occurs at the first stage of the flame (from HAB = 5 mm to HAB = 20 mm), after which the temperature is stabilised, and the PAHs are gradually consumed. The formation of OH and H starts approximately at HAB = 50 mm. Subsequently, the OH and H radicals trigger the H-abstraction in the HACA mechanism, boosting the surface growth rate for a short distance. The shape of the growth profile is due to the low concentration of C_2H_2 when reaching HAB 60 mm, thus limiting the acetylene addition. In the meantime, the oxidation by the OH thus counters the increase due to surface growth. Other studies [8,55] have also found that the soot mass addition along the centreline is mainly through nucleation and condensation. Such feature explains why the CFV-2PBE provides similar results as CFV-1PBE. One of the major difference between two methods should be reflected in the particle surface area (presented later in Section 4.3.3), which plays a dominant role only in surface growth/oxidation process. Therefore, this underprediction is a feature of the kinetics and is not related to the aggregation model.

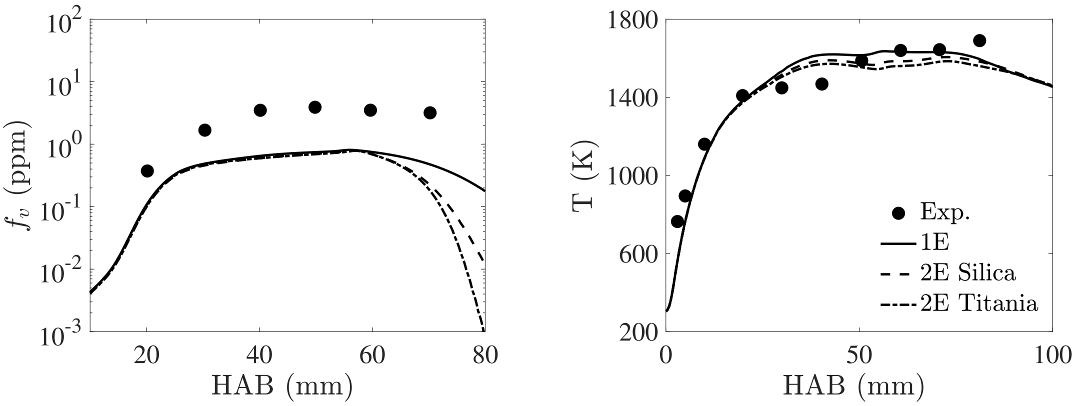

(a) Soot volume fraction (b) Temperature

Figure 4.7: Comparison of numerical predictions by CFV-1PBE and CFV-2PBE with two sintering models with experimental data along the centreline for (a) soot volume fraction (measurement from Refs. [172,180]), (b) temperature (measurement from Refs. [164,180]).

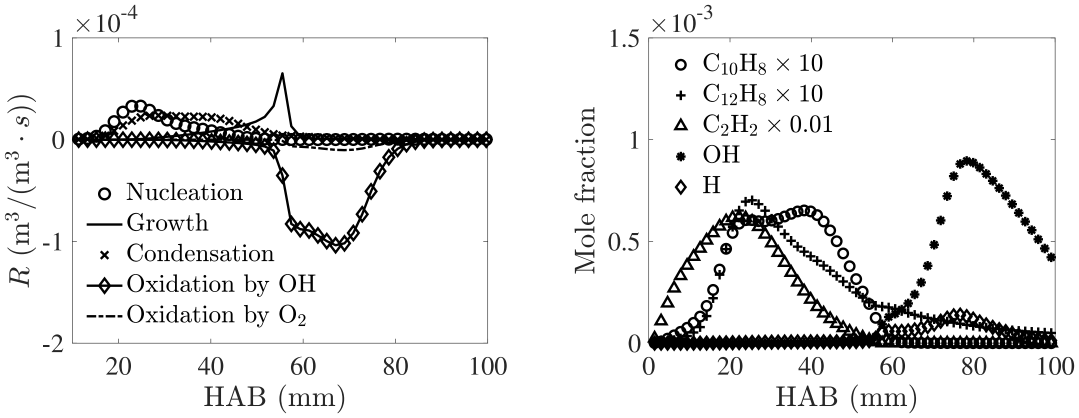

(a) Contribution rates R (b) Species mole fraction

Figure 4.8: The rates of change for each soot formation process and the predicted species mole fractions along the centreline by CFV-1PBE method.

In Fig. 4.9, the particle size distribution (PSD) of soot aggregates is shown at three locations along the centreline. Due to the lack of experimental data for the PSD, no comparison with experiments can be made. It is notable, however, that the predictions of the three models differ considerably, in spite of the soot yield being similar. In the nucleation region, most of the particles are newly formed and represent a unimodal PSD, and the differences between the three models are moderate. In the growth region, where growth and coagulation modes for soot particle are expected, bimodal shapes of PSD are predicted by the CFV-2PBE model with the sintering models, very different from the CFV-1PBE prediction. This feature illustrates the strong impact of primary particle size on the PSD, an observation consistent with the findings of a recent study by Bouaniche et al. [71], where the impact of primary particle size on the PSD was investigated in a premixed flame using a hybrid stochastic/fixed-sectional method. When soot enters the oxidation zone, the PSD becomes unimodal again. A further investigation is made along the annular pathline with the maximum soot volume fraction as a function of HAB in the following section, where the soot particles experience high temperatures near the flame front.

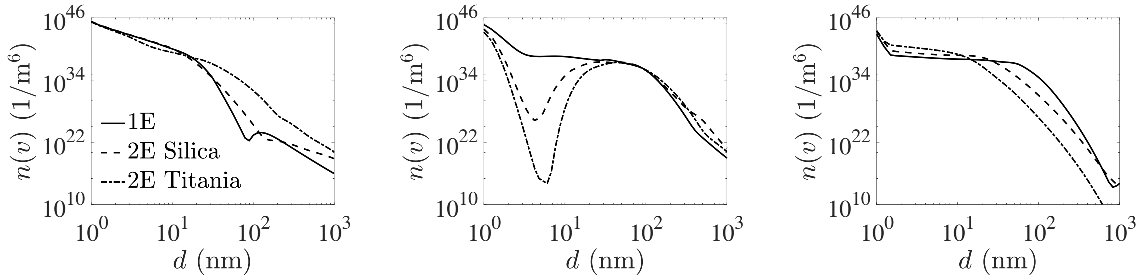

(a) 15mm HAB (b) 50mm HAB (c) 80mm HAB

Figure 4.9: Comparison of the numerical predictions of soot aggregate number density distribution by CFV-1PBE and CFV-2PBE of two sintering models at three probe locations along the centreline: (a) 15 mm HAB (nucleation region), (b) 50 mm HAB (growth region), and (c) 80 mm HAB (oxidation region).

4.3.3 Comparisons along pathline of maximum soot volume fraction

In this section, the results of both PBE models are compared with the experimental results along the soot particle path exhibiting maximum soot volume fraction. Moreover, the effect of the key parameters in both modelling approaches (one-PBE and two-PBE) are analysed in order to assess the effect of modelling uncertainties. As the focus of the work is on aggregate morphology and the evolution of soot fine structure, the discussion will focus on the parameters related to these aspects, rather than on parameters such as surface reactivity, which are implemented in the same way in both approaches.

Firstly, I investigate the impact of the artificial cut-off point that controls the morphology of soot in CFV-1PBE model. In Fig. 4.10, I compare the results from CFV-1PBE with $d_c = 30.8$ nm and $d_c = 20$ nm along the maximum soot pathline where intense growth and high temperatures are expected. A smaller cut-off point would, in principle, lead to a larger number of primary particles within the aggregate, and this is indeed the case, as shown in Figs. 4.10b,c. Also, as indicated in Figs. 4.10e,f, a larger surface area given by the case of $d_c = 20$ nm would enhance soot surface growth, leading to a larger soot yield. As expected by the construction of the one-PBE model, the average diameter of primary particles in both cases grows up to the size of the cut-off point and remains constant (see Fig. 4.10d). The difference in the total number density N is rather significant in the initial region, as shown in Fig. 4.10a. This is because a smaller cut-off point would lead to an earlier formation of aggregates, thus enhancing aggregation and leading to a decrease in the aggregate number density. In practice, one needs to choose the cut-off size d_c with care to achieve a good prediction of both soot volume fraction and soot morphology.

For the CFV-2PBE model, the need is shifted to the determination of the rate of fusing for the primary particles, which shapes the structure of soot aggregates. Therefore, I investigate the impact of the key parameters in the two sintering models employed in the framework of CFV-2PBE. For the silica model, cases having critical diameter $d_c = 5$ nm with different activation energy are investigated, while for the titania model there is only the activation energy to vary. For the titania model, soot aggregates tend to form earlier in the case of slow sintering rate (solid line), leading to smaller aggregate number density for the same reason as in the case of the CFV-1PBE and more primary particles (Fig. 4.11a and b). The slow sintering rate also leads to a greater number of primary particles and larger surface area, and thus larger soot volume fraction, as indicated in Figs. 4.11c,e,f. A similar pattern can be seen in the silica model. Overall, a fast sintering rate in either sintering models would enhance the fusing of the primary particles, resulting in larger primary particles. Consequently, the model behaviour shares a similar pattern with the case of a large cut-off point in CFV-1PBE method, except for the prediction of the average diameter of primary particles. Fig. 4.11d shows that there is a significant difference in the predicted primary particle size with different sintering behaviour, which is in accordance with the study of Goudeli et al. [179].

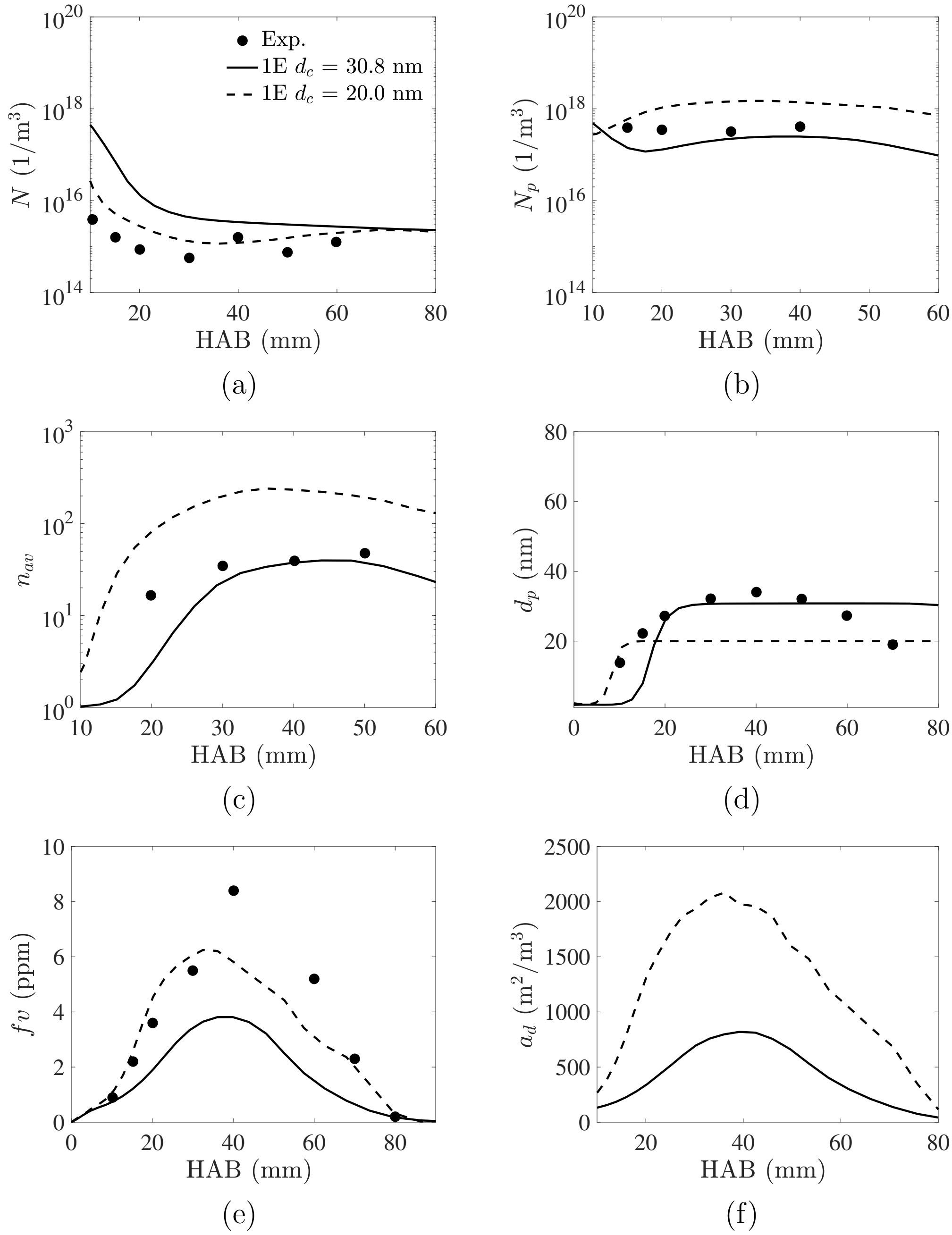

Figure 4.10: Comparison of the soot morphology along the annular pathline containing maximum soot volume fraction using different cut-off points for the CFV-1PBE model. (a) Number density of aggregates, (b) number density of primary particles, (c) average number of primary particles per aggregate, (d) diameter of primary particles, (e) soot volume fraction, and (f) surface area density. Solid line: CFV-1PBE with $d_c = 30.8$ nm; dashed line: CFV-1PBE with $d_c = 20.0$ nm.

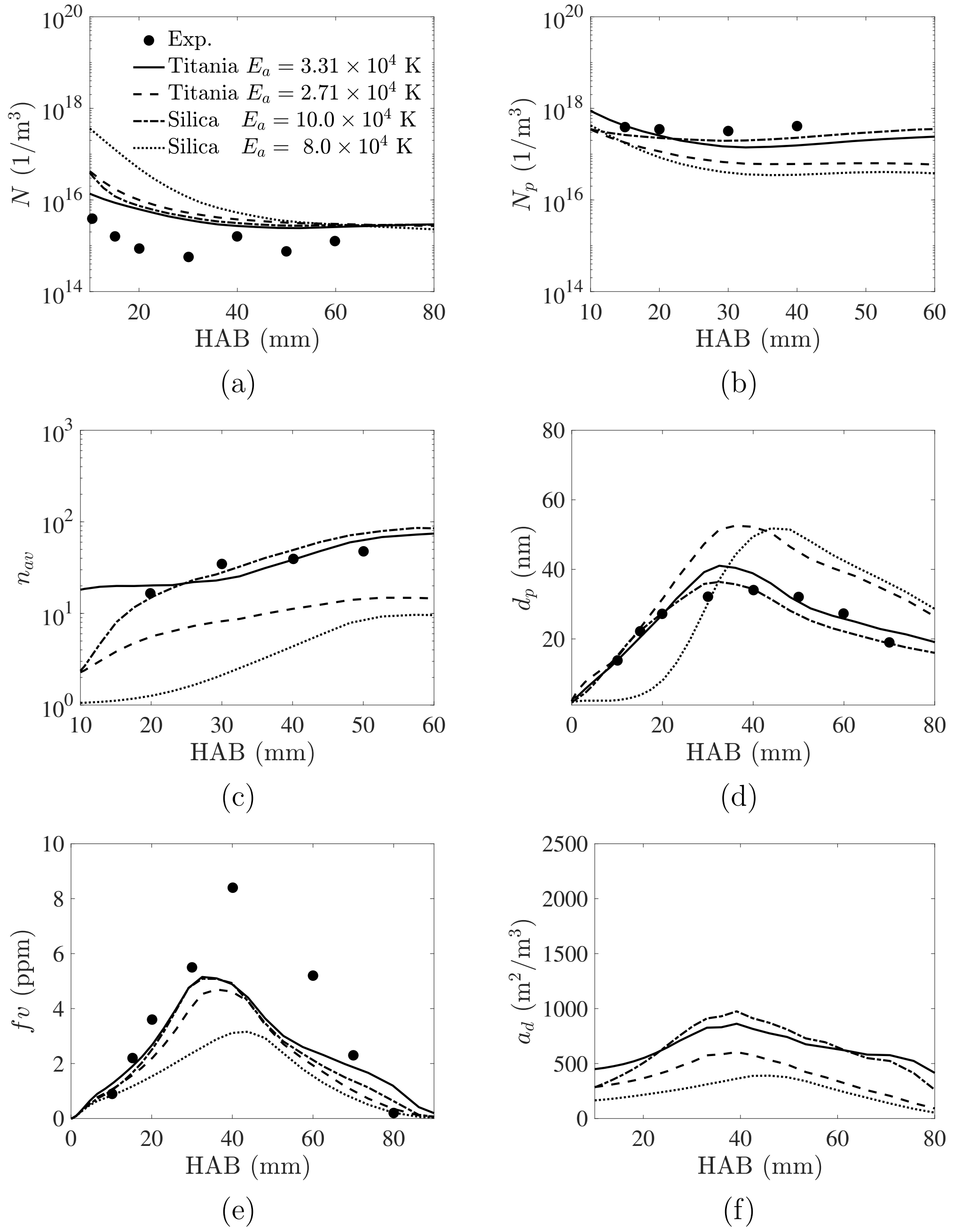

(a) (b)

(c) (d)

(e) (f)

Figure 4.11: Comparison of soot morphology along the annular pathline containing maximum soot volume fraction using different activation energies for CFV-2PBE with the silica and titania model. (a) Number density of aggregates, (b) number density of primary particles, (c) average number of primary particles per aggregate, (d) diameter of primary particles, (e) soot volume fraction, and (f) surface area density. Solid line: titania model with $E_a = 3.31 \times 10^4$ K; Dashed line: titania model with $E_a = 2.71 \times 10^4$ K; Dash-dot line: silica model with $d_c = 5$ nm, $E_a = 8.0 \times 10^4$ K; Dotted line: silica model with $d_c = 5$ nm, $E_a = 10.0 \times 10^4$ K.

4.3.4 Comparison of the one-PBE model with the two-PBE model without finite-rate fusing of primary particles

Finally, it is worth comparing the results of the CFV-1PBE with those of a CFV-2PBE formulation that does not involve finite-rate fusing of primary particles and employs the same critical diameter ($d_c = 30.8$ nm) as the CFV-1PBE model. This comparison exposes the influence of the inconsistent calculation of surface growth and oxidation in the one-PBE formulation, which (as discussed in Section 2.2.2) is due to the fact that the size of the primary particles is assumed to be frozen once they reach the cut-off size, ignoring the effect of surface processes. Fig. 4.12 shows the comparison of integrated soot volume fraction and temperature along the centreline, while Fig. 4.13 shows the comparison along the annular pathline containing maximum soot volume fraction for the average number of primary particles per aggregate and the diameter of primary particles. Small differences can be observed in both figures, and a similar trend is observed in other plots (not shown here). The impact of the inconsistent calculation of surface processes is therefore small, due to the fact that the effect of these processes on the particle properties beyond such a high cut-off point is small. Of course, the formulations without finite-rate fusing cannot account correctly for the trends in the morphology and PSD. However, the small error incurred by the one-PBE model indicates that this approach is a reasonable choice for simulations where predictions of such properties are not required, as is the case for many turbulent flame simulations.

4.4 Summary

To this point, a population balance approach was developed for modelling soot formation that distinguishes between coalescence and aggregation and incorporates finite-rate fusing of primary particles within aggregates, while providing a numerically accurate description of primary particle surface growth and oxidation within aggre-

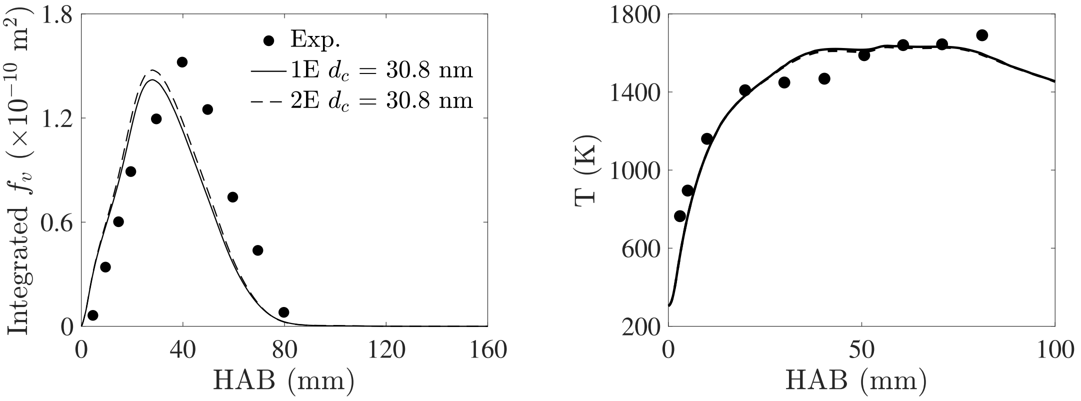

(a) Integrated soot volume fraction (b) Temperature

Figure 4.12: Comparison of numerical predictions by CFV-1PBE, CFV-2PBE without finite-rate fusing of primary particles and experimental data for (a) integrated soot volume fraction and (b) temperature along the centreline.

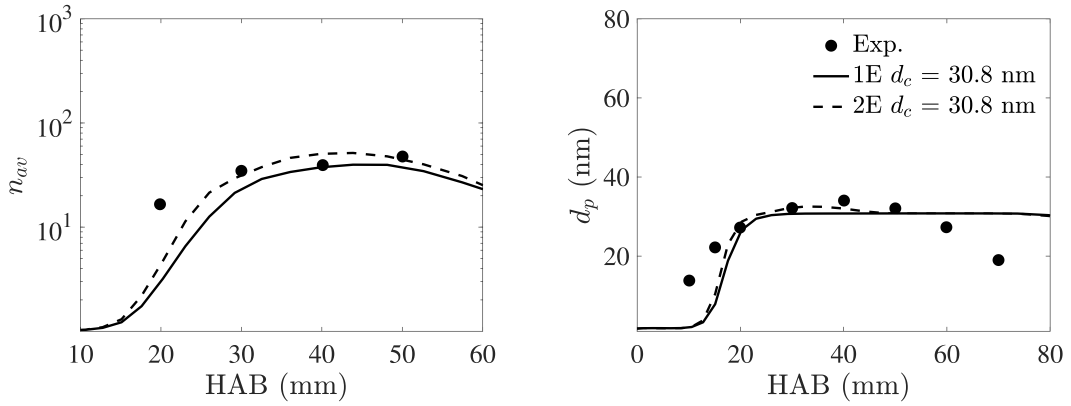

(a) n_{av} (b) d_p

Figure 4.13: Comparison of numerical predictions by CFV-1PBE, CFV-2PBE without finite-rate fusing of primary particles and experimental data for (a) average number of primary particles per aggregate and (b) primary particle diameter.

gates. The approach is based on the conservative finite volume PBE discretisation (CFV-1PBE) method [7], which was extended here to a two-population balance model (CFV-2PBE) comprising equations for the number density of primary particles and aggregates. The work also showed how the two-PBE approach could be coupled with CFD for the simulation of sooting flames.

One of the objectives for developing an accurate approach for population balance modelling is to prevent the compensation of errors between numerics and modelling. The conservative finite volume method attains accurate prediction of the distribution together with the conservation of the first moment (which is proportional to mass) in aggregation. The extension to the two-PBE approach ensures that growth is calculated in a consistent manner and avoids the unphysical assumption of a cut-off point required in the one-PBE approach.

The numerical method was first shown to reproduce the self-preserving property of aggregates with varying fractal dimension. Subsequently, the CFD-PBE framework was applied to the Santoro laminar non-premixed co-flow sooting flame, and the two-PBE approach was compared with the one-PBE approach. As the soot mass growth is dominated by surface growth, the surface reactivity in the HACA mechanism is critical for the soot volume fraction, and it was shown that, with a properly adjusted reactivity and cut-off point, the one-PBE method is able to give a reasonably good prediction of soot volume fraction. The two-PBE approach, however, attained this result with a consistent description of growth and a more physical model for the fusing of primary particles. Furthermore, the predictions of the PSD and of the morphological parameters by the two-PBE model differed considerably from those by the one-PBE model. The lack of information on the fusing timescale, however, necessitates the extrapolation of sintering models for other nanoparticles, such as silica and titania. Models for these two nanoparticles were implemented in the context of CFV-2PBE and tested, and significant improvement in the description of soot morphology could be attained with a careful adjustment in the sintering model parameters. However, it is clear that further research is warranted in this area in order to accomplish fully predictive simulations of soot aggregation. Furthermore, recent work by Goudeli et al. [190] has studied the variation of fractal dimension, and this effect could also be incorporated in future work.

One of the objectives of the analysis in this chapter is to lay the groundwork for the application of CFD-PBE coupling to turbulent flames, where the uncertainty involves several more factors, such as the turbulence-chemistry and turbulence-soot interaction. Given the fact that measurements in turbulent flames exist mainly for the soot volume fraction, the findings of this study demonstrate why the one-PBE approach has been used with relative success so far and is probably a reasonable choice. However, the parameter that must be adjusted in the one-PBE model (the cut-off point) is artificial and therefore, once experimental information on the fusing of soot primary particles becomes available, it should be possible to harvest the potential of the two-PBE approach towards attaining truly predictive simulations of soot formation in flames.

Chapter 5

Population balance modelling of soot formation in turbulent flames

The main objective of this chapter is to present the detailed formulation of a comprehensive approach for modelling soot formation in turbulent flames, and its associated solution method and implementational aspects. For the first time, I introduce coalescence and aggregation into the recently established LES-PBE-PDF approach [10, 11], thus developing a complete physicochemical model in which the PBE encompassing soot nucleation, surface reaction, aggregation and condensation is properly coupled with turbulent flow and chemical reactions, and the associated turbulence-chemistry-particle formation interactions are accounted for without severe closure assumptions.

This chapter is structured as follows: In Section 5.1, I briefly review the LES-PBE-PDF formalism. In Section 5.2, the closure for the micromixing term is presented, followed by the statistically equivalent stochastic field equations in Section 5.3. In the end, the solution algorithm and aspects of implementation is discussed.

5.1 LES-PBE-PDF formalism

In this section, I present first a general form of the conservation equations for a variable density flow under the framework of LES-PBE-PDF in view of an Eulerian formulation, and then I demonstrate the derivation of a transport equation for the joint scalar-number density PDF, in which the coupling between turbulence, chemistry and soot is properly accounted for and the chemical source terms and terms associated with homogeneous PBE appear in closed form.

5.1.1 Governing equations

The conservation equations for mass, momentum ($i = 1, 2, 3$ indicating three directions), $k = 1, ..., n_s$ reactive scalars (gaseous species and enthalpy) can be written in Cartesian coordinate as:

$$\frac{\partial \rho}{\partial t} + \frac{\partial \rho u_j}{\partial x_j} = 0 \tag{5.1}$$

$$\frac{\partial \rho u_i}{\partial t} + \frac{\partial \rho u_i u_j}{\partial x_j} = -\frac{\partial p}{\partial x_i} + \frac{\partial \tau_{ij}}{\partial x_j} + \rho g_i \tag{5.2}$$

$$\frac{\partial \rho Y_k}{\partial t} + \frac{\partial \rho u_j Y_k}{\partial x_j} = -\frac{\partial J_{kj}}{\partial x_j} + \rho \dot{\omega}_k(\mathbf{Y}, \mathbf{N}) \tag{5.3}$$

where τ_{ij}, g_i and $\dot{\omega}_k(\mathbf{Y}, \mathbf{N})$ represent the viscous stress tensor, the gravitational acceleration and the scalar production/destruction source term, respectively. Here, $\mathbf{Y} = (Y_1, \ldots, Y_{n_s})$ is the array of n_s reactive scalars, $\mathbf{N} = (N_1, \ldots, N_m)$ is the array of m PBE scalars, and J_{kj} denotes the diffusive flux of scalar k along direction j, following:

$$J_{kj}(\mathbf{x}, t) = -\rho(\mathbf{x}, t) D_m(\mathbf{Y}(\mathbf{x}, t)) \frac{\partial Y_k(\mathbf{x}, t)}{\partial x_j} \tag{5.4}$$

where $D_m(\mathbf{Y}(\mathbf{x}, t))$ denotes the kinematic diffusivity of any reactive scalar into the mixture. It can be related to the mixture kinematic viscosity μ, whose calculation is via a molecular Schmidt/Prandtl number $\mathrm{Sc} = 0.7$, $\rho D_m = \mu/\mathrm{Sc}$ [106]. It should be noted that in the argument list of $\dot{\omega}_k$, the dependency on the particle scalars $\mathbf{N}$ suggests that the scalar source terms are associated with particle dynamics. Typical examples would be the radioactive heat loss due to soot radiation and the species consumption due to soot formation. In turbulent reactive flow at low Mach numbers, the impact of pressure deviations from the ambient pressure on the density is relatively small. Thus, the carrier fluid can be treated as a multicomponent ideal gas, and its mixture density is often a function of the local reactive scalars:

$$\rho(\mathbf{x}, t) = \hat{\rho}(\mathbf{Y}(\mathbf{x}, t)) \tag{5.5}$$

For the soot particles within the carrier fluid, its population is described statistically via the number density $N(v, \mathbf{x}, t)$ per unit of mixture volume and per unit of length in particle volume space. As introduced in Section 2.3.4, the discretised population balance equation for the evolution of the number density N_i $(i = 1, \ldots, m)$ whose volume is located at section (v_{i-1}, v_i) in particle volume space can be written as:

$$\frac{\partial N_i}{\partial t} + \frac{\partial u_j N_i}{\partial x_j} = -\frac{\partial K_{ij}}{\partial x_j} + \dot{s}_i(v, \mathbf{Y}, \mathbf{N}) \tag{5.6}$$

where the thermophoretic velocity u_j^t in Eq. 2.40 is omitted in turbulent flame as a simplification, and K_{ij} denotes the diffusive flux of number density N_i along jth direction in physical space:

$$K_{ij}(v, \mathbf{x}, t) = -D_p(v, \mathbf{x}, t)\frac{\partial N_i}{\partial x_j} \tag{5.7}$$

Here, the source term $\dot{s}_i(v, \mathbf{Y}, \mathbf{N})$ encompasses all the terms describing particle evolution associated with section i in particle volume space due to nucleation, surface growth, oxidation, condensation and coagulation (coalescence and aggregation). Essentially, the source term $\dot{s}_i$ represents the particle evolution in a spatially homogeneous system:

$$\begin{aligned}\dot{s}_i(v, \mathbf{Y}, \mathbf{N}) = &-\frac{\partial(G(\mathbf{Y}, v)N)}{\partial v} + B(\mathbf{Y})\delta(v - v_0) + \dot{C}_i(\mathbf{Y}, \mathbf{N}) \\ &+ \frac{1}{2}\int_0^v \beta(w, v - w)N(w)N(v - w)dw - \int_0^\infty \beta(v, w)N(v)N(w)dw\end{aligned} \tag{5.8}$$

where the symbols G, B, β and $\dot{C}_i$ represent the cumulative particle growth rate, nucleation rate, collision frequency due to coagulation, and condensation source term, respectively. Their detailed functional forms depend on the soot kinetic model. In the following formulation, I employ a mass-based definition of the number density $N_\rho(v, \mathbf{x}, t)$ per unit of mixture mass, given as:

$$N_\rho(v, \mathbf{x}, t) = \frac{N(v, \mathbf{x}, t)}{\rho(\mathbf{x}, t)} \tag{5.9}$$

In the context of LES, the LES-filtered conservation equations for mass and momentum are given in Section. 2.4.3 (Eqs. 2.67 and 2.71). Applying the filtering operation to the transport equations of the reactive scalars and number densities would incur unclosed terms, whose existence poses the major modelling challenge in turbulent reactive flows. In the next section, I present the construction of the joint scalar-number density PDF for modelling the evolution of reactive scalars and the particle size distribution.

5.1.2 The joint scalar-number density PDF

As a start, this work follows the standard practice of first introducing the concept of one-point, one-time, Eulerian fine-grained PDF $g(\mathbf{y}, \mathbf{n}; \mathbf{x}, t)$ for the joint reactive scalars and particle number densities. Similar to the concept introduced in Section 2.6, $g(\mathbf{y}, \mathbf{n}; \mathbf{x}, t)$ is defined such that $g(\mathbf{y}, \mathbf{n})d\mathbf{y}d\mathbf{n}$ is the joint probability that at position $\mathbf{x}$ and time t, $y_k \leq Y_k(\mathbf{x}, t) \leq y_k + dy_k$ for all $k = 1, \ldots, n_s$, and $n_i \leq N_{\rho,i}(\mathbf{x}, t) \leq n_i + dn_i$ for all $i = 1, \ldots, m$, formulated as:

$$g(\mathbf{y}, \mathbf{n}; \mathbf{x}, t) = \prod_{k=1}^{n_s} \prod_{i=1}^{m} \delta(y_k - Y_k(\mathbf{x}, t)) \delta(n_i - N_{\rho,i}(\mathbf{x}, t)) = \delta(\mathbf{y} - \mathbf{Y}(\mathbf{x}, t)) \delta(\mathbf{n} - \mathbf{N}_\rho(\mathbf{x}, t)) \tag{5.10}$$

where y_k and n_i denote independent variables and represent the sample space of the dependent random variables Y_k and $N_{\rho,i}$, respectively; $\mathbf{Y}$ and $\mathbf{N}_\rho$ denote the set of Y_k for all $k = 1, \ldots, n_s$ and $N_{\rho,i}$ for all $i = 1, \ldots, m$, respectively.

The fine-grained PDF is useful in obtaining and manipulating PDF equations due to the following property [129]:

$$f(\mathbf{y},\mathbf{n};\mathbf{x},t)=\int_{\Omega}\delta(\mathbf{y}-\mathbf{Y}')\delta(\mathbf{n}-\mathbf{N}'_{\rho})f(\mathbf{Y}',\mathbf{N}'_{\rho};\mathbf{x},t)d\mathbf{Y}'d\mathbf{N}'_{\rho} \tag{5.11}$$

This concept was first pioneered by Lundgren [128] in the context of RANS and generalised to LES by Pope [129]. For my developments, the precise definition of the joint scalar-number density PDF in the context of LES is immaterial. It might be seen as a cell-averaged representation of a single realisation, such that its integral over a finite region of its sample space represents the likelihood of occurrence for an event within the local cell. Consequently, combining the filtering operation (Eq. 2.66), the joint scalar-number density PDF under the framework of LES can be formulated as:

$$\begin{aligned}f_{\mathbf{Y},\mathbf{N}_{\rho}}(\mathbf{y},\mathbf{n};\mathbf{x},t)=\overline{g(\mathbf{y},\mathbf{n};\mathbf{x},t)}&=\overline{\delta(\mathbf{y}-\mathbf{Y}(\mathbf{x},t))\delta(\mathbf{n}-\mathbf{N}_{\rho}(\mathbf{x},t))}\\&=\int_{\Omega}G(\mathbf{x}-\mathbf{x}')\delta(\mathbf{y}-\mathbf{Y}(\mathbf{x}',t))\delta(\mathbf{n}-\mathbf{N}_{\rho}(\mathbf{x}',t))d\mathbf{x}'\end{aligned} \tag{5.12}$$

With the positive definite filter G (see Eq. 2.63), it can be shown that $f_{\mathbf{Y},\mathbf{N}_{\rho}}(\mathbf{y},\mathbf{n};\mathbf{x},t)$ conserves the properties of a PDF. In particular, $f_{\mathbf{Y},\mathbf{N}_{\rho}}(\mathbf{y},\mathbf{n};\mathbf{x},t)$ represents the joint probability of $\mathbf{Y}=\mathbf{y}$ and $\mathbf{N}_{\rho}=\mathbf{n}$ arising within the filter volume. Subsequently, for any function $\omega(\mathbf{Y},\mathbf{N}_{\rho};\mathbf{x},t)$ depending on the scalar fields $\mathbf{Y}$ and $\mathbf{N}_{\rho}$, its LES-filtering operation $\bar{\cdot}$ results in:

$$\begin{aligned}\overline{\omega}(\mathbf{Y},\mathbf{N}_{\rho};\mathbf{x},t)&=\int_{\Omega}G(\mathbf{x}-\mathbf{x}')\omega(\mathbf{Y}(\mathbf{x}',t),\mathbf{N}_{\rho}(\mathbf{x}',t))d\mathbf{x}'\\&=\int_{-\infty}^{\infty}\left(\omega(\mathbf{y},\mathbf{n})d\mathbf{y}d\mathbf{n}\int_{\Omega}G(\mathbf{x}-\mathbf{x}')g(\mathbf{y},\mathbf{n};\mathbf{x}',t)d\mathbf{x}'\right)\\&=\int_{-\infty}^{\infty}\omega(\mathbf{y},\mathbf{n})f_{\mathbf{Y},\mathbf{N}_{\rho}}(\mathbf{y},\mathbf{n};\mathbf{x},t)d\mathbf{y}d\mathbf{n}\end{aligned} \tag{5.13}$$

It is obvious that once the joint scalar-number density PDF is known, the filtered source term as a function of the scalar fields $\mathbf{Y}$ and $\mathbf{N}_{\rho}$ is closed regardless of its functional form.

To facilitate the practical application, the joint PDF can be associated with the

LES-filtered density field. Here, I introduce, following Eq. 5.5 and Eq. 5.13, the LES-filtered density field $\overline{\rho}(\mathbf{x},t)$:

$$\overline{\rho}(\mathbf{x},t)=\overline{\rho(\mathbf{Y}(\mathbf{x},t))}=\int\hat{\rho}(\mathbf{y})f_{\mathbf{Y}}(\mathbf{y};\mathbf{x},t)d\mathbf{y} \tag{5.14}$$

where $f_{\mathbf{Y}}(\mathbf{y};\mathbf{x},t)$ represents the marginal filtered PDF associated with the reactive scalar fields within a single realization. Now, I can introduce the density weighted joint PDF $\widetilde{f}(\mathbf{y},\mathbf{n};\mathbf{x},t)$, which is analogous to Eq. 2.66 and is formulated as:

$$\overline{\rho}(\mathbf{x},t)\widetilde{f}_{\mathbf{Y},\mathbf{N}_\rho}(\mathbf{y},\mathbf{n};\mathbf{x},t)=\hat{\rho}(\mathbf{y})f_{\mathbf{Y},\mathbf{N}_\rho}(\mathbf{y},\mathbf{n};\mathbf{x},t) \tag{5.15}$$

5.1.3 Transport equation for the joint scalar-number density PDF

The transported PDF approach aims to solve directly a transport equation for the joint PDF in which the non-linear source terms appear in closed form. There are several methods for the derivation of the transport equation for PDF [129, 130, 132]. Here, the derivation process is presented briefly, in which I drop the arguments of the variables for conciseness.

Considering the material derivative of the density weighted fine-grained PDF ρg:

$$\frac{D\rho g}{Dt}=\frac{\partial\rho g}{\partial t}+\frac{\partial\rho g u_j}{\partial x_j} \tag{5.16}$$

where, applying the chain rule, the left-hand side can be written as:

$$\frac{D\rho g}{Dt}=\frac{\partial\rho g}{\partial\rho\mathbf{N}_\rho}\frac{D\rho\mathbf{N}_\rho}{Dt}+\frac{\partial\rho g}{\partial\rho\mathbf{Y}}\frac{D\rho\mathbf{Y}}{Dt}=\frac{\partial g}{\partial\mathbf{N}_\rho}\frac{D\mathbf{N}}{Dt}+\frac{\partial g}{\partial\mathbf{Y}}\frac{D\rho\mathbf{Y}}{Dt} \tag{5.17}$$

By introducing Eqs. 5.3 and 5.6, and the property of the delta function, Eq. 5.17 can be written as:

$$\frac{D\rho g}{Dt} = -\frac{\partial g}{\partial \mathbf{n}}\frac{D\mathbf{N}}{Dt} - \frac{\partial g}{\partial \mathbf{y}}\frac{D\rho \mathbf{Y}}{Dt} = -\sum_{k=1}^{n_s}\frac{\partial g}{\partial y_k}\left(\rho\dot{\omega}_k - \frac{\partial J_{kj}}{\partial x_j}\right) - \sum_{i=1}^{m}\frac{\partial g}{\partial n_i}\left(\dot{s}_i - \frac{\partial K_{ij}}{\partial x_j}\right) \tag{5.18}$$

Finally, applying Eq. 5.16 into Eq. 5.18, an exact evolution equation for the density weighted fine-grained PDF ρg can be derived:

$$\frac{\partial \rho g}{\partial t} + \frac{\partial \rho u_j g}{\partial x_j} = -\sum_{k=1}^{n_s}\frac{\partial}{\partial y_k}\left(g\rho\dot{\omega}_k - g\frac{\partial J_{kj}}{\partial x_j}\right) - \sum_{i=1}^{m}\frac{\partial}{\partial n_i}\left(g\dot{s}_i - g\frac{\partial K_{ij}}{\partial x_j}\right) \tag{5.19}$$

where the expression for source term $\dot{s}_i$ is the same as Eq. 5.8 but should be expressed in terms of N_ρ. For any function $\Psi(\mathbf{u}, p, \mathbf{Y}, \mathbf{N}_\rho, \partial\mathbf{Y}/\partial\mathbf{x}, ...)$, the following property of the fine-grained density g shall be reminded:

$$\overline{g\Psi\left(\mathbf{u}, p, \mathbf{Y}, \mathbf{N}_\rho, \frac{\partial \mathbf{Y}}{\partial \mathbf{x}}, ...\right)} = f_{\mathbf{Y},\mathbf{N}_\rho}\overline{\left(\Psi(\mathbf{u}, p, \mathbf{Y}, \mathbf{N}_\rho, \frac{\partial \mathbf{Y}}{\partial \mathbf{x}}, ...)\middle|\mathbf{y}, \mathbf{n}\right)} \tag{5.20}$$

where the vertical bar represents the conditional expectation of Ψ given that $\mathbf{Y} = \mathbf{y}$ and $\mathbf{N}_\rho = \mathbf{n}$. One may refer Appendix A in [10] for proof. Applying the LES-filtering operation to the convection term $\rho u_j g$ with some reformulations would lead to:

$$\overline{\rho u_j g} = \hat{\rho}(\mathbf{y})\overline{(u_j|\mathbf{y}, \mathbf{n})}f_{\mathbf{Y},\mathbf{N}_\rho} = \hat{\rho}(\mathbf{y})\widetilde{u}_j f_{\mathbf{Y},\mathbf{N}_\rho} - \hat{\rho}(\mathbf{y})\left(\widetilde{u}_j - \overline{(u_j|\mathbf{y}, \mathbf{n})}\right)f_{\mathbf{Y},\mathbf{N}_\rho} \tag{5.21}$$

where the density can be taken out of the expectation in the first step because it depends only on local reactive scalars. The turbulent transport term in the Eq. 5.21 is closed by adopting a gradient diffusion hypothesis [11]:

$$\hat{\rho}(\mathbf{y})\left(\widetilde{u}_j - \overline{(u_j|\mathbf{y}, \mathbf{n})}\right)f_{\mathbf{Y},\mathbf{N}_\rho} = \overline{\rho}(\mathbf{x}, t)\Gamma(\mathbf{x}, t)\frac{\partial \widetilde{f}_{\mathbf{Y},\mathbf{N}_\rho}}{\partial x_j} \tag{5.22}$$

Here, the scaled turbulent kinematic viscosity $\Gamma = \mu_{sgs}/(\overline{\rho}\mathrm{Sc})$ is modelled via the SGS turbulent viscosity computed by Eq. 2.70.

At this point, by applying the LES operator to Eq. 5.19 with the aid of Eqs. 2.67, 5.15, 5.20 and 5.22 and commutation properties, the following transport equation can be derived:

$$
\begin{aligned}
\overline{\rho}\frac{\partial \widetilde{f}}{\partial t} + \overline{\rho}\widetilde{u}_j\frac{\partial \widetilde{f}}{\partial x_j} = {} & \frac{\partial}{\partial x_j}\left(\overline{\rho}\Gamma\frac{\partial \widetilde{f}}{\partial x_j}\right) \\
& - \sum_{k=1}^{n_s}\frac{\partial}{\partial y_k}\left(\overline{\rho}\dot{\omega}_k(\mathbf{y},\mathbf{n})\widetilde{f} - \frac{\overline{\rho}\widetilde{f}}{\hat{\rho}(\mathbf{y})}\overline{\left(\frac{\partial J_{kj}}{\partial x_j}\middle|\mathbf{y},\mathbf{n}\right)}\right) \\
& - \sum_{i=1}^{m}\frac{\partial}{\partial n_i}\left(\frac{\overline{\rho}\widetilde{f}}{\hat{\rho}}\dot{s}_i(\mathbf{y},\mathbf{n}) - \frac{\overline{\rho}\widetilde{f}}{\hat{\rho}(\mathbf{y})}\overline{\left(\frac{\partial K_{ij}}{\partial x_j}\middle|\mathbf{y},\mathbf{n}\right)}\right)
\end{aligned}
\tag{5.23}
$$

where I omit the subscript symbols in the PDF $\widetilde{f}$ for brevity. In Eq. 5.23, the non-linear source terms $\dot{\omega}$ (Eq. 2.43) and $\dot{s}$ (Eq. 5.8) are in closed form due to Eq. 5.20, accounting for the interaction between turbulence, chemistry and soot and is the major benefit of employing the transported PDF approach. However, the molecular mixing or micromixing terms, $\overline{\left(\frac{\partial J_{kj}}{\partial x_j}\middle|\mathbf{y},\mathbf{n}\right)}$ and $\overline{\left(\frac{\partial K_{ij}}{\partial x_j}\middle|\mathbf{y},\mathbf{n}\right)}$, appear unclosed. These unclosed terms represent the molecular diffusion of the PDF in the sample space. In what follows, I present the micromixing model employed to close these terms.

5.2 Micromixing

There are two aspects of molecular diffusion to be considered: one is the process of mixing, which appears as transport in reactive scalar and number density space in the PDF; the other is spatial transport, which appears as gradient diffusion of the PDF in physical space. A number of proposals have been made for closing the micromixing terms [103,132]. In this work, the associated closure is achieved by an augmented IEM micromixing model proposed initially in Ref. [133] and taking into account for PBE in [10,11]:

$$
m_i = \begin{cases}
-\frac{1}{\hat{\rho}(\mathbf{y})}\overline{\left(\frac{\partial J_{ij}}{\partial x_j}\middle|\mathbf{y},\mathbf{n}\right)} = \left(\kappa(\mathbf{x},t)(\tilde{Y}_i - y_i) + \frac{1}{\overline{\rho}}\frac{\partial}{\partial x_j}\left(\overline{\rho}\tilde{D}_m\frac{\partial \tilde{Y}_i}{\partial x_j}\right)\right) & \text{for } i = 1,\dots,n_s \\
-\frac{1}{\hat{\rho}(\mathbf{y})}\overline{\left(\frac{\partial K_{ij}}{\partial x_j}\middle|\mathbf{y},\mathbf{n}\right)} = \left(\kappa(\mathbf{x},t)(\tilde{N}_{\rho,i} - n_i) + \frac{1}{\overline{\rho}}\frac{\partial}{\partial x_j}\left(\tilde{D}_{p,i}\frac{\partial \overline{\rho}\tilde{N}_{\rho,i}}{\partial x_j}\right)\right) & \text{otherwise}
\end{cases}
\tag{5.24}
$$

where $\kappa(\mathbf{x}, t)$ denotes a micromixing frequency common to all scalars:

$$\kappa(\mathbf{x}, t) = \frac{C_\kappa}{2} \frac{\Gamma(\mathbf{x}, t)}{\Delta^2} \tag{5.25}$$

where, as discussed in Section 2.5.3, the SGS mixing constant $C_\kappa = 2$, and Δ is the characteristic width defined in the context of LES. Formally, Eq. 5.24 provides the closure for the transport equation of the joint scalar-number density PDF (Eq. 5.23).

The IEM micromixing model of McDermott and Pope [133] accounts for the spatial transport of the PDF and consequently accounts for the spatial transport of all moments of the PDF. The decay of the SGS covariance can also be captured, as indicated in [133]. To guarantee the SGS covariance vanishes in the DNS limit, i.e., the micromixing frequency $\kappa(\mathbf{x}, t) \to \infty$ as the grid resolution approaches Kolmogorov scale, I introduce a scaling, which relates the turbulent viscosity to the molecular viscosity [191]:

$$\kappa^*(\mathbf{x}, t) = \kappa(\mathbf{x}, t) \frac{1 + \frac{\mu_{sgs}}{\mu}}{\frac{\mu_{sgs}}{\mu}} \tag{5.26}$$

This scaling ensures an increased micromixing frequency in regions where the flame is well resolved. It only becomes effective if the turbulent viscosity is small compared to the molecular viscosity. In high Reynolds number flows, where the flame is typically located in an unresolved region, the turbulent viscosity is large compared to the molecular viscosity, in which case the scaling would have no significant effect.

5.3 The stochastic field method

Due to the high dimensionality of Eq. 5.23, obtaining its solution via standard finite-difference or finite-volume solution methods is computationally intractable. Therefore, this work adopts the Monte Carlo method for the solution of the joint scalar-number density PDF. The primary goal is not to accurately compute $f(\mathbf{z}; \mathbf{x}, t)$ but rather to estimate expectations associated with $f(\mathbf{z}; \mathbf{x}, t)$, i.e., average values of scalars and number densities. Within the combustion community, different stochastic solution methods have been developed, such as the Lagrangian method of stochastic particles [129], the Eulerian method of stochastic particles [135], or the method of Eulerian stochastic fields [136–138]. The method in this work is based on the last class, the Eulerian stochastic fields method, in which a system of stochastic differential equations (SDE) statistically equivalent to the closed form of the transport equation of the joint PDF is derived. Specifically, an independent stochastic process $\theta(t; v, \mathbf{x})$ is constructed in a way such that its transition PDF $h(\mathbf{y}, \mathbf{n}, t|\, \mathbf{Y}_0, \mathbf{N}_{\rho,0}, t_0; \mathbf{x})$ evolves according to Eq.5.23. The transition PDF $h(\mathbf{y}, \mathbf{n}, t|\, \mathbf{Y}_0, \mathbf{N}_{\rho,0}, t_0; \mathbf{x})$ subject to the initial condition $\mathbf{Y}_0 = \mathbf{Y}(\mathbf{x}, t_0)$ and $\mathbf{N}_{\rho,0} = \mathbf{N}_\rho(\mathbf{x}, t_0)$ is defined as [129]:

$$h(\mathbf{y}, \mathbf{n}, t|\, \mathbf{Y}_0, \mathbf{N}_{\rho,0}, t_0; \mathbf{x}) = \delta(\mathbf{y} - \mathbf{Y}_0(\mathbf{x}))\delta(\mathbf{n} - \mathbf{N}_{\rho,0}(\mathbf{x})) \tag{5.27}$$

Since the initial conditions are known, the conditioning on the initial conditions can be dropped from the argument list of h for clarity and write $h = h(\mathbf{y}, \mathbf{n}, t; \mathbf{x})$. Since the total number of reactive scalars and number density scalars is $n_\phi = n_s + m$, the LES-filtered PDF, in a Monte Carlo solution method, is represented by an ensemble of n_f stochastic fields $\theta_k^n(t; v, \mathbf{x})$, such that:

$$\widetilde{f}_{\mathbf{Y},\mathbf{N}_\rho}(\mathbf{y}, \mathbf{n}; \mathbf{x}, t) \equiv h(\mathbf{y}, \mathbf{n}, t; \mathbf{x}) = h(\mathbf{z}, t; \mathbf{x}) = \frac{1}{n_f} \sum_{n=1}^{n_f} \prod_{k=1}^{n_\phi} \delta(z_k - \theta_k^n(t; v, \mathbf{x})) \tag{5.28}$$

where the vector $\mathbf{z}$ encompasses the reactive scalar samples and number density scalar samples. By design, the filtered values $\widetilde{Z}_k$ of scalars are obtained simply by averaging:

$$\widetilde{Z}_k(\mathbf{x}, t) = \int Z_k \widetilde{f}_{\mathbf{Z}}(\mathbf{z}; \mathbf{x}, t) d\mathbf{z} = \frac{1}{n_f} \sum_{n=1}^{n_f} \theta_k^n(t; v, \mathbf{x}) \tag{5.29}$$

It must be mentioned again that the LES-filtered PDF $\widetilde{f}$ is not computed directly, but rather its associated low order expectations are approximated. As such, an accurate computation can be achieved for the first moments, while the statistical error is accumulated on the higher-order moments [138]

The final system of SDEs is presented below, and the thorough derivation can be found in [10, 11]. Formally, the stochastic field equations are given by:

$$
\begin{aligned}
\overline{\rho}\frac{\partial \theta_i}{\partial t} + \overline{\rho}\widetilde{u}_j\frac{\partial \theta_i}{\partial x_j} =& \frac{\partial}{\partial x_j}\left(\overline{\rho}\Gamma\frac{\partial \theta_i}{\partial x_j}\right) - \overline{\rho}\sqrt{2\Gamma}\dot{W}_j(t)\frac{\partial \theta_i}{\partial x_j} \\
&+ \overline{\rho}\left(\dot{\omega}_i(\boldsymbol{\theta}, \mathbf{x}, v) + m_i(\boldsymbol{\theta}, \mathbf{x})\right)
\end{aligned} \tag{5.30}
$$

where reactive source term $\dot{\omega}_i$ and micromixing term $\dot{m}_i$ yield specific expressions associated with $\theta_{\mathbf{Y}}$ and $\theta_{\mathbf{N}_\rho}$, and $\dot{W}_j(t)$ denotes the time derivative of a three-dimensional Wiener process $\mathbf{W}(t)$ in jth direction. The stochastic field are differentiable in space but not in time. Thus, Eq. 5.30 is only valid holding in a time-integral sense:

$$
\begin{aligned}
\overline{\rho}d\theta_i = -\overline{\rho}\widetilde{u}_j\frac{\partial \theta_i}{\partial x_j}dt + \frac{\partial}{\partial x_j}\left(\overline{\rho}\Gamma\frac{\partial \theta_i}{\partial x_j}\right)dt - \overline{\rho}\sqrt{2\Gamma}\frac{\partial \theta_i}{\partial x_j}dW_j(t) \\
+ \overline{\rho}\left(\dot{\omega}_i(\boldsymbol{\theta}, \mathbf{x}, v) + m_i(\boldsymbol{\theta}, \mathbf{x})\right)dt
\end{aligned} \tag{5.31}
$$

where the stochastic integral with respect to $\mathbf{W}(t)$ is formulated in the Itô sense [192].

Commonly, the fractional time step method is employed as a numerical solution method for the evolution equations of the type of Eq. 5.30. While its introduction brings an approximation in time, it also offers the benefit that the numerical solution procedures can be tailored in terms of the physical characteristics of each fractional step. In my study, I employ a first-order accurate fractional time stepping [129]. The evolution of the stochastic process can be divided into three fractional steps, which are convection-diffusion, micromixing, and fluid reaction and PBE fractional steps respectively, written as:

$$
\overline{\rho}\frac{\partial \theta_i}{\partial t} + \left(\overline{\rho}\widetilde{u}_j + \overline{\rho}\sqrt{2\Gamma}\dot{W}_j(t)\right)\frac{\partial \theta_i}{\partial x_j} = \frac{\partial}{\partial x_j}\left(\overline{\rho}\Gamma\frac{\partial \theta_i}{\partial x_j}\right) \tag{5.32}
$$

for convection-diffusion fractional time step, and

$$
\overline{\rho}\frac{\partial \theta_i}{\partial t} = \begin{cases} \left(\overline{\rho}\kappa(\mathbf{x}, t)(\tilde{\theta}_i - \theta_i) + \frac{\partial}{\partial x_j}\left(\overline{\rho}\tilde{D}_m\frac{\partial \tilde{\theta}_i}{\partial x_j}\right)\right) & \text{for } i = 1, \ldots, n_s \\ \left(\overline{\rho}\kappa(\mathbf{x}, t)(\tilde{\theta}_i - \theta_i) + \frac{\partial}{\partial x_j}\left(\tilde{D}_{p,i}\frac{\partial \overline{\rho}\tilde{\theta}_i}{\partial x_j}\right)\right) & \text{otherwise} \end{cases} \tag{5.33}
$$

for micromixing fractional time step, and

$$\overline{\rho}\frac{\partial \theta_i}{\partial t} = \begin{cases} \overline{\rho}\dot{\omega}_i(\boldsymbol{\theta}, \mathbf{x}) & \text{for } i = 1, \ldots, n_s \\ \overline{\rho}\dot{s}_i(v, \boldsymbol{\theta}, \mathbf{x}) & \text{otherwise} \end{cases} \tag{5.34}$$

for the fluid reaction and PBE fractional time step. In particular, for $i = n_s + 1, \ldots, n_\phi$, the source term $\dot{s}_i$ in Eq. 5.34 represents the evolution of a homogeneous PBE shown in Eq. 5.8. The numerical implementation associated with each process is straightforward.

5.4 Solution algorithm and implementational aspects

The LES-PBE-PDF method with soot formation for simulating turbulent reacting flow was implemented in the in-house software LES-BOFFIN [110]. This parallel CFD code solves the three-dimensional incompressible Navier-Stokes equations on a structured mesh. For the coupled LES-filtered mass and momentum equations (Eqs. 2.67 and 2.68), a second-order accurate finite volume scheme on a staggered grid with the SIMPLE loop is adopted. For the reactive scalars, the transport equations for the stochastic fields (Eq. 5.30) are solved with a fractional step method as discussed in Section 5.3, in which the processes of convection/diffusion, micromixing and chemical reaction fractional step are solved in turn with a first-order approximation in time. Similarly, the stochastic field equation for the number density is decomposed into a convection/diffusion, micromixing and PBE fractional step. Moreover, I incorporate the CFV-1PBE method [7] (introduced in Chapter 3) in the PBE fractional step to account for the coalescence and aggregation without further introducing numerical errors. The detailed discretisation can be found in Section 3.3. Formally, the PBE is discretised into a series of fixed sections in the particle volume space, which is different from the previous adaptive grid application [11, 85]. The current CVF-1PBE method conserves the first moment during the coalescence and aggregation process and places no restriction on the grid. For efficiency, the volumetric dependence of the collision frequency kernels is tabulated only once in the beginning of the simulation, and the remaining part is updated at each time step, achieving a 50% CPU reduction for the computation of the coagulation terms with respect to the non-tabulated approach.

In the convection/diffusion fractional step, the convective terms are discretised via a TVD scheme based on van Leer's limiter; the spatial diffusion terms combine the diffusion due to turbulent transport and the diffusion due to the micromixing and are discretised by the central difference scheme. A second-order accurate Crank-Nicolson method is applied for the temporal integration of the deterministic terms, while an Euler-Maruyama scheme [192] is adopted for the stochastic terms. For chemical reaction fractional step, a first-order accurate implicit Euler method is used; The temporal integration of the PBE fractional step is achieved via an explicit Euler method as the PBE step is not stiff. To speed up the computation, the gas phase reaction fractional step is only carried out at cells whose temperature exceeds 800 K. Furthermore, the reaction mechanism is hard-coded to accelerate the solution process. Finally, a recently developed dynamic load balancing scheme [85] is applied to the reaction fractional step for better efficiency when running the code in massively parallel computing systems. Cumulatively, all these techniques achieved a reduction in the runtime of the reaction fractional step by approximately one order of magnitude.

Chapter 6

Application to the Sandia turbulent non-premixed sooting flame

Experimental measurements of turbulent sooting flames are of paramount importance for development and validation of accurate, predictive models of flames with soot. The International Sooting Flame Workshop (ISF) has identified certain target flames that are suitable for model development and validation, spanning a variety of flame types (e.g. jet flames, bluff-body flames and swirl flames) and fuels, and established an archive of the detailed data sets of these flames. In my work, the experimental data for the Sandia flame (ISF-5 target flame 2) is used to validate the LES-PBE-PDF approach, as the experimental dataset for this flame provides detailed information for a laboratory-scale turbulent burner with well-controlled boundary conditions and flow configurations [193]. So far, there have been several studies choosing this flame as the benchmark for model validation in the context of LES. Xuan and Blanquart [27] applied an FPV model and a PAH relaxation model to account for the unsteady evolution of PAH species with a bi-variate soot model [53,194], later the soot model was revisited again by Jain and Xuan [28] to study the effects of large aromatic precursors. The same soot model, but combined with a presumed PDF model for the soot-turbulence-chemistry interaction, was employed in the work of Yang et al. [156]. Rodrigues et al. [29] applied a PBE sectional method, in which the turbulence-chemistry interaction is accounted for by a Flamelet/Progress variable (FPV) model. Nevertheless, the current state of the art is still limited due to the complexity of the problem, with only qualitatively acceptable predictions.

In the present study, I choose the CFV-1PBE method to employ for several reasons: a) experimental dataset in turbulent flames contains only soot volume fraction information, thus the CFV-1PBE method is advantageous for its predictive capability regarding the prediction of soot volume fraction, b) CFV-1PBE method contains less PBE scalars and is computationally affordable, and c) the knowledge on the fusing of soot primary particles is not yet clear to fully utilise the CFV-2PBE approach. I adopt the same gaseous chemical kinetics and soot kinetic model tested in the laminar diffusion flame case (Chapter 4). The numerical setup for the PBE is the same as the one introduced in Section 4.3.1. As discussed in Chapter 4, the current model was shown to provide a good prediction in soot volume fraction in Santoro laminar diffusion flame with properly calibrated model parameters such as the cut-off point d_c and surface reactivity α. Thus the same model parameters are applied to conduct a comprehensive investigation. In particular, d_c is set to be 30.8 nm, and the surface reactivity is set to be $\alpha = 0.0037 \times e^{9000/T}$. Moreover, to achieve a better agreement with experimental measurements regarding the axial profile of soot volume fraction, an additional simulation with an enhanced surface reactivity ($\alpha = 0.0074 \times e^{9000/T}$) is also conducted.

In the following sections, I present the flame configuration and numerics first, followed by a comprehensive investigation of the soot formation. My findings are summarised in the end.

6.1 Flame configuration and numerical set-up

A brief description of the flame configuration is presented in this section, together with the numerical configuration employed in the simulation. The flame has a central fuel jet surrounded by two concentric tubes of pilot flame and air. The fuel jet has an inner diameter (ID) of 3.2 mm and an outer diameter (OD) of 4.6 mm, and it is encircled by the pilot of ID 15.2 mm and OD 19.1 mm. Ethylene at room temperature 295 K is injected with bulk velocity $V_{fuel} = 54.7$ m/s in the central nozzle, resulting in a Reynolds number of 20,000. The pilot consists of premixed ethylene and air at an equivalence ratio of 0.9 and the flow rate of the pilot mixture is adjusted such that the heat release corresponds to 2% of that of the fuel jet. An adiabatic flame temperature of 2127 K is imposed for the corresponding equivalence ratio. The pilot is surrounded by a co-flow of air at 295 K and a uniform velocity $V_{air} = 0.6$ m/s. The experiment is conducted under an atmospheric pressure.

The computational domain is a rectangular parallelepiped, spanning 900 mm in the axial x-direction and 300 mm in the y and z directions, having 240, 80 and 80 cells respectively. The grid is stretched by a factor 1.013 axially, resulting in higher resolution near the burner. Radially, ten cells are allocated in the central region to resolve the fuel jet with a resolution of 0.3 mm, while the grid is stretched by a factor of 1.12 from the pilot towards the lateral boundaries. The mean axial velocities at the inflow for the fuel, jet and pilot are set to power-law profiles with exponents 1/6 and 1/2, respectively. On the contrary, the air co-flow is set to a constant mean axial inflow velocity. The turbulence intensities for all flows are set to 6%. The RMS inflow velocity for the fuel jet varies quadratically (at the jet rim, it is four times as large as the nominal centreline value), and becomes constant for the pilot and co-flow. The initial composition of the pilot is the adiabatic equilibrium condition for the premixed mixture. The four lateral boundaries are set to have the same composition and velocity as the co-flow air. At the domain exit, the convective outflow condition is applied to the velocity field, and the zero gradient condition is applied to the scalar fields. A schematic illustration of the computational domain is given in Fig. 6.1:

Previous applications of stochastic fields [10, 11, 106] have shown that eight fields are sufficient to account for the effect of SGS fluctuations. Unfortunately, no velocity measurements are available in the experiment. Since no validation can be made for the velocity field, I adopt a simplified inflow geometry, in which the thin wall of the tube

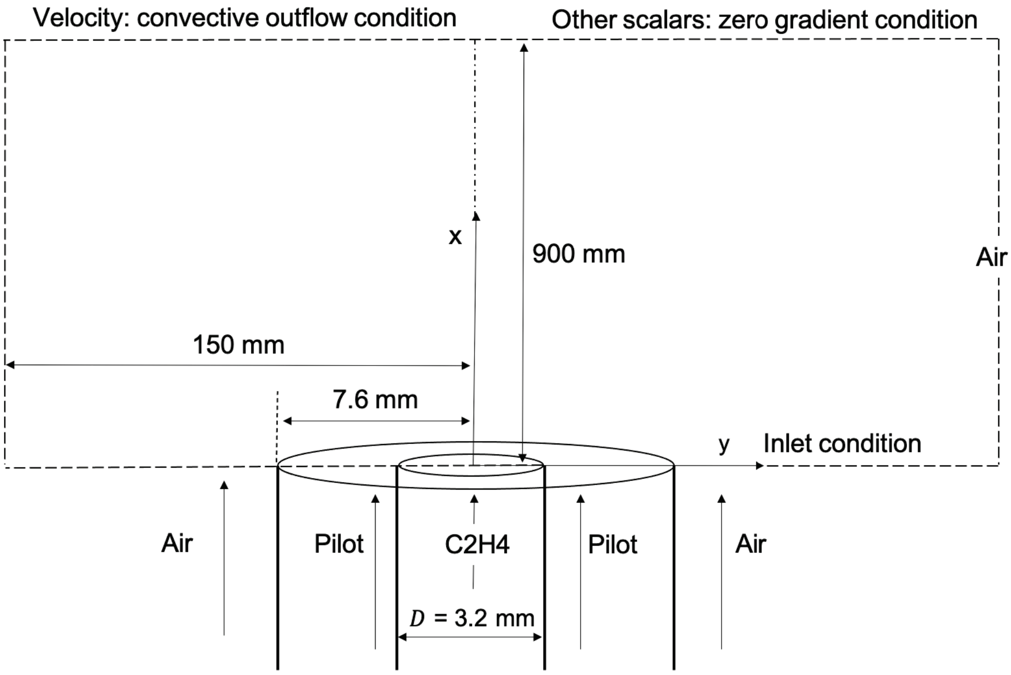

Figure 6.1: Illustration of the burner and computational domain.

and the jet immersion are ignored. A similar configuration was used by Sewerin and Rigopoulos [11], where good agreements for both mean and RMS velocity profiles were achieved for the Delft III turbulent flame. Once the simulation reached a statistically steady state, the temporal statistics were collected after a further period of 0.15 s (time step $\Delta t = 3 \times 10^{-6}$ s), corresponding to about three flow-through times, which is adequate for the temporal statistics of the scalars to become time-invariant.

6.2 Results and discussion

6.2.1 Comparison with experiment data

In order to validate the LES-PBE-PDF approach, the numerical results are compared first to the available experimental data, which are summarised below:

- CARS temperature and $X_{\mathrm{O}_2}/X_{\mathrm{N}_2}$ measurements [195]
- PLIF OH and PLIF PAH measurements [196]
- Axial profile of soot intermittency measurement [196]

- LII soot volume fraction measurements [197]

Fig. 6.2 shows a comparison of radial mean and RMS temperature profiles with experiments at $x/D = 134$ and $x/D = 175$ [195], while Fig. 6.3 shows a comparison of radial mean and RMS X_{O_2}/X_{N_2} profiles with experiment data at the same heights. Overall, the predictions are quite good for both mean and RMS values. At $x/D = 134$, an overestimation of the mean temperature around the centreline is observed (Fig. 6.2a) and the mean mole fraction ratio X_{O_2}/X_{N_2} (Fig. 6.3a) is slightly underpredicted, while the peaks of the RMS temperature (Fig. 6.2c) and RMS X_{O_2}/X_{N_2} (Fig. 6.3c) radial profiles from the simulation are in very good agreement with the experimental data. A similar level of discrepancy was also featured in the simulation of the same flame by Rodrigues et al. [29]. At $x/D = 175$, an overestimation of the mean temperature profile at the centreline (Fig. 6.2b) is also observed and the mean X_{O_2}/X_{N_2} profile (Fig. 6.3b) is slightly overpredicted. However, the shape of the flame tip is well reproduced and the RMS tempereture (Fig. 6.2d) and X_{O_2}/X_{N_2} (Fig. 6.3d) radial profiles are in good agreement with the experimental data. Possible causes for the overprediction of temperature include the underprediction of soot volume fraction, which will be discussed below (Fig. 6.7), as well as the deficiencies of the radiation model.

Fig. 6.4 shows a comparison of simulation results results and measurements for the mean OH radial profiles at different heights. As the experimental measurements are PLIF signals rather than mole fractions, numerical and experimental results are normalised by their corresponding maximum values for each height. Good agreement is observed, apart from some small discrepancies at $x/D = 117.2$ and $x/D = 132.8$. This result indicates a satisfactory prediction of the mean flame shape. Moreover, Fig. 6.5 shows a comparison of mean PAH radial profiles at different heights between numerical results and experimental measurements [196]. Note that $C_{10}H_8$ (A_2) is chosen as the representative PAH species in the numerical results, as its mass fraction is dominant compared to that of other PAHs contributing to soot nucleation. Despite a wider PAH profile at the lower region of the flame, as indicated in Fig. 6.5, the overall agreement

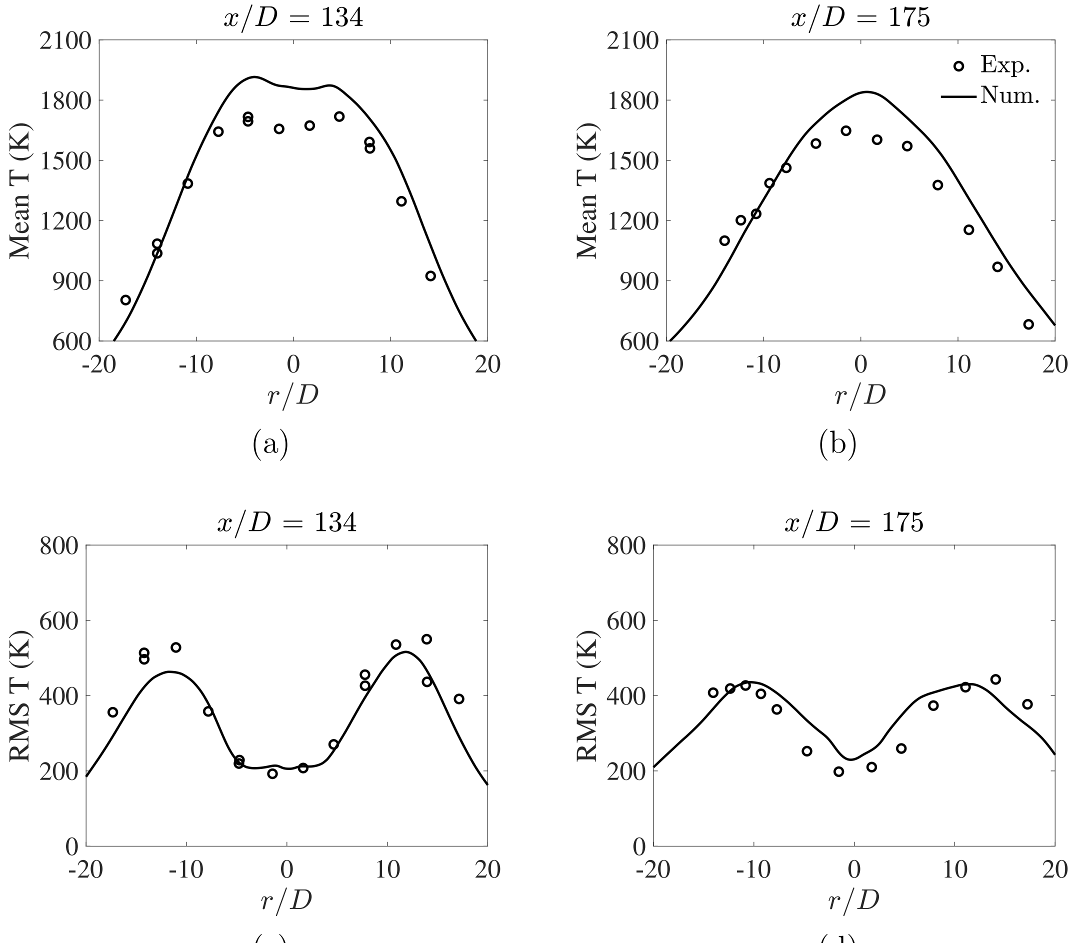

(a) (b)

(c) (d)

Figure 6.2: Comparison of mean and RMS temperature radial profiles between experimental data (symbols) and numerical results (line) at $x/D = 134$ and $x/D = 175$.

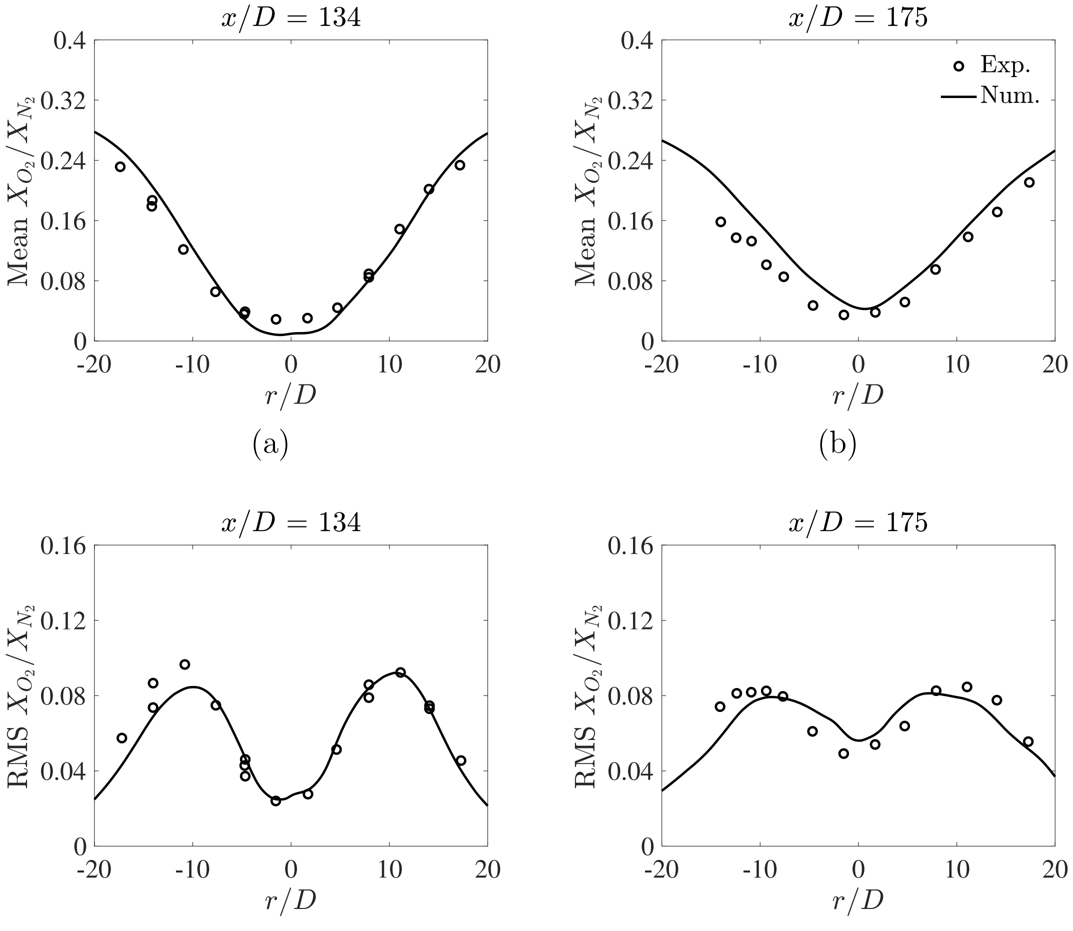

(a) (b)

(c) (d)

Figure 6.3: Comparison of mean and RMS X_{O_2}/X_{N_2} radial profiles between experiment data (symbol) and numerical results (line) at $x/D = 134$ and $x/D = 175$.

is also satisfactory. Good matches in both Fig. 6.4 and Fig. 6.5 are required for a proper account of soot oxidation, nucleation and condensation.

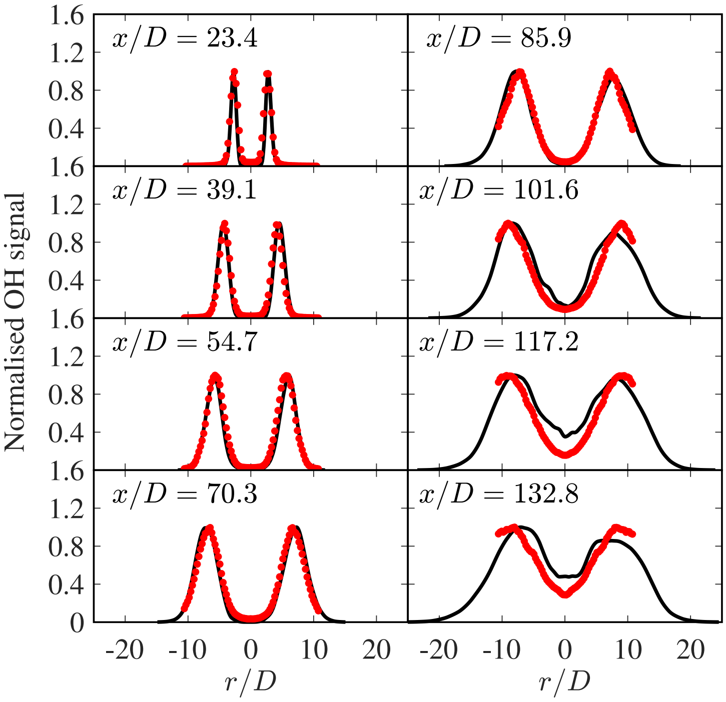

Figure 6.4: Radial profiles of normalised mean OH mass fraction from simulations (black line) and normalised OH signals from experimental data (red symbols).

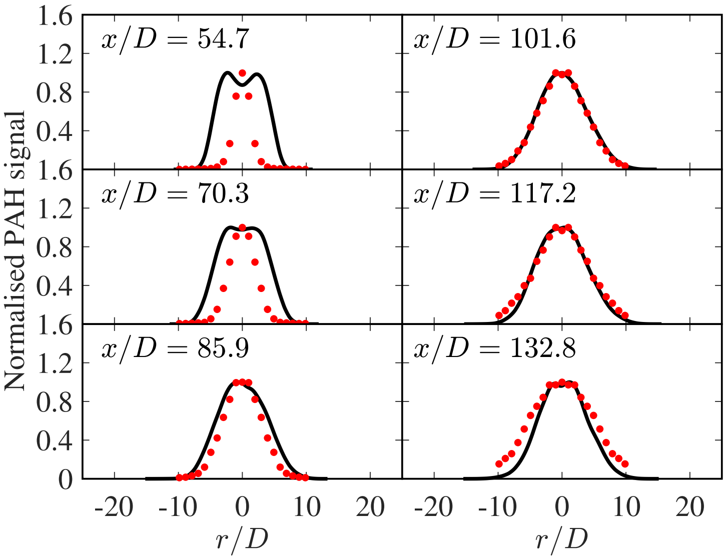

Figure 6.5: Radial profiles of normalised mean A_2 mass fraction from simulations (black line) and normalised PAH signals from experimental data (red symbols).

The axial profiles of mean and RMS soot volume fraction along the centreline are shown in Fig. 6.6. It is evident that, while the location of the soot formation zone and the qualitative features are reproduced, the magnitude is considerably underpredicted when using the same surface reactivity factor that was employed in the Santoro laminar flame simulations (i.e. $\alpha = 0.0037 \times e^{9000/T}$). Therefore, a simulation with enhanced reactivity (twice the pre-exponential factor, $\alpha = 0.0074 \times e^{9000/T}$) has also been conducted. Even in the case with the unaltered surface reactivity, while the peak mean and RMS soot volume fraction are underpredicted, the location and peak position of the predicted profiles are close to the experimental ones. It must be stressed that, in this case, all kinetics are exactly the same as in my simulation of the Santoro flame. In the literature, an overestimation of soot volume fraction by a factor of 2 [29] for this flame can be found, whereas a level of underprediction similar to my work was also observed in several studies [27,28]. In particular, several cases were conducted in Ref. [156] with different mixture fraction parameters associated with the conditional soot subfilter PDF model, and in some of these cases an underprediction by an order of magnitude were obtained, while in one case an overprediction by a factor of 3 was observed. The higher reactivity yields results close to the experimental values for the mean soot volume fraction, though the RMS is still underpredicted. An interesting finding is that the peak position of the predicted profiles is the same in both simulation cases. Since the surface reactivity alters the rate of surface growth and oxidation process, the α in the HACA mechanism is vital for obtaining quantitative agreement between simulation results and experimental data, while the onset of nucleation is responsible for the peak position of the soot volume fraction profile. Furthermore, due to higher amount of soot produced, the radiative heat loss is greater in the case with the enhanced surface reactivity, leading to lower temperature profiles at $x/D = 134$ and $x/D = 175$ (Fig. 6.7), which are closer to the experimental values.

Furthermore, Fig. 6.8 compares radial profiles of mean soot volume fraction at different heights. The location and qualitative trends in the experimental data are reproduced, but the magnitude of soot volume fraction in the region away from the jet is underpredicted for the case of the unaltered reactivity. Moreover, Fig. 6.9 compares the RMS radial profiles of soot volume fraction for the same heights, and similar features as for the means are observed. The good predictions of the position and the shape of the profiles indicate that several elements of the model, particularly related to the flow and turbulence-chemistry soot interaction, are performing well, but a quantitative agreement is still not possible, and the major source of the discrepancies lies in the kinetics and in particular the modelling of surface reactivity.

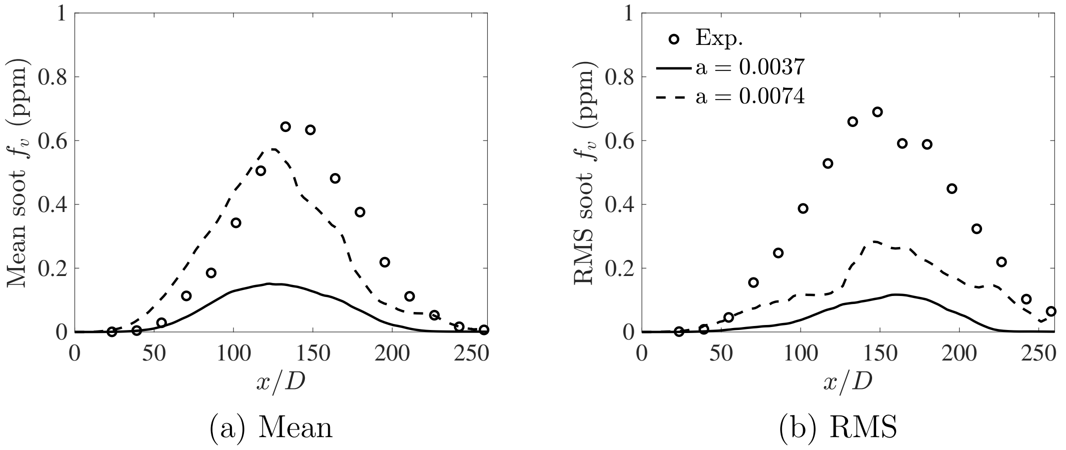

(a) Mean (b) RMS

Figure 6.6: Axial profiles of the mean and RMS soot volume fraction along the flame centreline. The solid line indicates the case of the same kinetics as in the laminar flame, while the dashed line indicates the case of enhanced reactivity.

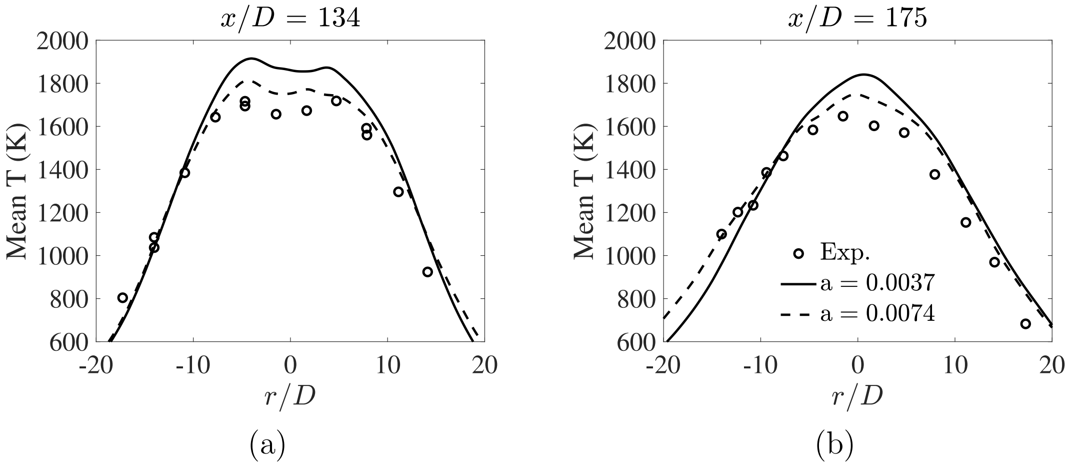

(a) (b)

Figure 6.7: Predictions of the mean temperature radial profiles at $x/D = 134$ and $x/D = 175$. The solid line indicates the case of the same kinetics as in the laminar flame, while the dashed line indicates the case of enhanced reactivity.

In addition, Fig. 6.10 shows a comparison of predicted and measured soot intermittency along the flame centreline. The resolved soot intermittency at each spatial position is defined experimentally as the probability of observing an instantaneous

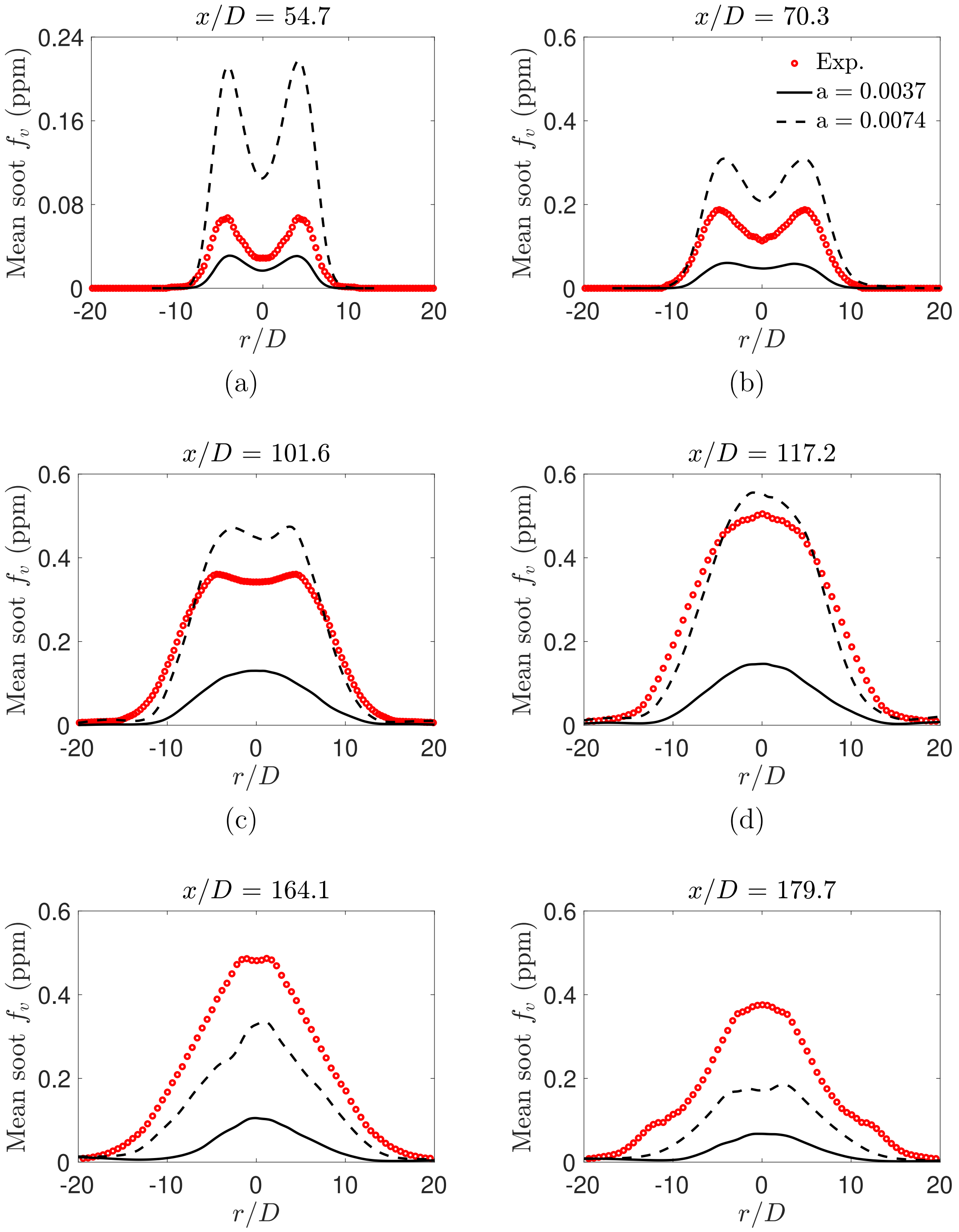

(a) (b)

(c) (d)

(e) (f)

Figure 6.8: Predictions of the mean soot volume fraction radial profiles at different heights. The solid line indicates the case of the same kinetics as in the laminar flame, while the dashed line indicates the case of enhanced reactivity.

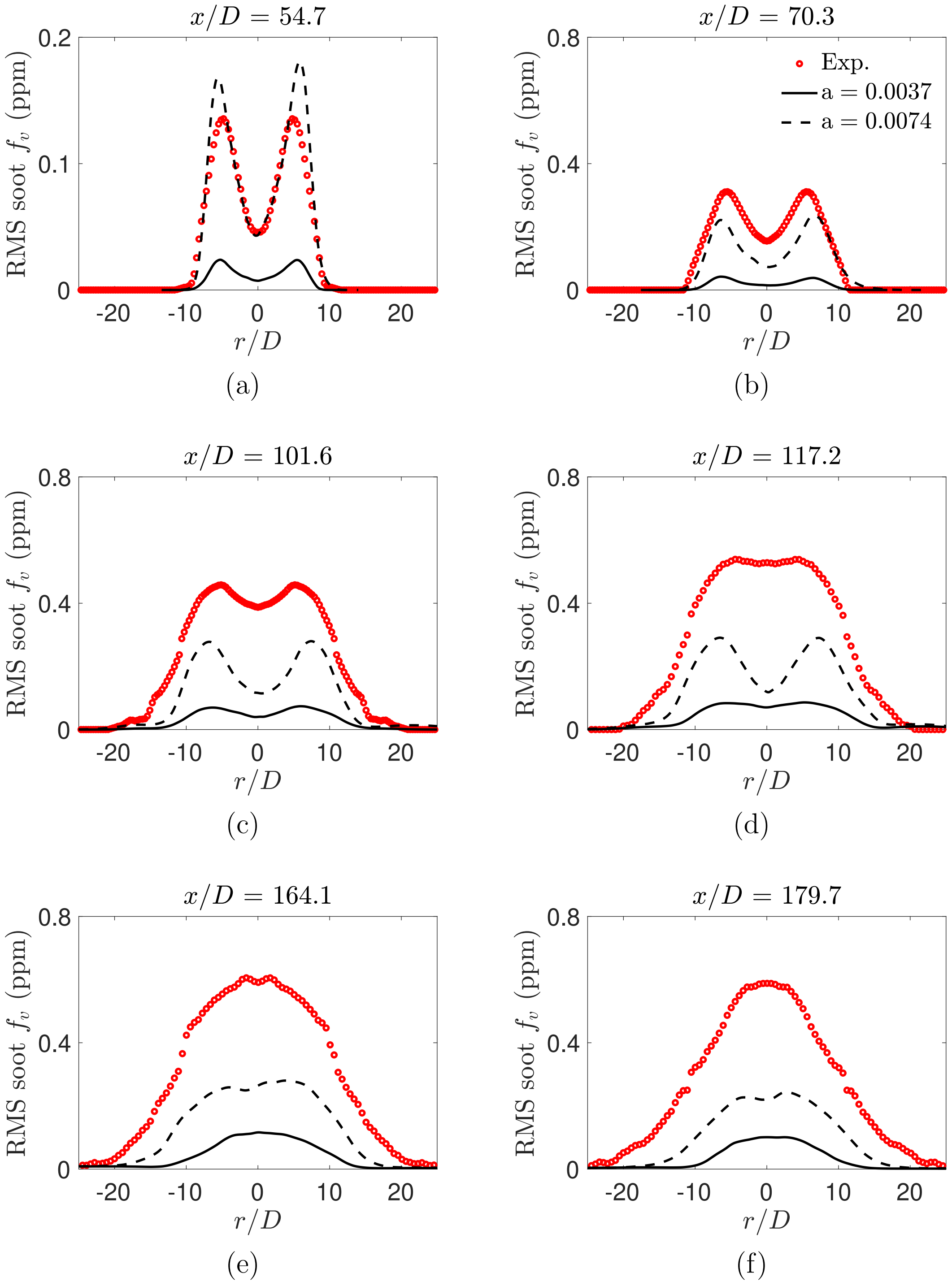

(a) (b)

(c) (d)

(e) (f)

Figure 6.9: Predictions of the RMS soot volume fraction radial profiles at different heights. The solid line indicates the case of the same kinetics as in the laminar flame, while the dashed line indicates the case of enhanced reactivity.

value of soot volume fraction lower than 0.03 ppm [196]. For the case with the unaltered surface reactivitty, the simulation results seem to be translated upstream with an underestimation in the region between $x/D = 60$ and $x/D = 130$. The current results indicate a stronger soot growth phenomenon in the middle region of the flame than was observed experimentally, which is further confirmed by the case of the enhanced surface reactivity, where a wider and lower soot intermittency profile is observed. Further investigation into the nature of these discrepancies and their relation to the kinetics is warranted.

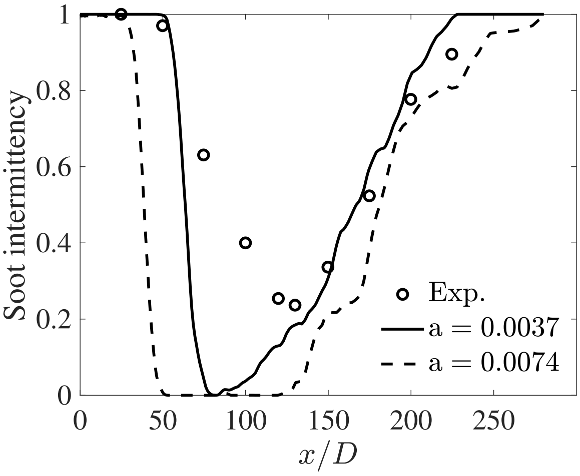

Figure 6.10: Comparison of numerical and experimental results for the axial soot intermittency profile along the flame centreline. The solid line indicates the case of the same kinetics as in the laminar flame, while the dashed line indicates the case of enhanced reactivity.

In summary, despite some discrepancies in the simulation compared to the experiment, the overall performance of the proposed LES-PBE-PDF approach is reasonably good in light of the current state of the art in the modelling of turbulent sooting flames. The soot reactivity in HACA growth seems to be one of the main uncertainties in the prediction of soot volume fraction, as the main soot mass addition is through surface growth (as will be confirmed later in the discussion of Fig. 6.14). However, it is notable that the qualitative trend and the location of the sooting zone can be predicted correctly with the Santoro flame kinetics. Further analysis of the soot formation mechanisms is presented in the next section.

6.2.2 Investigation of soot formation

In this section, the soot formation processes are analysed based on the results for the same kinetics as in the laminar flame ($d_c = 30.8$ nm, $\alpha = 0.0037 \times e^{9000/T}$), except for the results shown in Fig. 6.15. Fig. 6.11 shows contour plots of the instantaneous temperature, soot volume fraction and soot number density. An iso-contour of stoichiometric mixture fraction ($Z = 0.0634$) indicating the flame front is also presented with a solid line. As indicated in Fig. 6.11b,c, soot is restricted to fuel-rich regions within the mixture fraction iso-contour. Most soot particles are located in the region between $x/D = 40$ and $x/D = 100$, while the soot volume fraction peaks at a region between $x/D = 80$ and $x/D = 160$, consistent with the prediction in Fig. 6.6 and experimental observation [196]. Similar patterns were observed also in other simulations [27,29]. The distinct separation of the peak zones in these two plots indicates that soot would experience a strong mass addition after being formed, which is confirmed below (Fig. 6.12c).

To further analyse the soot formation phenomena associated with N and f_v fields, Fig. 6.12 shows the instantaneous and mean soot volume fraction contribution rates from nucleation, condensation, surface growth and oxidation. Note that only the oxidation rate due to OH is presented, as it is much larger than the one due to O_2 (as shown in Fig. 6.14, to be discussed later). The instantaneous and mean contour plots of mole fraction of several key species are presented in Fig. 6.13. Regarding PAHs, only the contour plot of A_2 mole fraction is shown, because the concentration of A_2 is orders of magnitude larger than that of other PAHs contributing to dimer formation. Firstly, by comparing Fig. 6.13a with Fig. 6.11c, it is clear that A_2 is formed before the measurable soot in the flame and is limited to the inner jet, consistent with the experimental observation in Ref. [196]. Fig. 6.12a, b and Fig. 6.13a show a strong spatial correlation between nucleation, condensation and A_2 species. This feature is expected, as the nucleation and condensation depend on the dimer concentration, which is associated with the concentration of A_2. Fig. 6.12a also confirms the early

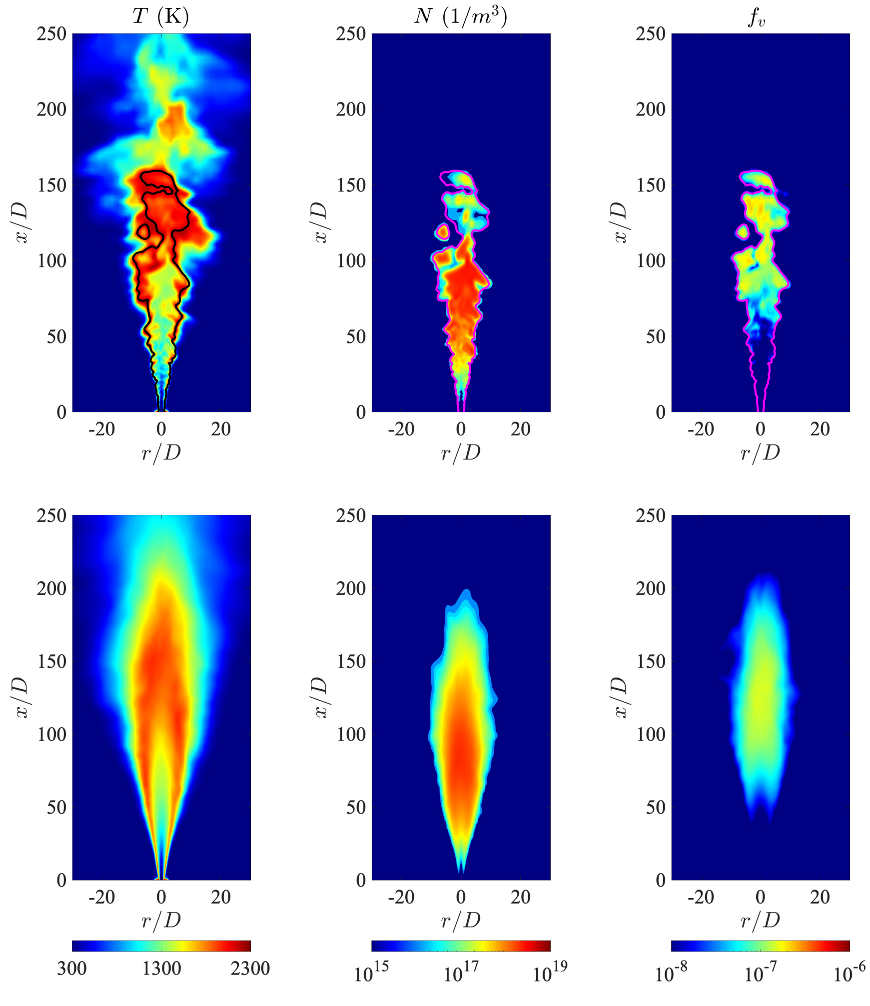

(a) (b) (c)

Figure 6.11: Contour plots of instantaneous (top) and mean (bottom) (a) temperature, (b) soot volume fraction and (c) soot number density computed from the LES-PBE-PDF model. The iso-contour of stoichiometric mixture fraction (indicating the flame front) is shown in solid line in the instantaneous contour plot (black in (a) and magenta in (b) and (c)).

nucleation indicated by Fig. 6.11b. By comparing Fig. 6.12a,b with c, it can be seen that surface growth is responsible for most of the mass addition, as its contribution rate is one order of magnitude larger than that of condensation. According to Ref. [196], the structure of OH should develop from straight, thin layers at the jet exit to increasingly wrinkled, thick structures downstream from the nozzle, which is well reproduced in Fig. 6.13c. A weak spatial correlation between growth rate and C_2H_2 is observed. As discussed in Chapter 4.3.1, this is because the rate-limiting reactions in the current soot kinetics are the hydrogen abstraction reactions, which means that radical species (e.g., H and OH) contribute more to surface growth than C_2H_2. In the regions that are rich in OH and H, C_2H_2 is consumed via the acetylene addition reaction step in HACA mechanism, which can be observed in Fig. 6.13b,c and d. These observations are consistent with those reported in Ref. [29] on a simulation of the same flame.

Fig. 6.14 shows the mean rate of change for each soot formation process along the centreline by the LES-PBE-PDF method. Similar to the observation in Fig. 6.12, a spatial correlation between the mean nucleation and condensation can be found, and the mass addition along the centreline is dominated by the surface growth process. As the oxidation due to OH is one order of magnitude larger than the one due to O_2, the prediction of the soot volume fraction along the centreline is dominated by surface growth and OH oxidation. The main uncertainty associated with these two processes is, as discussed before, the surface reactivity.

Fig. 6.15 shows the instantaneous normalised soot volume distribution along the flame centreline for the two different values of surface reactivity investigated. Note that the soot volume in each volume section is normalised by the total soot volume fraction at the corresponding spatial location. With enhanced surface reactivity, the majority of soot volume shifted towards the larger end in the size space (as expected). For the case of a small α (Fig. 6.15a), soot nucleation dominates in the regions near the jet nozzle, leading to spikes at the small particle size sections (around 1 nm) in these regions. For the case of a large α, however, a rather flat curve at the small particle size sections, even in the region very close to the jet, is observed in Fig. 6.15b,

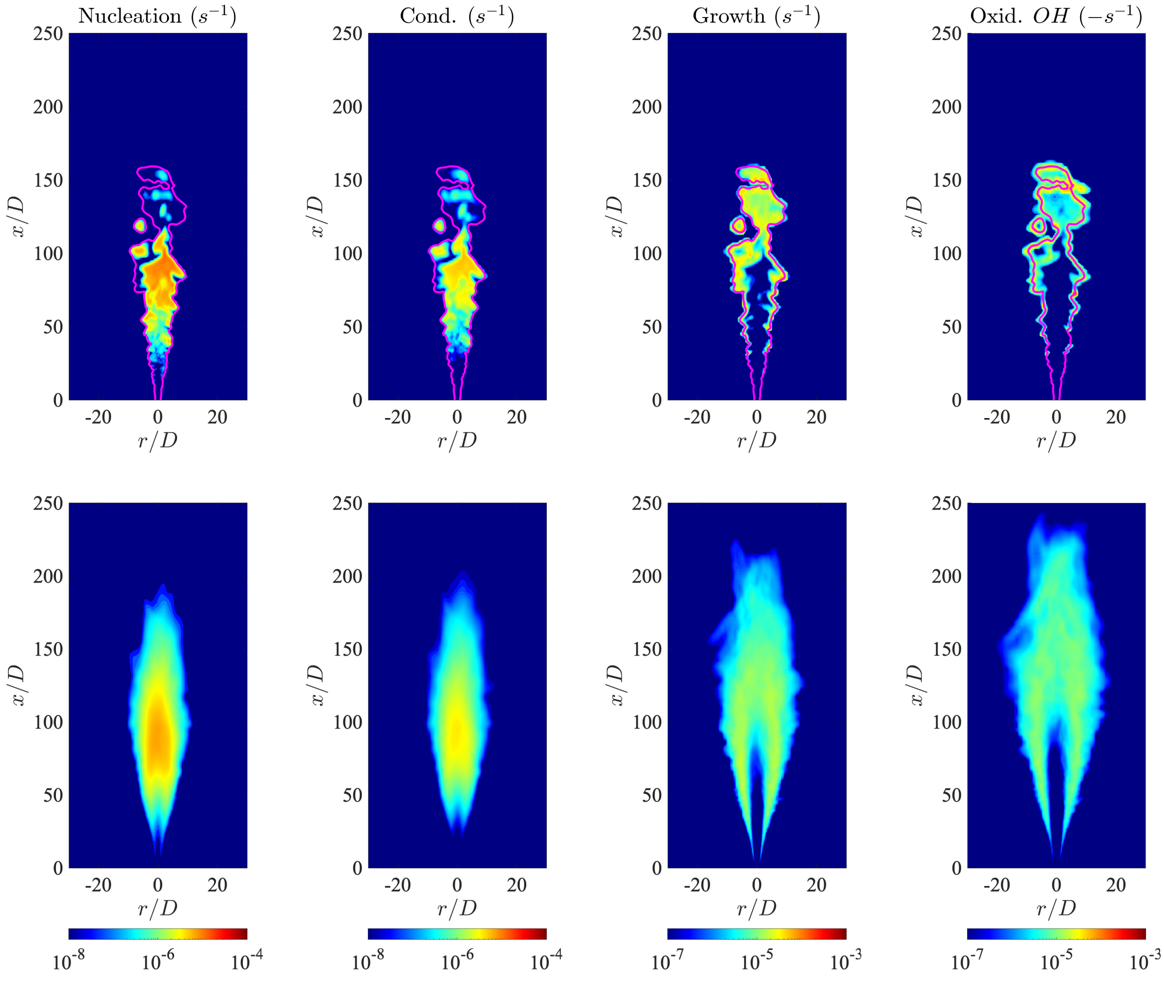

(a) (b) (c) (d)

Figure 6.12: Contour plots of the instantaneous (top) and mean (bottom) (a) nucleation rate, (b) condensation rate, (c) growth rate, and (d) oxidation rate due to OH computed from the LES-PBE-PDF model. The iso-contour of stoichiometric mixture fraction is shown in solid magenta line in the instantaneous contour plot.

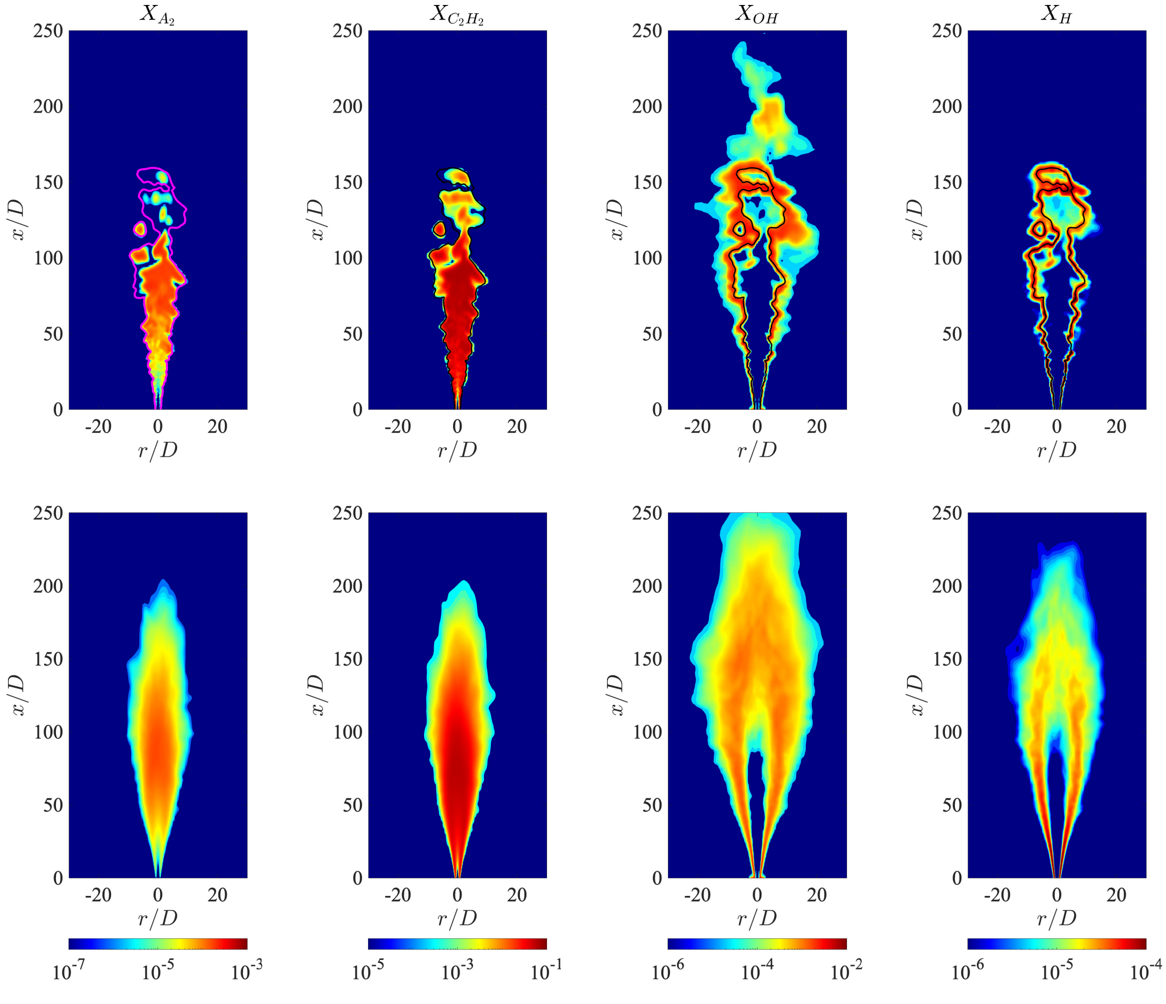

(a) (b) (c) (d)

Figure 6.13: Contour plots of the instantaneous (top) and mean (bottom) (a) A_2 mole fraction, (b) C_2H_2 mole fraction, (c) OH mole fraction and (d) H mole fraction computed from the LES-PBE-PDF model. The iso-contour of stoichiometric mixture fraction is shown in solid line in the instantaneous contour plot (magenta in (a), and magenta in the rest plots).

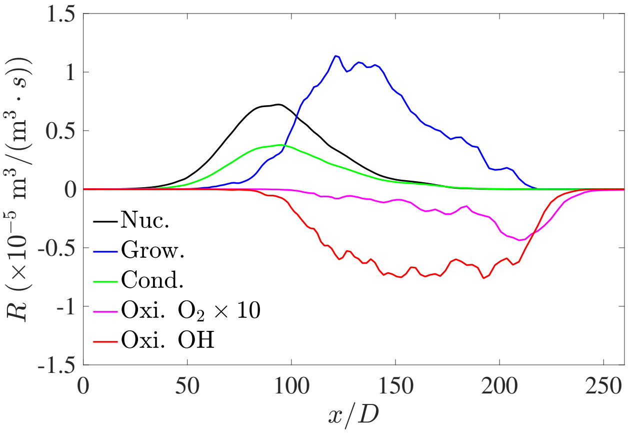

Figure 6.14: The mean rates of change for each soot formation process along the centreline by the LES-PBE-PDF method.

indicating that soot particles would experience strong surface growth right after they are formed. This feature also explains the overprediction for the mean soot volume fraction at the regions near the jet, as presented in Fig. 6.8a.

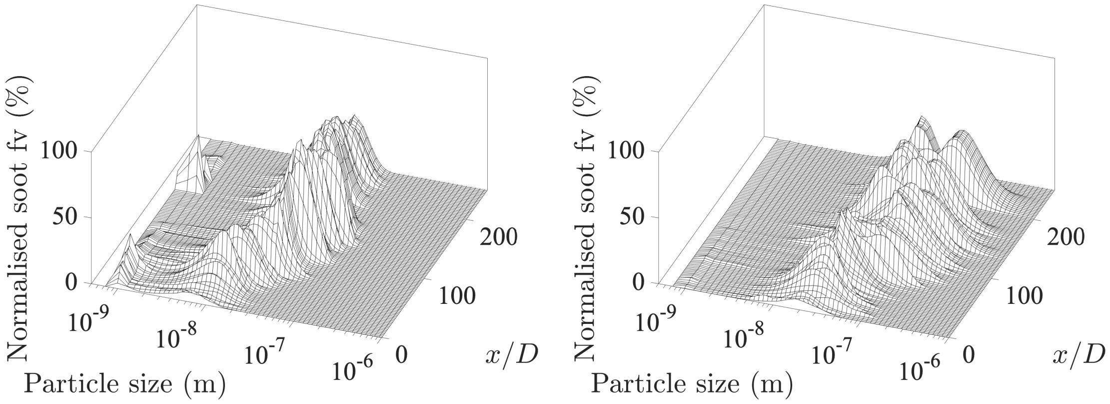

(a) $\alpha = 0.0037 \times e^{9000/T}$

(b) $\alpha = 0.0074 \times e^{9000/T}$

Figure 6.15: Impact of different surface reactivity on the instantaneous normalised soot volume distribution along the flame centreline.

6.2.3 Analysis of computational performance

Table 6.1 shows the CPU breakdown for each process in the simulation, calculated based on an average over 3000 time steps. It is evident that the greatest CPU cost is due to the gas-phase reaction, which takes almost half of the total CPU time. The solution of the PBE with the sectional method requires 17.79% of the total CPU time, indicating that it is not a major overload on the LES-PBE-PDF method. LES-PDF methods for turbulent combustion are generally expensive due to the high CPU cost for the integration of chemical kinetics, but the latter can be severely reduced by using using machine learning tabulation methods [198–200].

Table 6.1: Average runtimes for the LES-PBE-PDF method to advance one time step ($\Delta t = 3 \times 10^{-6}$ s) on 20 nodes (480 MPI processes) of ARCHER supercomputer.

Process	Average runtime (s)	Percentage
Scalar convection/diffusion	3.67	12.25%
Micromixing	1.59	5.31%
Gas phase reaction	14.86	49.60%
PBE solution	5.33	17.79%
Flow field	0.42	1.40%
All other processes	4.09	13.65%
Total CPU cost	29.96	-

6.3 Summary

Based on the findings in the laminar flame and employing the soot kinetics, the one-equation conservative finite volume PBE discretisation (CFV-1PBE) method was employed in a turbulent flame under the framework of LES-PBE-PDF, which allows for the interactions between turbulence, chemistry, and particle formation to be accounted for. Compared to previous applications [10, 11], a complete physicochemical model, incorporating particle coalescence and aggregation, was employed for the first time to predict soot formation in the turbulent flame. The turbulent transport was closed by a gradient diffusion hypothesis, and the conditional diffusion in the reactive scalars and number density space was modelled by an extension of the IEM model that accounts for differential diffusion. Subsequently, the transport equation for the joint scalar-number density PDF was solved using the method of Eulerian stochastic fields, in which eight stochastic fields were invoked to predict, in a statistical sense, the evolution of the joint scalar-number density PDF. The solution of the PBE with the conservative finite volume method does not require the closure assumptions needed in moment methods, while at the same time conserving the first moment (which is proportional to soot mass) in the aggregation process [7]. Note that in this method, any soot kinetics can be employed without further approximation on the turbulence-chemistry-soot interaction.

The LES-PBE-PDF method was applied to simulate a turbulent non-premixed flame using the same kinetics and implementation as employed in the Santoro non-premixed laminar sooting flame. By employing the same gas-phase and soot kinetics, aerosol dynamics models and CFD code implementation as in the laminar flame, I aim to shed light in the nature of the present challenges in modelling turbulent sooting flames. In the application to the Sandia turbulent non-premixed sooting flame, overall good agreement was obtained for the mean and RMS profiles of temperature, RMS X_{O_2}/X_{N_2} and normalised species profiles. The location and qualitative shape of the soot volume fraction axial and radial profiles were also well predicted, but the soot volume fraction was underpredicted, with an associated overprediction of the peak temperature. The uncertainties lie in soot kinetics and particularly in the model of surface reactivity, which is an adjustable parameter and was calibrated in the Santoro laminar flame simulations. Further adjustment of the reactivity in the turbulent flame yields results close to the experimental measurements for the axial profiles of soot and temperature, though some discrepancies in the radial profiles persist. The simulation dataset was finally utilised for an analysis of the soot formation processes and their relation with the spatial distribution of the precursor species.

It is clear that further research is needed in order for quantitative agreement to be accomplished without adjustments, particularly on the domain of soot kinetics, but the fact that several features of the soot formation could be captured with the same kinetics and code implementation used for both the laminar and turbulent flames is encouraging. Furthermore, a breakthrough of the CPU time among the various elements of the method showed that the solution of the PBE with the sectional method required 17.79% of the CPU time, thus indicating that the incorporation of aggregation in the context of the LES-PDF simulation is computationally feasible. Future work can consider incorporating into the LES-PBE-PDF framework more advanced soot kinetic models, such as models that consider the effect of soot carbonisation on surface reactivity [31, 55], as well as aerosol dynamics models that account for aggregate structure in a more realistic way (e.g., CFV-2PBE method). The use of such models in turbulent flame simulations could be greatly enhanced by the availability of more detailed experimental datasets on the properties of soot particles in turbulent flames. Moreover, for future work, it is interesting to investigate the impact of differential diffusion on reactive scalars, as well as the impact of different micromixing frequency for gas-phase scalars and soot number density. The impact of radiative heat transfer is also worth an investigation, as the current work employ a simple radiation model based upon the assumption of optically thin radiative heat loss.

Chapter 7

Conclusions and future work

7.1 Conclusions

The present thesis aims to address the research challenges introduced in Chapter 1 by: a) proposing a population balance approach for modelling soot formation that distinguishes between coalescence and aggregation and accounts for finite-rate fusing of primary particles within aggregates, while providing a numerically accurate description of primary particle surface growth and oxidation within aggregates, and b) introducing a comprehensive methodology for modelling turbulent sooting flames with detailed kinetics, aerosol dynamics and turbulence-chemistry-soot interaction by combining the LES-PBE-PDF method with the CFV-1PBE method for PBE solution. In particular, the important adjustable parameters (cut-off point d_c and surface reactivity α) were calibrated in the Santoro laminar flame and employed in the Sandia turbulent sooting flame. By doing so, this thesis attempts to conduct a systematic study of population balance modelling for soot formation in both the laminar and turbulent flame.

The first part of the thesis presented in detail the two-PBE approach that allows for more accurate modelling of primary particle surface growth and oxidation and furthermore involves a timescale for the fusing of primary particles. Specifically, CFV-2PBE resolves both the number density of aggregates and primary particles, taking into account the fusing process of primary particles. The accuracy of the numerical method was tested by reproducing the self-preserving distributions of aggregates with varying fractal dimension. Moreover, this part demonstrated how the two-PBE approaches could be coupled with CFD, and the CFD-PBE method was applied to the simulation of the Santoro laminar non-premixed co-flow sooting flame, where the two-PBE approach was compared with the one-PBE approach. As the soot mass addition is dominated by surface growth, the surface reactivity in the HACA mechanism is critical for the soot volume fraction prediction. My results showed that, with proper adjustments in the cut-off point and surface reactivity, the one-PBE approach is able to give a reasonably good prediction of soot volume fraction. On the other hand, the two-PBE approach attained this result with a consistent description of growth and a significant improvement in the description of soot morphology. At this stage, the model parameters for the fusing timescale are based on sintering models extrapolated from other nanoparticles, such as silica and titania, due to the lack of experimental data for soot. This work pointed out the need for further investigation in this area.

A major achievement of the first part is to lay the groundwork for the coupling of CFD-PBE to turbulent flames. As the conservative finite volume method attains accurate prediction of the distribution together with conservation of the first moment in aggregation, my goal is to prevent the compensation of errors between numerics and modelling. Considering that measurements in turbulent flames are mainly for soot volume fraction, the one-PBE method is a reasonable choice to be incorporated into the turbulent flame, for its computational efficiency and accuracy. Finally, the chemical mechanism and soot kinetic model employed in the laminar flame also demonstrated good predictive capabilities and were employed in the subsequent turbulent flame without adjustments.

Subsequently, in the second part of the thesis, CFV-1PBE method was incorporated into the LES-PBE-PDF framework. By doing so, the LES-PBE-PDF approach was fully coupled with a complete set of particle formation processes, including nucleation, surface growth, oxidation, condensation, coalescence and aggregation. The interaction between chemistry, turbulence and soot was accounted for, via a joint scalar-number density PDF transport equation. A turbulent diffusion hypothesis was used to provide closure for the turbulent transport term, and a micromixing model accounting for differential diffusion was employed to close the conditional diffusion term. The solution was obtained using a Monte-Carlo method, in which the Eulerian stochastic field method was employed to construct a stochastic process statistically equivalent to the joint scalar-number density PDF. One of the major advantages of the approach is that kinetic models of arbitrary complexity can be applied without additional assumptions on the turbulence-chemistry and turbulence-soot interaction, allowing a direct application of the same kinetics that was tested in the laminar flame.

The LES-PBE-PDF approach was then applied in the Sandia turbulent non-premixed sooting flame, initially without any adjustments on the model parameters obtained from the laminar flame. Despite some overpredictions on the temperature profile, the feature of the temperature field was well reproduced. The predicted $X_{\mathrm{O}_2}/X_{\mathrm{N}_2}$ profiles were in good agreement compared to the measurements. Qualitatively good predictions of OH and PAH showed that the method was able to capture the thermochemical condition, which is important for modelling soot formation. Regarding the mean and RMS soot volume fraction, predicted radial profiles and axial profiles along the flame centreline were in qualitatively good agreement with the measurements, with a consistent underprediction in the magnitude. Further adjustment of the reactivity in the turbulent flame predicts results close to the experimental measurements for the axial profiles of soot and temperature, though some discrepancies in the radial profiles persist. The work also found that the peak position in the profile of soot volume fraction along the flame centreline was less affected by the surface reaction, and possibly only relevant to the onset of the nucleation process, while the PSD could also be affected by the surface reactivity. Overall, the results demonstrated the good predictive capabilities and computational feasibility of the LES-PBE-PDF method, but uncertainties in kinetics and surface reaction warrant further investigations.

In conclusion, this thesis presented a comprehensive study of soot formation in both laminar and turbulent flames with sensitivity analysis regarding the key model parameters. A two-PBE method that accounts for soot morphology and finite-rate fusing of primary particles within aggregates was proposed and tested in the laminar flame, and an accurate one-PBE method was incorporated into the LES-PBE-PDF method to form a complete physicochemical model for the turbulent sooting flame simulations. By using accurate numerical methods, the chemistry and soot kinetics could be validated first in the laminar flames, and then employed into the turbulent flames using the comprehensive LES-PBE-PDF approach. As the current methodology neglects soot composition, a relatively simple model for surface reactivity was employed and thus some adjustments on the model parameter are inevitable. In the following sections, some potential model improvements are outlined, and suggestions about the future study are listed for consideration.

7.2 Suggestions for future work

In this section, a few thoughts for extending the CFD-PBE method and for further validating the comprehensive LES-PBE-PDF approach are collected. For each aspect, the main motivation, rationale and potential benefits are briefly summarised.

- ***Soot composition.*** As observed in the past studies, nascent and mature soot particles have significant differences in terms of properties, appearances and even nanostructures [31], particularly the surface reactivity [201]. The CFD-PBE method of this thesis neglects soot composition and is thus not yet able to distinguish between nascent and mature soot particle. The validation in Chapter 4 and Chapter 6 showed that soot surface reactivity α in HACA mechanism plays a dominant role in obtaining a quantitatively good prediction for soot volume fraction. Although surface reactivity was mainly modelled as a function of temperature or/and particle size (see Table 2.1 in Chapter 2) and treated as a free parameter when fitted with measurements in the past decade, several recent studies attempt to account for soot composition in modelling surface reactivity, e.g., Refs. [55, 188]. It is of interest to extend the current model such that the method can capture soot composition and subsequently be able to accommodate with the cutting-edge soot kinetics. A possible way to achieve this is to incorporate an extra property, soot C/H ratio, to describe the composition of soot, thus allowing for a more advanced model for the surface reactivity.

- ***Soot particle morphology.*** As the newly proposed CFV-2PBE method provides a physically more realistic description for aggregate growth and primary particles, it opens the possibility of investigating the impact of the morphology-related model parameters. In the present thesis, a constant fractal dimension was assumed, which is a simplification. Future work is warranted with respect to the impact of a varying fractal dimension on soot particle morphology. Moreover, the application of CFV-2PBE in the laminar flame showed a significant improvement for the description of soot morphology based on the fusing of primary particles. At this stage, experimental measurements associated with the fusing of primary particles are not yet available, and the sintering models appeared in a few numerical studies associated with soot were extrapolated from the model for other nanoparticles. As new experimental data become available, it should be possible to explore the potential of the CFV-2PBE method towards attaining good predictive simulations of soot morphology in flames.

- ***Turbulent sooting flame.*** The LES-PBE-PDF approach now provides a complete physicochemical model that can be applied in turbulent flames. As the interaction between turbulence, chemistry and soot can be accounted for without further assumptions, the method can be applied in various turbulent flames to test its predictive capabilities and robustness. Moreover, it is interesting to study the impact of differential diffusion on reactive scalars. Investigations will be needed regarding the micromixing model, however, as pointed out in [133], the micromixing frequency is a measure of the decay rate of the scalar variance. At present, limited experimental data is available in turbulent flames. As morphology data becomes available in the future, it will be worth exploring the

CFV-2PBE method under the framework of the LES-PBE-PDF approach, as the fraction of the CPU cost for the PBE fractional time step is only moderate.

Bibliography

[1] A. Liu, C. E. Garcia, F. Sewerin, B. A. O. Williams, and S. Rigopoulos, "Population balance modelling and laser diagnostic validation of soot particle evolution in laminar ethylene diffusion flames," *Combustion and Flame*, vol. 221, pp. 384–400, 2020.

[2] K. Donaldson, L. Tran, L. A. Jimenez, R. Duffin, D. E. Newby, N. Mills, W. MacNee, and V. Stone, "Combustion-derived nanoparticles: A review of their toxicology following inhalation exposure," *Particle and Fibre Toxicology*, vol. 2, 2005.

[3] R. F. Service, "Study fingers soot as a major player in global warming," *Science*, vol. 319, no. 5871, pp. 1745–1745, 2008.

[4] D. Shindell, J. C. I. Kuylenstierna, E. Vignati, R. Van Dingenen, M. Amann, Z. Klimont, S. C. Anenberg, N. Muller, G. Janssens-Maenhout, F. Raes, J. Schwartz, G. Faluvegi, L. Pozzoli, K. Kupiainen, L. Höglund-Isaksson, L. Emberson, D. Streets, V. Ramanathan, K. Hicks, N. T. K. Oanh, G. Milly, M. Williams, V. Demkine, and D. Fowler, "Simultaneously mitigating near-term climate change and improving human health and food security," *Science*, vol. 335, no. 6065, pp. 183–189, 2012.

[5] J. R. McConnell, R. Edwards, G. L. Kok, M. G. Flanner, C. S. Zender, E. S. Saltzman, J. R. Banta, D. R. Pasteris, M. M. Carter, and J. D. Kahl, "20th-century industrial black carbon emissions altered arctic climate forcing," *Science*, vol. 317, no. 5843, p. 1381–1384, 2007.

[6] T. L. Farias, Köylü, Ü. Ö., and M. G. Carvalho, “Effects of polydispersity of aggregates and primary particles on radiative properties of simulated soot,” *Journal of Quantitative Spectroscopy and Radiative Transfer*, vol. 55, no. 3, pp. 357–371, 1996.

[7] A. Liu and S. Rigopoulos, “A conservative method for numerical solution of the population balance equation, and application to soot formation,” *Combustion and Flame*, vol. 205, pp. 506–521, 2019.

[8] S. B. Dworkin, Q. Zhang, M. J. Thomson, N. A. Slavinskaya, and U. Riedel, “Application of an enhanced PAH growth model to soot formation in a laminar coflow ethylene/air diffusion flame,” *Combustion and Flame*, vol. 158, no. 9, pp. 1682–1695, 2011.

[9] S. Rigopoulos, “PDF method for population balance in turbulent reactive flow,” *Chemical Engineering Science*, vol. 62, no. 23, pp. 6865–6878, 2007.

[10] F. Sewerin and S. Rigopoulos, “An LES-PBE-PDF approach for modeling particle formation in turbulent reacting flows,” *Physics of Fluids*, vol. 29, no. 10, 2017.

[11] F. Sewerin and S. Rigopoulos, “An LES-PBE-PDF approach for predicting the soot particle size distribution in turbulent flames,” *Combustion and Flame*, vol. 189, pp. 62–76, 2018.

[12] H. Wang, “Formation of nascent soot and other condensed-phase materials in flames,” *Proceedings of the Combustion Institute*, vol. 33, no. 1, pp. 41–67, 2011.

[13] S. Harris and A. Weiner, “Surface growth of soot particles in premixed ethylene/air flames,” *Combustion Science and Technology*, vol. 31, no. 3-4, pp. 155–167, 1983.

[14] H. X. Zhang, C. M. Sorensen, E. R. Ramer, B. J. Olivier, and J. F. Merklin, "*In situ* optical structure factor measurements of an aggregating soot aerosol," *Langmuir*, vol. 4, pp. 867–871, 1988.

[15] H. A. Michelsen, M. B. Colket, P. Bengtsson, A. D'Anna, P. Desgroux, B. S. Haynes, J. H. Miller, G. J. Nathan, H. Pitsch, and H. Wang, "A review of terminology used to describe soot formation and evolution under combustion and pyrolytic conditions," *ACS Nano*, vol. 14, no. 10, pp. 12470–12490, 2020.

[16] J. Nagle and R. F. Strickland-Constable, "Oxidation of carbon between 1000-2000^{o}C," in *Proceedings of the Fifth Carbon Conference*, vol. 1, pp. 154–164, 1962.

[17] K. G. Neoh, J. B. Howard, and A. F. Sarofim, "Effect of oxidation on the physical structure of soot," *Symposium (International) on Combustion*, vol. 20, no. 1, pp. 951–957, 1985.

[18] B. S. Haynes and H. G. Wagner, "Soot formation," *Progress in Energy and Combustion Science*, vol. 7, no. 4, pp. 229–273, 1981.

[19] I. Glassman, "Soot formation in combustion processes," *Symposium (International) on Combustion*, vol. 22, no. 1, pp. 295–311, 1988.

[20] I. M. Kennedy, "Models of soot formation and oxidation," *Progress in Energy and Combustion Science*, vol. 23, no. 2, pp. 95–132, 1997.

[21] Z. A. Mansurov, "Soot formation in combustion processes (review)," *Combustion, Explosion and Shock Waves*, vol. 41, no. 6, pp. 727–744, 2005.

[22] A. D'Anna, "Combustion-formed nanoparticles," *Proceedings of the Combustion Institute*, vol. 32, no. 1, pp. 593–613, 2009.

[23] S. Rigopoulos, "Modelling of soot aerosol dynamics in turbulent flow," *Flow, Turbulence and Combustion*, vol. 103, no. 3, pp. 565–604, 2019.

[24] P. A. Tesner, T. D. Smegiriova, and V. G. Knorre, “Kinetics of dispersed carbon formation,” *Combustion and Flame*, vol. 17, no. 2, pp. 253–260, 1971.

[25] B. F. Magnussen and B. H. Hjertager, “On mathematical modeling of turbulent combustion with special emphasis on soot formation and combustion,” *Symposium (International) on Combustion*, vol. 16, no. 1, pp. 719–729, 1977.

[26] B. F. Magnussen, B. H. Hjertager, J. G. Olsen, and D. Bhaduri, “Effects of turbulent structure and local concentrations on soot formation and combustion in C_2H_2 diffusion flames,” *Symposium (International) on Combustion*, vol. 17, no. 1, pp. 1383–1393, 1979.

[27] Y. Xuan and G. Blanquart, “Effects of aromatic chemistry-turbulence interactions on soot formation in a turbulent non-premixed flame,” *Proceedings of the Combustion Institute*, vol. 35, no. 2, pp. 1911–1919, 2015.

[28] A. Jain and Y. Xuan, “Effects of large aromatic precursors on soot formation in turbulent non-premixed sooting jet flames,” *Combustion Theory and Modelling*, vol. 23, no. 3, pp. 439–466, 2019.

[29] P. Rodrigues, B. Franzelli, R. Vicquelin, O. Gicquel, and N. Darabiha, “Coupling an LES approach and a soot sectional model for the study of sooting turbulent non-premixed flames,” *Combustion and Flame*, vol. 190, pp. 477–499, 2018.

[30] K. M. Leung, R. P. Lindstedt, and W. P. Jones, “A simplified reaction mechanism for soot formation in nonpremixed flames,” *Combustion and Flame*, vol. 87, no. 3-4, pp. 289–305, 1991.

[31] M. Kholghy, A. Veshkini, and M. J. Thomson, “The core–shell internal nanostructure of soot – a criterion to model soot maturity,” *Carbon*, vol. 100, pp. 508–536, 2016.

[32] R. P. Lindstedt, "Simplified soot nucleation and surface growth steps for non-premixed flames," in *Soot Formation in Combustion* (H. Bockhorn, ed.), Springer Series in Chemical Physics 59, pp. 417–441, Springer-Verlag, 1994.

[33] R. J. Hall, M. D. Smooke, and M. B. Colket, "Predictions of soot dynamics in opposed jet diffusion flames," in *Physical and Chemical Aspects of Combustion: A Tribute to Irvin Glassman* (F. K. Dryer and R. F. Sawyer, eds.), Combustion Science and Technology Book Series, Volume 4, pp. 189–229, Gordon and Breach, 1997.

[34] P. Akridis and S. Rigopoulos, "Modelling of soot formation in laminar diffusion flames using a comprehensive CFD-PBE model with detailed gas-phase chemistry," *Combustion Theory and Modelling*, vol. 21, no. 1, pp. 35–48, 2017.

[35] P. Akridis and S. Rigopoulos, "Modelling of soot formation in a turbulent diffusion flame using a comprehensive CFD-PBE model with full chemistry," in *Proceedings of the European Combustion Meeting, Paper P4-47, Budapest, Hungary*, 2015.

[36] H. Richter and J. B. Howard, "Formation of polycyclic aromatic hydrocarbons and their growth to soot - a review of chemical reaction pathways," *Progress in Energy and Combustion Science*, vol. 26, no. 4, pp. 565–608, 2000.

[37] C. S. McEnally, L. D. Pfefferle, B. Atakan, and K. Kohse-Höinghaus, "Studies of aromatic hydrocarbon formation mechanisms in flames: Progress towards closing the fuel gap," *Progress in Energy and Combustion Science*, vol. 32, no. 3, pp. 247–294, 2006.

[38] M. Frenklach and J. Warnatz, "Detailed modeling of PAH profiles in a sooting low-pressure acetylene flame," *Combustion Science and Technology*, vol. 51, no. 4-6, pp. 265–283, 1987.

[39] M. Frenklach and H. Wang, “Detailed modeling of soot particle nucleation and growth,” *Symposium (International) on Combustion*, vol. 23, no. 1, pp. 1559–1566, 1991.

[40] M. Frenklach and H. Wang, “Detailed mechanism and modeling of soot particle formation,” in *Soot Formation in Combustion* (H. Bockhorn, ed.), Springer Series in Chemical Physics 59, pp. 162–192, Springer-Verlag, 1994.

[41] J. Appel, H. Bockhorn, and M. Frenklach, “Kinetic modeling of soot formation with detailed chemistry and physics: Laminar premixed flames of C2 hydrocarbons,” *Combustion and Flame*, vol. 121, no. 1-2, pp. 122–136, 2000.

[42] N. M. Marinov, W. J. Pitz, C. K. Westbrook, M. J. Castaldi, and S. M. Senkan, “Modeling of aromatic and polycyclic aromatic hydrocarbon formation in premixed methane and ethane flames,” *Combustion Science and Technology*, vol. 116-117, no. 1-6, pp. 211–287, 1996.

[43] A. D’Anna and J. H. Kent, “Aromatic formation pathways in non-premixed methane flames,” *Combustion and Flame*, vol. 132, no. 4, pp. 715–722, 2003.

[44] H. Richter, S. Granata, W. H. Green, and J. B. Howard, “Detailed modeling of PAH and soot formation in a laminar premixed benzene/oxygen/argon low-pressure flame,” *Proceedings of the Combustion Institute*, vol. 30, no. 1, pp. 1397–1404, 2005.

[45] N. A. Slavinskaya and P. Frank, “A modelling study of aromatic soot precursors formation in laminar methane and ethene flames,” *Combustion and Flame*, vol. 156, no. 9, pp. 1705–1722, 2009.

[46] G. Blanquart, P. Pepiot-Desjardins, and H. Pitsch, “Chemical mechanism for high temperature combustion of engine relevant fuels with emphasis on soot precursors,” *Combustion and Flame*, vol. 156, no. 3, pp. 588–607, 2009.

[47] Y. Wang, A. Raj, and S. H. Chung, "Soot modeling of counterflow diffusion flames of ethylene-based binary mixture fuels," *Combustion and Flame*, vol. 162, no. 3, pp. 586–596, 2015.

[48] S. J. Harris and A. M. Weiner, "Determination of the rate constant for soot surface growth," *Combustion Science and Technology*, vol. 32, no. 5-6, pp. 267–275, 1983.

[49] S. J. Brookes and J. B. Moss, "Predictions of soot and thermal radiation properties in confined turbulent jet diffusion flames," *Combustion and Flame*, vol. 116, no. 4, pp. 486–503, 1999.

[50] K. B. Lee, M. W. Thring, and J. M. Beér, "On the rate of combustion of soot in a laminar soot flame," *Combustion and Flame*, vol. 6, no. C, pp. 137–145, 1962.

[51] F. Liu, H. Guo, G. J. Smallwood, and Gülder, Ö. L., "Numerical modelling of soot formation and oxidation in laminar coflow non-smoking and smoking ethylene diffusion flames," *Combustion Theory and Modelling*, vol. 7, no. 2, pp. 301–315, 2003.

[52] M. Frenklach, "Reaction mechanism of soot formation in flames," *Physical Chemistry Chemical Physics*, vol. 4, no. 11, pp. 2028–2037, 2002.

[53] G. Blanquart and H. Pitsch, "A joint volume-surface-hydrogen multi-variate model for soot formation," in *Combustion Generated Fine Carbonaceous Particles* (H. Bockhorn, A. D'Anna, A. Sarofim, and H. Wang, eds.), pp. 437–463, KIT Scientific Publishing, 2009.

[54] H. Guo, F. Liu, G. J. Smallwood, and Gülder, Ö. L., "Numerical study on the influence of hydrogen addition on soot formation in a laminar ethylene–air diffusion flame," *Combustion and Flame*, vol. 145, no. 1, pp. 324–338, 2006.

[55] A. Veshkini, S. B. Dworkin, and M. J. Thomson, “A soot particle surface reactivity model applied to a wide range of laminar ethylene/air flames,” *Combustion and Flame*, vol. 161, no. 12, pp. 3191–3200, 2014.

[56] R. Drake, “A general mathematical survey of the coagulation equation,” in *Topics in Current Aerosol Research* (G. M. Hidy and J. R. Brock, eds.), pp. 204–376, Pergamon, 1972.

[57] S. K. Friedlander, *Smoke, Dust, and Haze: Fundamentals of Aerosol Dynamics.* Oxford University Press, 2nd ed., 2000.

[58] D. Ramkrishna, *Population Balances: Theory and Applications to Particulate Systems in Engineering.* Academic Press, 2000.

[59] S. Rigopoulos, “Population balance modelling of polydispersed particles in reactive flows,” *Progress in Energy and Combustion Science*, vol. 36, no. 4, pp. 412–443, 2010.

[60] M. V. Smoluchowski, “Mathematical theory of the kinetics of coagulation of colloidal systems,” *Z. Phys. Chem.*, vol. 92, pp. 129–168, 1917.

[61] S. K. Friedlander, “On the particle size spectrum of a condensing vapor,” *Physics of Fluids*, vol. 3, no. 5, pp. 693–696, 1960.

[62] S. E. Pratsinis, “Simultaneous nucleation, condensation, and coagulation in aerosol reactors,” *Journal of Colloid and Interface Science*, vol. 124, no. 2, pp. 416–427, 1988.

[63] C. N. Davies, “Definitive equations for the fluid resistance of spheres,” *Proceedings of the Physical Society*, vol. 57, no. 4, pp. 259–270, 1945.

[64] J. H. Seinfeld and S. N. Pandis, *Atmospheric Chemistry and Physics: From Air Pollution to Climate Change.* Wiley, 3rd ed., 2016.

[65] N. A. Fuchs, *Mechanics of Aerosols.* Pergamon, New York, 1964.

[66] Köylü, Ü. Ö., G. M. Faeth, T. L. Farias, and M. G. Carvalho, "Fractal and projected structure properties of soot aggregates," *Combustion and Flame*, vol. 100, no. 4, pp. 621–633, 1995.

[67] O. Link, D. R. Snelling, K. A. Thomson, and G. J. Smallwood, "Development of absolute intensity multi-angle light scattering for the determination of polydisperse soot aggregate properties," *Proceedings of the Combustion Institute*, vol. 33, pp. 847–854, 2011.

[68] A. Kazakov and M. Frenklach, "Dynamic modeling of soot particle coagulation and aggregation: Implementation with the method of moments and application to high-pressure laminar premixed flames," *Combustion and Flame*, vol. 114, no. 3-4, pp. 484–501, 1998.

[69] A. M. Brasil, T. L. Farias, and M. G. Carvalho, "A recipe for image characterization of fractal-like aggregates," *Journal of Aerosol Science*, vol. 30, no. 10, pp. 1379–1389, 1999.

[70] M. Balthasar and M. Kraft, "A stochastic approach to calculate the particle size distribution function of soot particles in laminar premixed flames," *Combustion and Flame*, vol. 133, no. 3, pp. 289–298, 2003.

[71] A. Bouaniche, J. Yon, P. Domingo, and L. Vervisch, "Analysis of the soot particle size distribution in a laminar premixed flame: a hybrid stochastic/fixed-sectional approach," *Flow, Turbulence and Combustion*, vol. 104, pp. 753–775, 2020.

[72] M. Frenklach and S. J. Harris, "Aerosol dynamics modeling using the method of moments," *Journal of Colloid and Interface Science*, vol. 118, no. 1, pp. 252–261, 1987.

[73] M. Frenklach, "Method of moments with interpolative closure," *Chemical Engineering Science*, vol. 57, no. 12, pp. 2229–2239, 2002.

[74] M. E. Mueller, G. Blanquart, and H. Pitsch, "A joint volume-surface model of soot aggregation with the method of moments," *Proceedings of the Combustion Institute*, vol. 32, no. 1, pp. 785–792, 2009.

[75] R. Bleck, "A fast, approximative method for integrating the stochastic coalescence equation," *Journal of Geophysical Research*, vol. 75, no. 27, pp. 5165–5171, 1970.

[76] F. Gelbard, Y. Tambour, and J. H. Seinfeld, "Sectional representations for simulating aerosol dynamics," *Journal of Colloid and Interface Science*, vol. 76, no. 2, pp. 541–556, 1980.

[77] M. B. Colket and R. J. Hall, "Successes and uncertainties in modelling soot formation in laminar, premixed flames," in *Soot Formation in Combustion* (H. Bockhorn, ed.), Springer Series in Chemical Physics 59, pp. 442–470, Springer-Verlag, 1994.

[78] M. D. Smooke, R. J. Hall, M. B. Colket, J. Fielding, M. B. Long, C. S. McEnally, and L. D. Pfefferle, "Investigation of the transition from lightly sooting towards heavily sooting co-flow ethylene diffusion flames," *Combustion Theory and Modelling*, vol. 8, no. 3, pp. 593–606, 2004.

[79] M. D. Smooke, M. B. Long, B. C. Connelly, M. B. Colket, and R. J. Hall, "Soot formation in laminar diffusion flames," *Combustion and Flame*, vol. 143, no. 4, pp. 613–628, 2005.

[80] S. B. Dworkin, M. D. Smooke, and V. Giovangigli, "The impact of detailed multicomponent transport and thermal diffusion effects on soot formation in ethylene/air flames," *Proceedings of the Combustion Institute*, vol. 32, no. 1, pp. 1165–1172, 2009.

[81] S. Kumar and D. Ramkrishna, “On the solution of population balance equations by discretization - I. A fixed pivot technique,” *Chemical Engineering Science*, vol. 51, no. 8, pp. 1311–1332, 1996.

[82] S. H. Park, S. N. Rogak, W. K. Bushe, J. Z. Wen, and M. J. Thomson, “An aerosol model to predict size and structure of soot particles,” *Combustion Theory and Modelling*, vol. 9, no. 3, pp. 499–513, 2005.

[83] J. Z. Wen, M. J. Thomson, S. H. Park, S. N. Rogak, and M. F. Lightstone, “Study of soot growth in a plug flow reactor using a moving sectional model,” *Proceedings of the Combustion Institute*, vol. 30, no. 1, pp. 1477–1483, 2005.

[84] F. Sewerin and S. Rigopoulos, “An explicit adaptive grid approach for the numerical solution of the population balance equation,” *Chemical Engineering Science*, vol. 168, pp. 250–270, 2017.

[85] F. Sewerin and S. Rigopoulos, “Algorithmic aspects of the LES-PBE-PDF method for modeling soot particle size distributions in turbulent flames,” *Combustion Science and Technology*, vol. 191, no. 5-6, pp. 766–796, 2019.

[86] K. Netzell, H. Lehtiniemi, and F. Mauss, “Calculating the soot particle size distribution function in turbulent diffusion flames using a sectional method,” *Proceedings of the Combustion Institute*, vol. 31, no. 1, pp. 667–674, 2007.

[87] P. Rodrigues, B. Franzelli, R. Vicquelin, O. Gicquel, and N. Darabiha, “Unsteady dynamics of PAH and soot particles in laminar counterflow diffusion flames,” *Proceedings of the Combustion Institute*, vol. 36, no. 1, pp. 927–934, 2017.

[88] W. Koch and S. K. Friedlander, “The effect of particle coalescence on the surface area of a coagulating aerosol,” *Journal of Colloid and Interface Science*, vol. 140, no. 2, pp. 419–427, 1990.

[89] Y. Xiong and S. E. Pratsinis, "Formation of agglomerate particles by coagulation and sintering - Part I. A two-dimensional solution of the population balance equation," *Journal of Aerosol Science*, vol. 24, no. 3, pp. 283–300, 1993.

[90] Y. Xiong, M. Kamal Akhtar, and S. E. Pratsinis, "Formation of agglomerate particles by coagulation and sintering - Part II. The evolution of the morphology of aerosol-made titania, silica and silica-doped titania powders," *Journal of Aerosol Science*, vol. 24, no. 3, pp. 301–313, 1993.

[91] S. N. Rogak, "Modeling small cluster deposition on the primary particles of aerosol agglomerates," *Journal of Aerosol Science*, vol. 26, pp. 127–140, 1997.

[92] S. Tsantilis and S. Pratsinis, "Evolution of primary and aggregate particle-size distributions by coagulation and sintering," *AIChE Journal*, vol. 46, no. 2, pp. 407–415, 2000.

[93] J. I. Jeong and M. Choi, "A sectional method for the analysis of growth of polydisperse non-spherical particles undergoing coagulation and coalescence," *Journal of Aerosol Science*, vol. 32, no. 5, pp. 565–582, 2001.

[94] S. H. Park and S. N. Rogak, "A one-dimensional model for coagulation, sintering, and surface growth of aerosol agglomerates," *Aerosol Science and Technology*, vol. 37, no. 12, pp. 947–960, 2003.

[95] S. H. Park and S. N. Rogak, "A novel fixed-sectional model for the formation and growth of aerosol agglomerates," *Journal of Aerosol Science*, vol. 35, no. 11, pp. 1385–1404, 2004.

[96] A. Khosousi and S. B. Dworkin, "Soot surface reactivity during surface growth and oxidation in laminar diffusion flames," *Combustion and Flame*, vol. 162, no. 12, pp. 4523–4532, 2015.

[97] N. A. Eaves, Q. Zhang, F. Liu, H. Guo, S. B. Dworkin, and M. J. Thomson, "Coflame: A refined and validated numerical algorithm for modeling sooting

laminar coflow diffusion flames," *Computer Physics Communications*, vol. 207, pp. 464–477, 2016.

[98] A. Veshkini, S. B. Dworkin, and M. J. Thomson, "Understanding soot particle size evolution in laminar ethylene/air diffusion flames using novel soot coalescence models," *Combustion Theory and Modelling*, vol. 20, no. 4, pp. 707–734, 2016.

[99] D. Chen, Z. Zainuddin, E. Yapp, J. Akroyd, S. Mosbach, and M. Kraft, "A fully coupled simulation of pah and soot growth with a population balance model," *Proceedings of the Combustion Institute*, vol. 34, pp. 1827–1835, 2013.

[100] F. A. Williams, "Elementary derivation of the multicomponent diffusion equation," *American Journal of Physics*, vol. 26, no. 7, pp. 467–469, 1958.

[101] R. B. Bird, W. E. Stewart, and E. N. Lightfoot, *Transport Phenomena.* Wiley International edition, Wiley, 2006.

[102] L. F. Richardson, *Weather prediction by numerical process.* Cambridge University Press, 1922.

[103] S. B. Pope, *Turbulent flows.* Cambridge University Press, 2000.

[104] A. N. Kolmogorov, "The local structure of turbulence in incompressible viscous fluid for very large reynolds' numbers," *Akademiia Nauk SSSR Doklady*, vol. 30, pp. 301–305, 1941.

[105] W. P. Jones and B. E. Launder, "The prediction of laminarization with a two-equation model of turbulence," *International Journal of Heat and Mass Transfer*, vol. 15, no. 2, pp. 301–314, 1972.

[106] W. P. Jones and V. N. Prasad, "Large eddy simulation of the sandia flame series (d–f) using the eulerian stochastic field method," *Combustion and Flame*, vol. 157, no. 9, pp. 1621–1636, 2010.

[107] D. Veynante and L. Vervisch, “Turbulent combustion modeling,” *Progress in Energy and Combustion Science*, vol. 28, no. 3, pp. 193–266, 2002.

[108] N. Peters, *Turbulent Combustion.* Cambridge University Press, 2000.

[109] H. Pitsch, “Large-eddy simulation of turbulent combustion,” *Annual Review of Fluid Mechanics*, vol. 38, no. 1, pp. 453–482, 2006.

[110] W. P. Jones, “The joint scalar probability density function method,” in *Closure Strategies for Turbulent and Transitional Flows* (B. E. Launder and N. D. E. Sandham, eds.), p. 582–625, Cambridge University Press, 2002.

[111] N. Peters, “Local quenching due to flame stretch and non-premixed turbulent combustion,” *Combustion Science and Technology*, vol. 30, no. 1-6, pp. 1–17, 1983.

[112] N. Peters, “Laminar diffusion flamelet models in non-premixed turbulent combustion,” *Progress in Energy and Combustion Science*, vol. 10, no. 3, pp. 319–339, 1984.

[113] A. W. Cook, J. J. Riley, and G. Kosály, “A laminar flamelet approach to subgrid-scale chemistry in turbulent flows,” *Combustion and Flame*, vol. 109, no. 3, pp. 332–341, 1997.

[114] C. Jiménez, F. Ducros, B. Cuenot, and B. Bédat, “Subgrid scale variance and dissipation of a scalar field in large eddy simulations,” *Physics of Fluids*, vol. 13, no. 6, pp. 1748–1754, 2001.

[115] C. D. Pierce and P. Moin, “A dynamic model for subgrid-scale variance and dissipation rate of a conserved scalar,” *Physics of Fluids*, vol. 10, no. 12, pp. 3041–3044, 1998.

[116] C. D. Pierce and P. Moin, “Progress-variable approach for large-eddy simulation of non-premixed turbulent combustion,” *Journal of Fluid Mechanics*, no. 504, pp. 73–97, 2004.

[117] M. Ihme and H. Pitsch, "Modeling of radiation and nitric oxide formation in turbulent nonpremixed flames using a flamelet/progress variable formulation," *Physics of Fluids*, vol. 20, no. 5, 2008.

[118] M. E. Mueller and H. Pitsch, "LES model for sooting turbulent nonpremixed flames," *Combustion and Flame*, vol. 159, no. 6, pp. 2166–2180, 2012.

[119] M. E. Mueller and V. Raman, "Effects of turbulent combustion modeling errors on soot evolution in a turbulent nonpremixed jet flame," *Combustion and Flame*, vol. 161, no. 7, pp. 1842–1848, 2014.

[120] A. Y. Klimenko, "Multicomponent diffusion of various admixtures in turbulent flow," *Fluid Dynamics*, vol. 25, p. 327–334, 1990.

[121] R. W. Bilger, "Conditional moment closure for turbulent reacting flow," *Physics of Fluids A: Fluid Dynamics*, vol. 5, no. 2, pp. 436–444, 1993.

[122] A. Y. Klimenko and R. W. Bilger, "Conditional moment closure for turbulent combustion," *Progress in Energy and Combustion Science*, vol. 25, no. 6, pp. 595–687, 1999.

[123] S. Navarro-Martinez, A. Kronenburg, and F. D. Mare, "Conditional moment closure for large eddy simulations," *Flow, Turbulence and Combustion*, vol. 75, pp. 245–274, 2005.

[124] S. Navarro-Martinez and S. Rigopoulos, "Differential diffusion modelling in LES with RCCE-reduced chemistry," *Flow, Turbulence and Combustion*, vol. 89, no. 2, pp. 311–328, 2012.

[125] A. Kronenburg, R. W. Bilger, and J. H. Kent, "Modeling soot formation in turbulent methane-air jet diffusion flames," *Combustion and Flame*, vol. 121, no. 1-2, pp. 24–40, 2000.

[126] Yunardi, R. M. Woolley, and M. Fairweather, "Conditional moment closure prediction of soot formation in turbulent, nonpremixed ethylene flames," *Combustion and Flame*, vol. 152, no. 3, pp. 360–376, 2008.

[127] M. Bolla, Y. M. Wright, K. Boulouchos, G. Borghesi, and E. Mastorakos, "Soot formation modeling of n-heptane sprays under diesel engine conditions using the conditional moment closure approach," *Combustion Science and Technology*, vol. 185, no. 5, pp. 766–793, 2013.

[128] T. S. Lundgren, "Distribution functions in the statistical theory of turbulence," *The Physics of Fluids*, vol. 10, no. 5, pp. 969–975, 1967.

[129] S. B. Pope, "PDF methods for turbulent reactive flows," *Progress in Energy and Combustion Science*, vol. 11, no. 2, pp. 119–192, 1985.

[130] E. E. O'Brien, "The probability density function (pdf) approach to reacting turbulent flows," in *Turbulent Reacting Flows* (P. A. Libby and F. A. Williams, eds.), pp. 185–218, Berlin, Heidelberg: Springer Berlin Heidelberg, 1980.

[131] P. J. Colucci, F. A. Jaberi, P. Givi, and S. B. Pope, "Filtered density function for large eddy simulation of turbulent reacting flows," *Physics of Fluids*, vol. 10, no. 2, pp. 499–515, 1998.

[132] R. O. Fox, *Computational models for turbulent reacting flows.* Cambridge Series in Chemical Engineering, Cambridge University Press, 2003.

[133] R. McDermott and S. B. Pope, "A particle formulation for treating differential diffusion in filtered density function methods," *Journal of Computational Physics*, vol. 226, no. 1, pp. 947–993, 2007.

[134] C. Dopazo and E. E. O'Brien, "An approach to the autoignition of a turbulent mixture," *Acta Astronautica*, vol. 1, no. 9-10, pp. 1239–1266, 1974.

[135] S. B. Pope, "A Monte Carlo method for the PDF equations of turbulent reactive flow," *Combustion Science and Technology*, vol. 25, no. 5-6, pp. 159–174, 1981.

[136] L. Valiño, "Field Monte Carlo formulation for calculating the probability density function of a single scalar in a turbulent flow," *Flow, Turbulence and Combustion*, vol. 60, no. 2, pp. 157–172, 1998.

[137] G. Hauke and L. Valiño, "Computing reactive flows with a field monte carlo formulation and multi-scale methods," *Computer Methods in Applied Mechanics and Engineering*, vol. 193, no. 15, pp. 1455–1470, 2004.

[138] V. Sabel'nikov and O. Soulard, "Rapidly decorrelating velocity-field model as a tool for solving one-point Fokker-Planck equations for probability density functions of turbulent reactive scalars," *Physical Review E - Statistical, Nonlinear, and Soft Matter Physics*, vol. 72, no. 1, 2005.

[139] F. Bisetti, G. Blanquart, M. E. Mueller, and H. Pitsch, "On the formation and early evolution of soot in turbulent nonpremixed flames," *Combustion and Flame*, vol. 159, no. 1, pp. 317–335, 2012.

[140] F. Bisetti, A. Attili, and H. Pitsch, "Advancing predictive models for particulate formation in turbulent flames via massively parallel direct numerical simulations," *Philosophical Transactions of the Royal Society A: Mathematical, Physical and Engineering Sciences*, vol. 372, no. 2022, p. 20130324, 2014.

[141] A. Attili, F. Bisetti, M. E. Mueller, and H. Pitsch, "Formation, growth, and transport of soot in a three-dimensional turbulent non-premixed jet flame," *Combustion and Flame*, vol. 161, no. 7, pp. 1849–1865, 2014.

[142] V. Raman and R. O. Fox, "Modeling of fine-particle formation in turbulent flames," *Annual Review of Fluid Mechanics*, vol. 48, pp. 159–190, 2016.

[143] A. Attili and F. Bisetti, "Application of a robust and efficient Lagrangian particle scheme to soot transport in turbulent flames," *Computers and Fluids*, vol. 84, pp. 164–175, 2013.

[144] A. Attili, F. Bisetti, M. E. Mueller, and H. Pitsch, "Damköhler number effects on soot formation and growth in turbulent nonpremixed flames," *Proceedings of the Combustion Institute*, vol. 35, no. 2, pp. 1215–1223, 2015.

[145] A. Attili, F. Bisetti, M. E. Mueller, and H. Pitsch, "Effects of non-unity Lewis number of gas-phase species in turbulent nonpremixed sooting flames," *Combustion and Flame*, vol. 166, pp. 192–202, 2016.

[146] H. El-Asrag, T. Lu, C. K. Law, and S. Menon, "Simulation of soot formation in turbulent premixed flames," *Combustion and Flame*, vol. 150, no. 1-2, pp. 108–126, 2007.

[147] H. El-Asrag and S. Menon, "Large eddy simulation of soot formation in a turbulent non-premixed jet flame," *Combustion and Flame*, vol. 156, no. 2, pp. 385–395, 2009.

[148] M. E. Mueller and H. Pitsch, "Large eddy simulation subfilter modeling of soot-turbulence interactions," *Physics of Fluids*, vol. 23, no. 11, 2011.

[149] P. Donde, V. Raman, M. E. Mueller, and H. Pitsch, "LES/PDF based modeling of soot-turbulence interactions in turbulent flames," *Proceedings of the Combustion Institute*, vol. 34, no. 1, pp. 1183–1192, 2013.

[150] M. E. Mueller, Q. N. Chan, N. H. Qamar, B. B. Dally, H. Pitsch, Z. T. Alwahabi, and G. J. Nathan, "Experimental and computational study of soot evolution in a turbulent nonpremixed bluff body ethylene flame," *Combustion and Flame*, vol. 160, no. 7, pp. 1298–1309, 2013.

[151] M. E. Mueller and H. Pitsch, "Large eddy simulation of soot evolution in an aircraft combustor," *Physics of Fluids*, vol. 25, no. 11, 2013.

[152] H. Koo, M. Hassanaly, V. Raman, M. E. Mueller, and K. P. Geigle, "Large-Eddy Simulation of soot formation in a model gas turbine combustor," *Journal of Engineering for Gas Turbines and Power*, vol. 139, no. 3, 2017.

[153] C. Eberle, P. Gerlinger, K. P. Geigle, and M. Aigner, “Toward finite-rate chemistry large-eddy simulations of sooting swirl flames,” *Combustion Science and Technology*, vol. 190, no. 7, pp. 1194–1217, 2018.

[154] A. Giusti, E. Mastorakos, C. Hassa, J. Heinze, E. Magens, and M. Zedda, “Investigation of flame structure and soot formation in a single sector model combustor using experiments and numerical simulations based on the large eddy simulation/conditional moment closure approach,” *Journal of Engineering for Gas Turbines and Power*, vol. 140, no. 6, 2018.

[155] W. Han, V. Raman, M. E. Mueller, and Z. Chen, “Effects of combustion models on soot formation and evolution in turbulent nonpremixed flames,” *Proceedings of the Combustion Institute*, vol. 37, no. 1, pp. 985–992, 2019.

[156] S. Yang, J. K. Lew, and M. E. Mueller, “Large eddy simulation of soot evolution in turbulent reacting flows: presumed subfilter pdf model for soot–turbulence–chemistry interactions,” *Combustion and Flame*, vol. 209, pp. 200–213, 2019.

[157] S. Gkantonas, M. Sirignano, A. Giusti, A. D’Anna, and E. Mastorakos, “Comprehensive soot particle size distribution modelling of a model Rich-Quench-Lean burner,” *Fuel*, vol. 270, 2020.

[158] T. W. J. Peeters, P. P. J. Stroomer, J. E. de Vries, D. J. E. M. Roekaerts, and C. J. Hoogendoorn, “Comparative experimental and numerical investigation of a piloted turbulent natural-gas diffusion flame,” *Symposium (International) on Combustion*, vol. 25, no. 1, pp. 1241–1248, 1994.

[159] G. Di Veroli and S. Rigopoulos, “A study of turbulence-chemistry interaction in reactive precipitation via a population balance-transported PDF method,” in *Turbulence, Heat and Mass Transfer 6. Proceedings of the Sixth International Symposium on Turbulence, Heat and Mass Transfer, Rome, Italy* (K. Hanjalić, Y. Nagano, and S. Jakirlić, eds.), Begell House, Inc., 2009.

[160] G. Y. Di Veroli and S. Rigopoulos, "Modeling of turbulent precipitation: A transported population balance-PDF method," *AIChE Journal*, vol. 56, pp. 878–892, Apr. 2010.

[161] G. Y. Di Veroli and S. Rigopoulos, "Modeling of aerosol formation in a turbulent jet with the transported population balance equation-probability density function approach," *Physics of Fluids*, vol. 23, no. 4, 2011.

[162] Q. Zhang, M. J. Thomson, H. Guo, F. Liu, and G. J. Smallwood, "A numerical study of soot aggregate formation in a laminar coflow diffusion flame," *Combustion and Flame*, vol. 156, no. 3, pp. 697–705, 2009.

[163] C. Saggese, S. Ferrario, J. Camacho, A. Cuoci, A. Frassoldati, E. Ranzi, H. Wang, and T. Faravelli, "Kinetic modeling of particle size distribution of soot in a premixed burner-stabilized stagnation ethylene flame," *Combustion and Flame*, vol. 162, no. 9, pp. 3356–3369, 2015.

[164] U. O. Köylü, C. S. McEnally, D. E. Rosner, and L. D. Pfefferle, "Simultaneous measurements of soot volume fraction and particle size / microstructure in flames using a thermophoretic sampling technique," *Combustion and Flame*, vol. 110, no. 4, pp. 494–507, 1997.

[165] M. Schenk, S. Lieb, H. Vieker, A. Beyer, A. Gölzhäuser, H. Wang, and K. Kohse-Höinghaus, "Morphology of nascent soot in ethylene flames," *Proceedings of the Combustion Institute*, vol. 35, no. 2, pp. 1879–1886, 2015.

[166] B. Koren, "A robust upwind discretization method for advection, diffusion and source terms," in *Numerical Methods for Advection-Diffusion Problems* (C. B. Vreugdenhil and B. Koren, eds.), vol. 45 of *Notes on Numerical Fluid Mechanics and Multidisciplinary Design*, pp. 117–138, Vieweg Verlag, 1993.

[167] S. Qamar, M. P. Elsner, I. A. Angelov, G. Warnecke, and A. Seidel-Morgenstern, "A comparative study of high resolution schemes for solving population bal-

ances in crystallization," *Computers and Chemical Engineering*, vol. 30, no. 6-7, pp. 1119–1131, 2006.

[168] S. Qamar, G. Warnecke, and M. P. Elsner, "On the solution of population balances for nucleation,growth,aggregation and breakage processes," *Chemical Engineering Science*, vol. 64, pp. 2088–2095, 2009.

[169] N. H. Qamar, Z. T. Alwahabi, Q. N. Chan, G. J. Nathan, D. Roekaerts, and K. D. King, "Soot volume fraction in a piloted turbulent jet non-premixed flame of natural gas," *Combustion and Flame*, vol. 156, no. 7, pp. 1339–1347, 2009.

[170] S. Vemury and S. E. Pratsinis, "Self-preserving size distributions of agglomerates," *Journal of Aerosol Science*, vol. 26, no. 2, pp. 175–185, 1995.

[171] S. K. Friedlander and C. S. Wang, "The self-preserving particle size distribution for coagulation by Brownian motion," *Journal of Colloid and Interface Science*, vol. 22, no. 2, pp. 126–132, 1966.

[172] R. J. Santoro, H. G. Semerjian, and R. A. Dobbins, "Soot particle measurements in diffusion flames," *Combustion and Flame*, vol. 51, no. C, pp. 203–218, 1983.

[173] R. P. Lindstedt and S. A. Louloudi, "Joint-scalar transported PDF modeling of soot formation and oxidation," *Proceedings of the Combustion Institute*, vol. 30, no. 1, pp. 775–782, 2005.

[174] W. L. Grosshandler, *RADCAL: a Narrow-band model for radiation calculations in a combustion environment.* NIST technical note 1402, National Institute of Standards and Technology, Building and Fire Research Laboratory, 1993.

[175] S. J. Harris and I. M. Kennedy, "The coagulation of soot particles with van der waals forces," *Combustion Science and Technology*, vol. 59, pp. 443–454, 1988.

[176] C. Marchal, *Soot formation and oxidation modelling in an automotive engine.* PhD thesis, Université d'Orléans, 2008.

[177] S. Tsantilis, H. Briesen, and S. E. Pratsinis, “Sintering time for silica particle growth,” *Journal of Aerosol Science*, vol. 34, no. 3, pp. 237–246, 2001.

[178] A. Kobata, K. Kusakabe, and S. Morooka, “Growth and transformation of tio2 crystallites in aerosol reactor,” *AIChE Journal*, vol. 37, no. 3, pp. 347–359, 1991.

[179] E. Goudeli, M. L. Eggersdorfer, and S. E. Pratsinis, “Aggregate characteristics accounting for the evolving fractal-like structure during coagulation and sintering,” *Journal of Aerosol Science*, vol. 89, pp. 58–68, 2015.

[180] R. J. Santoro, T. T. Yeh, J. J. Horvath, and H. G. Semerjian, “The transport and growth of soot particles in laminar diffusion flames,” *Combustion Science and Technology*, vol. 53, no. 2-3, pp. 89–115, 1987.

[181] C. M. Megaridis and R. A. Dobbins, “Comparison of soot growth and oxidation in smoking and non–smoking ethylene diffusion flames,” *Combustion Science and Technology*, vol. 66, pp. 1–16, 1989.

[182] S. S. Iyer, T. A. Litzinger, S. Y. Lee, and R. J. Santoro, “Determination of soot scattering coefficient from extinction and three-angle scattering in a laminar diffusion flame,” *Combustion and Flame*, vol. 149, no. 1, pp. 206–216, 2007.

[183] Q. Zhang, H. Guo, F. Liu, G. Smallwood, and M. Thomson, “Modeling of soot aggregate formation and size distribution in a laminar ethylene/air coflow diffusion flame with detailed PAH chemistry and an advanced sectional aerosol dynamics model,” *Proceedings of the Combustion Institute*, vol. 32, no. 1, pp. 761–768, 2009.

[184] H. Guo, F. Liu, G. J. Smallwood, and Gülder, Ö. L., “The flame preheating effect on numerical modelling of soot formation in a two-dimensional laminar ethylene–air diffusion flame,” *Combustion Theory and Modelling*, vol. 6, no. 2, pp. 173–187, 2002.

[185] J. D. Landgrebe and S. E. Pratsinis, "A discrete-sectional model for particulate production by gas-phase chemical reaction and aerosol coagulation in the free-molecular regime," *Journal of Colloid and Interface Science*, vol. 139, no. 1, pp. 63–86, 1990.

[186] I. M. Kennedy, C. Yam, D. C. Rapp, and R. J. Santoro, "Modeling and measurements of soot and species in a laminar diffusion flame," *Combustion and Flame*, vol. 107, no. 4, pp. 368–382, 1996.

[187] R. Puri, T. F. Richardson, R. J. Santoro, and D. R. A., "Aerosol dynamic processes of soot aggregates in a laminar ethene diffusion flame," *Combustion and Flame*, vol. 92, no. 3, pp. 320–333, 1993.

[188] D. Chen and K. Luo, "Reactive sites on the surface of polycyclic aromatic hydrocarbon clusters: A numerical study," *Combustion and Flame*, vol. 211, pp. 362–373, 2020.

[189] G. A. Kelesidis and S. E. Pratsinis (in press), "Determination of the volume fraction of soot accounting for its composition and morphology," *Proceedings of the Combustion Institute*, 2020.

[190] E. Goudeli, M. L. Eggersdorfer, and S. E. Pratsinis, "Coagulation–agglomeration of fractal-like particles: structure and self-preserving size distribution," *Langmuir*, vol. 31, no. 4, pp. 1320–1327, 2015.

[191] V. N. Prasad, *Large eddy simulation of partially premixed turbulent combustion.* PhD thesis, Imperial College London, 2011.

[192] G. A. Pavliotis, *Stochastic Processes and Applications.* Springer-Verlag New York, 2014.

[193] J. Y. Zhang, C. R. Shaddix, and R. W. Schefer, "Design of "model-friendly" turbulent non-premixed jet burners for C2+ hydrocarbon fuels," *Review of Scientific Instruments*, vol. 82, no. 7, p. 074101, 2011.

[194] M. E. Mueller, G. Blanquart, and H. Pitsch, "A joint volume-surface model of soot aggregation with the method of moments," *Proceedings of the Combustion Institute*, vol. 32, no. 1, pp. 785–792, 2009.

[195] S. P. Kearney, D. R. Guildenbecher, C. Winters, P. A. Farias, T. W. Grasser, and J. C. Hewson, "Temperature, oxygen, and soot-volume-fraction measurements in a turbulent C_2H_4-fueled jet flame," tech. rep., Sandia National Laboratories, 2015. SAND2015-7968.

[196] C. R. Shaddix, J. Zhang, R. W. Schefer, J. Doom, J. C. Oefelein, S. Kook, L. M. Pickett, and H. Wang, "Understanding and predicting soot generation in turbulent non-premixed jet flames," tech. rep., Sandia National Laboratories, 2010. SAND2010-7178.

[197] "International sooting flame (ISF) workshop." https://www.adelaide.edu.au/cet/ isfworkshop/data-sets/turbulent-flames, accessed: 01/09/2018.

[198] A. K. Chatzopoulos and S. Rigopoulos, "A chemistry tabulation approach via rate-controlled constrained equilibrium (RCCE) and artificial neural networks (ANNs), with application to turbulent non-premixed $CH_4/H_2/N_2$ flames," *Proceedings of the Combustion Institute*, vol. 34, no. 1, pp. 1465–1473, 2013.

[199] L. L. C. Franke, A. K. Chatzopoulos, and S. Rigopoulos, "Tabulation of combustion chemistry via artificial neural networks (ANNs): Methodology and application to LES-PDF simulation of Sydney flame L," *Combustion and Flame*, vol. 185, pp. 245–260, 2017.

[200] T. Readshaw, T. Ding, S. Rigopoulos, and W. P. Jones, "Modelling of turbulent flames with the Large Eddy Simulation - Probability Density Function (LES-PDF) approach, stochastic fields and artificial neural networks," *Physics of Fluids*, vol. 33, 2021.

[201] J. Camacho, Y. Tao, and H. Wang, “Kinetics of nascent soot oxidation by molecular oxygen in a flow reactor,” *Proceedings of the Combustion Institute*, vol. 35, no. 2, pp. 1887–1894, 2015.